

Stellingen

behorende bij het proefschrift:

*Gradient-Dependent Plasticity
in Numerical Simulation of Localization Phenomena*

van J. Pamin

1. In de context van constitutieve relaties met een tangentoperator die niet voldoet aan de condities van symmetrie en positief-definitieit, dienen de klassieke voorwaarden voor eenduidigheid en goedgesteldheid van het randvoorwaardeprobleem opnieuw te worden gedefinieerd.
2. Een correct continuümmodel van een ontstevigend (*softening*) materiaal dient een parameter te bevatten die een minimum stelt aan de localisatiebreedte.
3. De toepasbaarheid van niet-standaardcontinuümmodellen is beperkt zolang er geen verband is gelegd tussen de vanuit de microstructuur gemotiveerde of experimenteel bepaalde interne lengteschaal, en de lengteschalen die gebruikt worden in macroscopische constitutieve modellen.
4. De toekomst van het modelleren van lokalisatie ligt in een combinatie van ruimtelijke gradiënten en snelheidsafhankelijkheid in de beschrijving van het continuüm, en in een combinatie van een continue en discontinue benadering voor een realistische beschrijving van het bezwijkgedrag.
5. Bij gebruik van gemengde eindige elementen voor het oplossen van niet-lineaire randvoorwaardeproblemen, dienen *locking* en oneigenlijke mechanismen met meer nauwkeurigheid te worden onderzocht dan in het lineaire geval.
6. Het constateren van een probleem heeft een beperkte waarde zolang er geen oplossing voor wordt aangedragen.
7. Nederland is een goed voorbeeld van een land waarin discriminatie en intolerantie aan het verdwijnen zijn. Om dit soort verschijnselen kwijt te raken moet men eerst armoede kwijt.
8. Het is jammer dat ten behoeve van de verhoging van het nationale inkomen in Centraal Europa de mensen meer inspanning moeten gaan steken in hun carrière ten koste van hun gezinsleven.
9. Computer en popcultuur hebben ertoe geleid dat de Engelse taal wereldwijd als communicatiemiddel wordt geaccepteerd. Het nasynchroniseren van Engelse en Amerikaanse films en televisie programma's is daarom een onnodige en onzinnige maatregel onder het mom van de bescherming van de nationale taal.
10. Wetenschappelijke netwerken worden belangrijker, aangezien tijden van economische recessie vragen om een verdeling van onderzoekstaken tussen verschillende landen en organisaties.

11. Een precieze wiskundige formulering van een probleem en de oplossing ervan vermijden veel moeilijkheden in onderzoek. Jonge onderzoekers dienen daarom meer te worden geoefend in wiskundige technieken.
12. Een evenwicht tussen de individuele pogingen van een onderzoeker en de samenwerking met de groep is essentieel voor het minimaliseren van de tijd nodig voor het bereiken van goede onderzoeksresultaten.

GRADIENT-DEPENDENT PLASTICITY
IN NUMERICAL SIMULATION
OF LOCALIZATION PHENOMENA

**TR diss
2482**

GRADIENT-DEPENDENT PLASTICITY
IN NUMERICAL SIMULATION
OF LOCALIZATION PHENOMENA



PROEFSCHRIFT

ter verkrijging van de graad van doctor
aan de Technische Universiteit Delft,
op gezag van de Rector Magnificus, Prof. ir. K. F. Wakker,
in het openbaar te verdedigen ten overstaan van een commissie
aangewezen door het College van Dekanen
op 12 december 1994 te 13.30 uur

door

JERZY KRZYSZTOF PAMIN

magister inżynier budownictwa,
Politechnika Krakowska,
geboren te Krynica, Polen

Dit proefschrift is goedgekeurd door de promotor:

Prof. dr. ir. R. de Borst

Samenstelling promotiecommissie:

Prof. dr. ir. E. van der Giessen, TU Delft

Prof. dr. G. Pijaudier-Cabot, ENS de Cachan

Prof. dr. ir. J.C. Walraven, TU Delft

Prof. dr. Z. Waszczyszyn, Politechnika Krakowska

Dr. ir. P.J.G. Schreurs, TU Eindhoven

Dr. ir. L.J. Sluys, TU Delft

Published and distributed by:

Delft University Press

Stevinweg 1

2628 CN Delft

The Netherlands

Telephone +31 15 783254

Fax +31 15 781661

CIP-GEGEVENS KONINKLIJKE BIBLIOTHEEK, DEN HAAG

Pamin, Jerzy Krzysztof

Gradient-dependent plasticity in numerical simulation of
localization phenomena / Jerzy Krzysztof Pamin. - Delft:

Delft University Press. - 111.

Proefschrift Technische Universiteit Delft. - Met lit.

opg. - Met samenvatting in het Nederlands.

ISBN 90-407-1042-2

NUGI 841

Trefw.: plastische deformatie.

Copyright © 1994 by J. Pamin

All rights reserved.

No part of the material protected by this copyright notice may be reproduced or utilized in any form or by any means, electronic or mechanical, including photocopying, recording or by any information storage and retrieval system, without permission from the publisher:

Delft University Press, Stevinweg 1, 2628 CN Delft, the Netherlands.

Printed in the Netherlands.

Acknowledgements

The research reported in this thesis has been carried out at the Faculty of Civil Engineering, Delft University of Technology in the years 1991-1994, on leave from Cracow University of Technology. The algorithm and finite elements have been implemented in the pilot version of the DIANA code. The calculations have been performed on Sun and Silicon Graphics workstations. The financial support of the Commission of the European Communities within the Brite-Euram program (project BE-3275) is gratefully acknowledged.

I would like to express my deep gratitude to Prof. René de Borst for formulating the basis of my research, useful suggestions and patient guidance. I am also grateful to all my colleagues from the computational mechanics group and the faculty, especially to Peter Feenstra, Han Schellekens, Bert Sluys, Arend Groen, Paulo Lourenço, Harold Thung and Wei Min Wang, for their support and interesting discussions. Illuminating talks with Prof. H.-B. Mühlhaus from CSIRO Division of Exploration and Mining in Melbourne and Dr. J. Carmeliet from Catholic University of Leuven are also gratefully acknowledged.

I would like to record my deep appreciation of the system of doctoral studies in the Netherlands and thank all the authors of the theses referenced in this work.

Special thanks goes to Prof. Z. Waszczyszyn from Cracow University of Technology, who was my first teacher of computational mechanics and made my coming to Delft possible. Last but not least I would like to thank my wife and my parents for their love and patience.

Contents

| | |
|--|----|
| 1. Introduction | 1 |
| 1.1 Scope and objectives | 1 |
| 1.2 Assumptions and contents | 2 |
| 2. Strain localization in softening media | 4 |
| 2.1 Background and problem statement | 4 |
| 2.1.1 Material instability and loss of ellipticity | 6 |
| 2.1.2 Implications for softening and non-associated plasticity | 10 |
| 2.1.3 Mesh sensitivity of results for classical continuum | 12 |
| 2.2 Related work and possible solution approaches | 16 |
| 2.2.1 Discontinuum versus continuum modelling | 16 |
| 2.2.2 Micropolar continuum | 19 |
| 2.2.3 Nonlocal integral models | 20 |
| 3. Gradient-dependent softening plasticity theory | 25 |
| 3.1 Essentials of the theory | 25 |
| 3.1.1 Analytical solution for one-dimensional case | 26 |
| 3.1.2 Material stability and ellipticity | 28 |
| 3.2 Rate boundary value problem | 30 |
| 3.3 Weak form of field equations | 33 |
| 3.3.1 Variational formulation | 34 |
| 4. Algorithm and finite elements | 36 |
| 4.1 Incremental formulation | 36 |
| 4.1.1 C^1 -continuous element formulation | 39 |
| 4.1.2 C^0 -approach with a penalty constraint | 42 |
| 4.2 Algorithmic problems | 45 |
| 4.2.1 Consistent linearization | 45 |
| 4.2.2 Comparison with a standard plasticity algorithm | 46 |
| 4.2.3 Gradient-dependent yield strength | 49 |
| 4.3 Two-dimensional cases | 52 |
| 4.3.1 Plane strain case | 53 |
| 4.3.2 Plane stress case | 54 |
| 4.4 Finite elements | 55 |
| 4.4.1 One-dimensional elements | 56 |
| 4.4.2 Quadrilateral elements | 57 |
| 4.4.3 Triangular elements | 62 |
| 5. Mesh-sensitivity studies | 65 |
| 5.1 Huber-Mises gradient plasticity | 65 |
| 5.2 One-dimensional tests | 66 |
| 5.3 Shear banding examples | 70 |

| | | |
|-------|---|-----|
| 5.3.1 | Rectangular elements | 70 |
| 5.3.2 | Triangular elements | 73 |
| 5.4 | Imperfection sensitivity | 75 |
| 6. | Application to soil instability problems | 78 |
| 6.1 | Drucker-Prager gradient plasticity | 79 |
| 6.2 | Biaxial compression test | 80 |
| 6.2.1 | Associated flow rule | 80 |
| 6.2.2 | Non-associated flow rule | 84 |
| 6.3 | Slope stability problem | 86 |
| 7. | Application to concrete fracture | 91 |
| 7.1 | Vertex-enhanced Rankine fracture function | 92 |
| 7.1.1 | Vertex smoothing approach | 95 |
| 7.1.2 | Drucker-Prager type approximation | 97 |
| 7.2 | Four point bending | 99 |
| 7.3 | Direct tension test | 105 |
| 7.4 | Single-edge-notched beam | 109 |
| 7.5 | Double-edge-notched specimen | 112 |
| 8. | Conclusions | 119 |
| | References | 122 |
| | Table 1: Gradient plasticity elements | 129 |
| | Summary | 131 |
| | Samenvatting | 133 |

1. Introduction

Observation of the mechanical behaviour and failure of various materials reveals the existence of *localization* phenomena. Strain localization is a notion describing a deformation mode, in which the whole deformation of a material specimen occurs in one or more narrow bands, while the rest of the specimen usually exhibits unloading. The width and direction of localization bands depend on material parameters, geometry, boundary conditions, loading distribution and loading rate.

The origin of localization lies at the micro-level of observation. In simple terms, material heterogeneity induces a strongly nonlinear behaviour and local weakness of the material, which is an *instability* triggering strain localization. As a result of the inhomogeneous deformations a *softening* response at the structural level is observed.

To assess the safety of a system it is necessary to analyze its ductility. In other words, it is necessary to evaluate the danger of a sudden (brittle) failure just after attaining the limit load. Therefore there exists a demand for reliable computational methods capable of reproducing the post-peak behaviour in addition to the ultimate load carrying capacity.

Classical, i.e. local constitutive models, expressed in terms of (averaged) stress and strain, embody an implicit assumption that the deformation of the specimen varies in a sufficiently smooth manner. This is not the case when strain localization occurs. Nevertheless a variety of strain softening models which feature a descending relation between the stress and strain have been formulated. The mathematical implication of such a constitutive relation within the classical continuum description is the loss of *well-posedness* of the partial differential equations governing the solution of a given boundary value problem. In a similar way the well-posedness is lost when we deal with dynamic (e.g. wave propagation) problems. The further consequence is a spurious discretization sensitivity in numerical simulations of localization and softening problems.

1.1 Scope and objectives

In this thesis we focus our attention on the computational mechanics of frictional materials, in particular granular materials (soils) and quasi-brittle materials (concrete). They are characterized by highly nonlinear stress-strain and volume change relations and their failure usually involves strain localization in the form of shear bands or cracks.

We use the framework of plasticity theory, which is a natural choice for the description of soil behaviour but can also be adapted to give meaningful results for quasi-brittle materials like concrete and rock. However, the used theory of the rate-independent plastic flow is not classical: to preserve well-posedness of the governing equations we incorporate higher-order gradients of plastic strains in the definition of the yield function. This enhancement can be explained from the physical point of view: higher-order strain gradients play an important role in a proper representation of highly nonuniform (localized) deformation.

The gradient dependence of the yield function has an important consequence: the

plastic consistency condition, which is an algebraic equation in the classical case and then allows for a straightforward determination of the plastic strain increment, is a partial differential equation in the present theory. Therefore in order to solve the boundary value problem of *gradient plasticity* an independent finite element discretization of the displacement and plastic strain fields is used. The theory, algorithm and finite element formulation are given for the general case of a three-dimensional continuum. The applications are limited to two-dimensional (plane stress and plane strain) configurations.

The main objective of this work is thus a finite element implementation of an enhanced elasto-plastic continuum model for the analysis of localized deformation in softening materials. Our aim is not a formulation or verification of an accurate or general constitutive model for soil or concrete, but the development of a regularization methodology (localization limiter) that prevents the loss of well-posedness and its negative consequences in numerical analysis, i.e. pathological mesh refinement and alignment sensitivity. We believe however that an adequate constitutive model for a softening continuum must be furnished with a localization limiter.

Special emphasis is laid on the concrete fracture problems and therefore many interpretations are made from the viewpoint of concrete mechanics. In the applications of the gradient plasticity model to concrete a quantitative comparison with the experimental results is performed.

1.2 Assumptions and contents

The main assumptions of this work are the *static loading* and *small deformations* of the analyzed configurations. We limit the consideration to monotonic loading. We employ a deterministic description of isotropic and homogeneous continuum.

Chapter 2 deals with the physical and theoretical background of the localization phenomena. The notions of material stability and ellipticity are recalled. The fundamental difficulty in the formulation and numerical predictions of localization problems within the framework of the classical continuum are shown. The possible solution approaches and the existing regularization methods (micropolar and nonlocal continuum) are summarized.

Chapter 3 presents the rate boundary value problem of gradient-dependent softening plasticity. The localization limiting properties of the employed theory are shown analytically. The weak form of the field equations is derived. Chapter 4 presents the incremental equations and the algorithm used in numerical simulations. The classical elastic predictor-plastic corrector idea is followed and the consistent tangent operator is derived. Finite element formulations with C^1 - and C^0 -continuous interpolation functions for the plastic strain field are presented and the implemented elements are characterized.

Chapter 5 reports the results of mesh-sensitivity analyses in one-dimensional and two-dimensional localization tests. The Huber-Mises gradient-dependent softening plasticity is applied. The behaviour of all implemented elements is compared and the influence of structural imperfections is investigated. Chapter 6 presents the application of the Drucker-Prager yield function with gradient-dependent degrading cohesion to the

numerical simulation of localization phenomena in soil. The biaxial compression test and the slope stability problem are analyzed.

Chapter 7 is devoted to the analysis of concrete cracking problems. A formulation of the vertex-enhanced Rankine gradient plasticity with nonlinear softening is proposed and applied in the simulation of Mode-I fracture in a four point bending test, a direct tension test and a single-edge-notched beam. Finally mixed-mode fracture in a double-edge-notched specimen is analyzed. Comparisons with experimental results are made, the roles of the fracture energy and the internal length scale are examined and the size effect is demonstrated. Chapter 8 summarizes the conclusions from the results.

A conventional notation is used in the whole thesis and each symbol is defined when it appears for the first time or when it changes its meaning.

2. Strain localization in softening media

2.1 Background and problem statement

At the macroscopic level of observation deformed solids frequently exhibit concentrations of deformation in small zones. This phenomenon may be caused by geometrical effects (e.g. shape and boundary conditions of the body) or by material effects (e.g. heterogeneity and local defects). In this thesis we are dealing only with the latter case, called *strain localization*.

We consider a body subjected to such loads and boundary conditions, that the resulting deformation is approximately homogeneous. Localization occurs suddenly at a certain point of the loading history when the whole further deformation is confined in narrow band-shaped parts of the body, while the remaining parts of the body exhibit unloading. Localization is usually accompanied by a decrease of the load carrying capacity after reaching the peak load. It is often a precursor to ductile or brittle fracture, since the large deformations accumulated in the small localization bands lead to rupture.

The gradual decrease of the stiffness and load carrying capacity with the increase of deformation imposed on the body is called *softening*. Fig. 2.1 shows a typical result of an experiment, in which after attaining the maximum load a descending branch of the load-deformation diagram is observed. The deformation Δv is measured over the length L_m enclosing the localization zone. Gauges attached to the lower part of the bar reveal unloading.

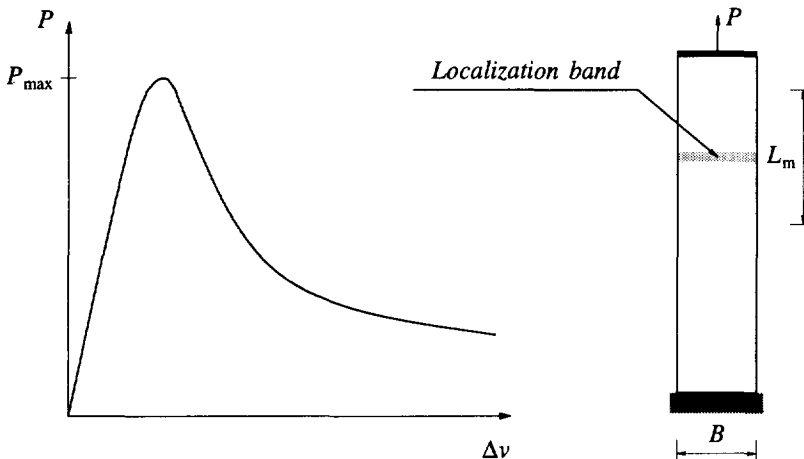


Figure 2.1 Softening response related to strain localization.

It is noted that such an experiment must be carried out under servo-control (under load control the bar would fail at the peak load P_{\max}) and that the controlling parameter must be carefully chosen (i.e. must monotonically increase). Results of this experiment depend on the size and shape of the specimen and the boundary conditions (Read and

Hegemier 1984, Sandler 1984). Accordingly, softening is rather a structural property, since it is largely a manifestation of the fact, that the deformation of the specimen is highly inhomogeneous. Nevertheless, intrinsic material softening may exist in certain kinds of materials.

Localization of deformation is observed for a variety of materials, whether they possess ductile (plastic) or brittle (damaging) characteristics. Patterns of intense shear deformation occur in metals, polymers and soil masses, cracking is observed in concrete, rock and ceramics. The width of the shear bands is small (but finite) and depends on the examined material. Apparently there exists a characteristic length parameter that sets the size of the bands. Localization is sometimes promoted by a dynamic character of loading (e.g. adiabatic shear bands in metals, which are caused by a rapid local heating due to high-rate plastic deformation). On the other hand localization may be precluded by boundary conditions. In this thesis we focus our interest on fracture phenomena in structural concrete and shear band development in granular materials (soils) under static loading.

Though strain localization is a macroscopic phenomenon, its origin lies in the material microstructure. To analyze the forming and evolution of localization zones, we must go below the macroscopic level of observation. At this so-called *meso-level of observation* (van Mier 1984) every material is inhomogeneous and, due to the presence of microvoids and microcracks, it is also discontinuous. Soil is built of grains, with pores or water in between. Concrete is a two-phase material composed of aggregate and mortar with microcracks existing at the interfaces of the two phases and in the cement paste.

During an increasing deformation the microstructures evolve in the material. Grains rotate and slide, microvoids nucleate and grow, microcracks propagate and get arrested by encountered aggregate, new microcracks initiate from existing weak spots. However, when the deformation is smooth and its gradients are small, i.e. if the characteristic deformation scale is much larger than the characteristic size of the material heterogeneity (Mühlhaus et al 1991), the microstructural contributions to the deformation vanish upon averaging and we may assume the material to be a classical continuum with some equivalent characteristics (strain and stress are understood as averaged values). This is the case prior to the ultimate load and before the emergence of localization bands.

In the softening regime, i.e. when a localized deformation mode gets activated by a local defect, the characteristic deformation scale and the microstructure size become comparable. In the presence of large deformation gradients the relative motions of microstructures contribute significantly to the deformation of the body. Moreover, the microstructures interact over distances comparable to the length scale in the deformation pattern, which means that the state of the material at a point depends on the deformation history of a certain neighbourhood of this point (i.e. the material behaviour is *nonlocal*). In fact, these microstructural processes are the driving force behind the localization phenomenon.

In quasi-brittle materials the growth and coalescence of microcracks leads to

macroscopic cracks, i.e. discontinuities that divide the body into some separated parts. In plain concrete the macrocrack formation is delayed because of the crack bridging effect of aggregate (van Mier 1991) and in reinforced or fiber concrete composites the fracture gets distributed owing to the stress redistribution between the phases.

Returning to our idealization in Fig. 2.1, the deformation Δv within the measuring length L_m includes the inelastic deformation in the fracture zone and the elastic unloading outside this zone. If we perform a homogenization by defining the stress as the acting load P over the initial load carrying area $B \times t$ (where t is the thickness of the bar) and defining the strain as the measured deformation Δv over the length L_m , we obtain a continuum model called here *strain softening*. However, in this approach we disregard the essential inhomogeneity of deformation and the decrease of load carrying area due to increasing damage in the fracture zone.

2.1.1 Material instability and loss of ellipticity

We temporarily limit the discussion to the classical (standard) continuum. By this term we mean a continuum description (cf. for instance Becker & Burger 1975), in which the stress tensor σ_{ij} at a certain point of a body depends only on the deformation history of this point and the functional dependence is only through the first order deformation gradient F_{ij} :

$$\sigma_{ij}(\xi_k, t) = \psi_{ij}(\xi_k, F_{lm}(\xi_k, t - \tau)), \quad 0 \leq \tau < \infty, \quad (2.1)$$

where ξ_k are the (Cartesian) material coordinates of the point in the reference configuration and t is the time. The local constitutive relation in eq. (2.1) defines a so-called *simple material*, which possesses no internal length scale. The deformation gradient tensor F_{ij} is defined on the basis of the motion functions $x_i = x_i(\xi_j, t)$ written in terms of the (Cartesian) spatial coordinates x_i of the point in the present configuration

$$F_{ij} = \frac{\partial x_i}{\partial \xi_j}. \quad (2.2)$$

Introducing the displacement vector $u_i = x_i - \xi_i$ we observe that the deformation gradient is related to the displacement derivatives:

$$F_{ij} = \frac{\partial u_i}{\partial \xi_j} + \delta_{ij}, \quad (2.3)$$

where δ_{ij} denotes a second order unit tensor.

In rate boundary value problems the rate of the deformation gradient is needed. For this purpose we differentiate eq. (2.3) to obtain:

$$\dot{F}_{ij} = \frac{\partial \dot{u}_i}{\partial \xi_j} = \frac{\partial \dot{u}_i}{\partial x_k} F_{kj}, \quad (2.4)$$

where the superimposed dots denote the derivative with respect to time. At this point we introduce the assumption of small deformation gradients:

$$F_{ij} \approx \delta_{ij}, \quad (2.5)$$

so that the rate of the deformation gradient is obtained as:

$$\dot{F}_{ij} \approx \frac{\partial \dot{u}_i}{\partial x_j} . \quad (2.6)$$

To eliminate rotation effects we take the symmetric part of \dot{F}_{ij} and define

$$\dot{\epsilon}_{ij} = \frac{1}{2} \left(\frac{\partial \dot{u}_i}{\partial x_j} + \frac{\partial \dot{u}_j}{\partial x_i} \right) \quad (2.7)$$

as the strain rate tensor.

We will now examine mathematical consequences of the strain softening constitutive relations and consider a possibility of localization within the classical continuum (cf. de Borst 1986, Willam and Etse 1990, Neilsen and Schreyer 1993).

First we recall the classical notion of *material stability* (Hill 1958, Maier and Hueckel 1979). A material is defined as stable if its constitutive relationship fulfils the condition of a positive second order work density:

$$\dot{\epsilon}_{ij} \dot{\sigma}_{ij} > 0 , \quad (2.8)$$

where $\dot{\sigma}_{ij}$ is the stress rate tensor and the summation convention is adopted. Since the stability of a body that occupies a volume V is assured if

$$\int_V \dot{\epsilon}_{ij} \dot{\sigma}_{ij} dV > 0 \quad (2.9)$$

for all kinematically admissible $\dot{\epsilon}_{ij}$, the existence of points in which inequality (2.8) is violated may lead to a structural instability.

In the following considerations we limit our interest to incrementally linear constitutive equations:

$$\dot{\sigma}_{ij} = D_{ijkl} \dot{\epsilon}_{kl} , \quad (2.10)$$

in which the tangent stiffness tensor D_{ijkl} , in general nonsymmetric, is piecewise independent of the strain rate $\dot{\epsilon}_{kl}$. We will adopt the concept of a linear comparison solid of Hill (1958), which means that the possibility of unloading is not considered. We substitute eq. (2.10) into inequality (2.8) and observe that the occurrence of material instability is indicated by the loss of positive-definiteness of the material tangent stiffness tensor D_{ijkl} :

$$\dot{\epsilon}_{ij} D_{ijkl} \dot{\epsilon}_{kl} = 0 . \quad (2.11)$$

This condition coincides with the singularity of the symmetric part of D_{ijkl} :

$$\det(D_{ijkl} + D_{klij}) = 0 . \quad (2.12)$$

The limit point condition has the form:

$$\dot{\sigma}_{ij} = D_{ijkl} \dot{\epsilon}_{kl} = 0 , \quad (2.13)$$

so that $\det(D_{ijkl}) = 0$. The last condition can also mark the existence of a non-unique solution of the differential equation (2.10). For a symmetric tangent stiffness tensor D_{ijkl} the loss of material stability coincides with the limit point and the loss of uniqueness. For a nonsymmetric tangent stiffness tensor the loss of material stability may be encountered prior to the limit point and loss of uniqueness (cf. Willam and Etse 1990).

For a discrete mechanical system we can introduce the (nonsymmetric) structural

tangent stiffness matrix \mathbf{K} :

$$\mathbf{K} = \int_V \mathbf{B}^T \mathbf{D}^e \mathbf{B} dV, \quad (2.14)$$

where the matrix \mathbf{B} relates the strain rate vector $\dot{\boldsymbol{\varepsilon}}$ to the nodal displacement rate vector $\dot{\mathbf{a}}$:

$$\dot{\boldsymbol{\varepsilon}} = \mathbf{B} \dot{\mathbf{a}} \quad (2.15)$$

and the superscript T is the transpose symbol. We can write the structural instability condition in terms of the loss of positive definiteness of the tangent stiffness matrix \mathbf{K} , cf. inequality (2.9):

$$\det(\mathbf{K} + \mathbf{K}^T) = 0. \quad (2.16)$$

We consider also the uniqueness of the solution of the rate boundary value problem. If the solution is not unique, there exist two different stress rates which satisfy the following equilibrium equation:

$$\mathbf{L}^T \dot{\boldsymbol{\sigma}} + \dot{\mathbf{b}} = \mathbf{0}, \quad (2.17)$$

where \mathbf{L} is a differential operator and $\dot{\mathbf{b}}$ is a body-force rate vector. Eq. (2.17) can be written for the two stress rates and upon subtraction we obtain:

$$\mathbf{L}^T \Delta \dot{\boldsymbol{\sigma}} = \mathbf{0}, \quad (2.18)$$

where 'Δ' denotes a difference between two quantities. The relevant static and kinematic boundary conditions are fulfilled by each of the two solutions. Now, following the idea of the weighted residuals, we write a weak form of the above equation:

$$\int_V \mathbf{w}^T (\mathbf{L}^T \Delta \dot{\boldsymbol{\sigma}}) dV = 0 \quad (2.19)$$

and associate the weighting function \mathbf{w} with a variation of the difference between the displacement rates for the two considered solutions $\delta \Delta \dot{\mathbf{u}}$. We then apply Green's formula and the boundary conditions to obtain the equation:

$$\int_V \delta \Delta \dot{\boldsymbol{\varepsilon}}^T \Delta \dot{\boldsymbol{\sigma}} dV = 0. \quad (2.20)$$

Substitution of the matrix form of eq. (2.10) and eq. (2.15), and the requirement that the equation holds for an arbitrary variation of the displacement rate field $\delta \Delta \dot{\mathbf{a}}$ leads to the equation:

$$\mathbf{K} \Delta \dot{\mathbf{a}} = \mathbf{0}, \quad (2.21)$$

which has a non-trivial solution if

$$\det(\mathbf{K}) = 0. \quad (2.22)$$

This means that a point of bifurcation or limit load is detected when the smallest eigenvalue of the tangent operator \mathbf{K} becomes negative. We conclude again that for a symmetric tangent operator the loss of structural stability coincides with the loss of solution uniqueness (and also with the limit point condition). For a nonsymmetric tangent stiffness the structural stability may be lost prior to the loss of uniqueness (cf. de Borst et al 1993).

Next, we consider a homogeneous and homogeneously deformed body and investigate the possibility of such behaviour, that upon a further increment of deformation not only the homogeneous solution, but also a discontinuity of the deformation gradient across a plane with normal v_i is admitted (cf. for instance Rudnicki and Rice 1975, Ortiz et al 1987, Runesson et al 1991):

$$[[u_{i,j}]] = u_{i,j}^+ + u_{i,j}^- \neq 0, \quad (2.23)$$

where $[[\]]$ denotes a jump of a quantity and the '+' and '-' sign refer to the two sides of the discontinuity plane. During this bifurcation the continuity of displacements and the equilibrium condition are preserved pointwise. If we assume that the deformation fulfils the kinematic compatibility equations, it must be piecewise homogeneous, so the jump of the displacement gradient has the form:

$$[[u_{i,j}]] = v_i \mu_j, \quad (2.24)$$

for an arbitrary vector μ_i . The strain jump may be written as follows:

$$[[\varepsilon_{ij}]] = \frac{1}{2} (v_i \mu_j + v_j \mu_i). \quad (2.25)$$

With the piecewise linear constitutive equation (2.10) we obtain the stress rate jump at the onset of the discontinuity:

$$[[\dot{\sigma}_{ij}]] = D_{ijkl} [[\dot{\varepsilon}_{kl}]], \quad (2.26)$$

where it has been assumed that the same tangent stiffness moduli govern the material behaviour on both sides of the discontinuity plane (cf. the concept of a linear comparison solid of Hill 1958). In terms of the plasticity theory this corresponds to the plastic/plastic bifurcation, which has been shown to occur prior to the bifurcation with plastic loading on one side and elastic unloading on the other side of the discontinuity (cf. Runesson et al 1991). Equilibrium requires that during the formation of the discontinuity the tractions t_j are continuous across the plane with normal v_i :

$$[[t_j]] = v_i [[\dot{\sigma}_{ij}]] = 0, \quad (2.27)$$

so substituting eq. (2.26) and (2.25), and exploiting the (minor) symmetry property $D_{ijkl} = D_{ijlk}$ we obtain the condition:

$$(v_i D_{ijkl} v_l) \mu_k = 0, \quad (2.28)$$

which gives a non-trivial solution only when the determinant of the so-called acoustic tensor $Q_{jk} = v_i D_{ijkl} v_l$ vanishes:

$$\det(Q_{jk}) = 0. \quad (2.29)$$

For a given tangent stiffness the last condition yields a vector v_l , which defines the discontinuity direction, the vector μ_k can then be determined from eq. (2.28) and the jump mode in eq. (2.24) is known.

The singularity of the acoustic tensor and the formation of the discontinuity correspond to the local loss of ellipticity of the rate equilibrium equations. Ellipticity is one of the necessary conditions for well-posedness of the rate boundary value problem (cf. Benallal et al 1991). Here, well-posedness is understood as the existence of a finite

number of linearly independent and continuous solutions. It is important to notice that under the assumption of small deformation gradients the loss of ellipticity can occur only if the material stability has been lost (cf. Willam and Etse 1990, de Borst et al 1993).

The emergence of the discontinuities in the deformation gradient has traditionally been identified with strain localization. In other terms localization has been understood as a bifurcation in the macroscopic constitutive description of the material (Rudnicki and Rice 1975). A shear band may then be viewed as a zone of intense deformation bounded by two discontinuity planes. However, since the distance between those planes remains undefined for a simple material, they coincide giving localization in a set of measure zero. In this thesis the notion of strain localization is understood in a broader sense, according to the definition at the beginning of Chapter 2.1.

It is noted that in addition to the above analyzed *weak* discontinuities jumps in the displacement field itself (*strong* discontinuities) can be considered (cf. Willam et al 1994). They correspond to a total material fracture along plane interfaces, while in the continuous parts of the body material stability and ellipticity are preserved. Since the softening behaviour is then concentrated in the interfaces, the boundary value problem for the discontinuum remains well-posed.

2.1.2 Implications for softening and non-associated plasticity

For the sake of the following considerations we summarize a classical softening plasticity model starting from a uniaxial case. A strain softening relation between uniaxial stress and strain may be obtained by the transformation of the experimental force-deformation diagram described in the previous section. In Fig. 2.2 a simple relation is plotted, composed of a linear elastic branch and a linear softening branch.

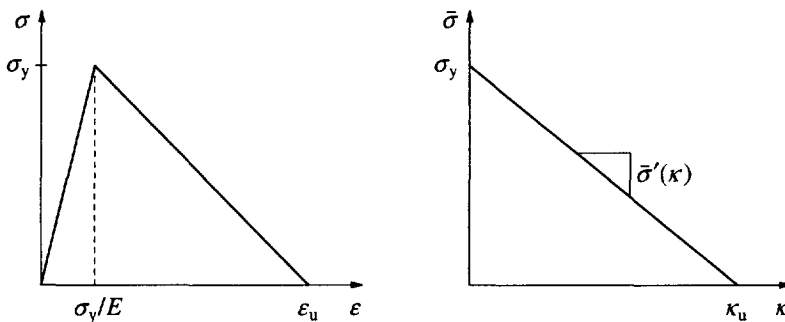


Figure 2.2 Linear strain-softening model for a uniaxial case (left) and in terms of equivalent measures (right).

In the post-peak regime, i.e. when the limit stress σ_y has been reached, we assume a decomposition of the total strain ε into an elastic part and a plastic (or, more generally, inelastic) part:

$$\boldsymbol{\varepsilon} = \boldsymbol{\varepsilon}^e + \boldsymbol{\varepsilon}^p . \quad (2.30)$$

The elastic strains are governed by Hooke's law:

$$\boldsymbol{\varepsilon}^e = \frac{\boldsymbol{\sigma}}{E} \quad (2.31)$$

and the plastic strains are determined from the yield (or failure) condition:

$$\boldsymbol{\sigma} = \boldsymbol{\sigma}_y + h \boldsymbol{\varepsilon}^p , \quad \boldsymbol{\varepsilon}^p = \frac{\boldsymbol{\sigma} - \boldsymbol{\sigma}_y}{h} , \quad (2.32)$$

where h is a negative softening modulus:

$$h = - \frac{\boldsymbol{\sigma}_y}{\boldsymbol{\varepsilon}_u} \quad (2.33)$$

and $\boldsymbol{\varepsilon}_u > \boldsymbol{\sigma}_y/E$ is the strain at which the load-carrying capacity is totally exhausted. The tangential relation between the stress rate (or increment) and the strain rate may be calculated by differentiating and combining eqs (2.30), (2.31) and (2.32):

$$\dot{\boldsymbol{\sigma}} = \frac{Eh}{h+E} \dot{\boldsymbol{\varepsilon}} , \quad -E < h < 0 . \quad (2.34)$$

When the hardening modulus h is non-positive, material stability and ellipticity are lost. This means that at the onset of softening the problem becomes ill-posed, continuity is lost and in a one-dimensional case localization occurs in a point.

In a general case of a three-dimensional elasto-plastic body the constitutive relation has the form:

$$\dot{\boldsymbol{\sigma}} = \mathbf{D}^e (\dot{\boldsymbol{\varepsilon}} - \dot{\lambda} \mathbf{m}) , \quad (2.35)$$

where $\dot{\boldsymbol{\sigma}}$ and $\dot{\boldsymbol{\varepsilon}}$ are the stress and strain rate tensors, respectively, \mathbf{D}^e is an elastic stiffness matrix, $\dot{\lambda}$ determines the magnitude and \mathbf{m} the direction of the plastic flow. The vector \mathbf{m} can be derived from a plastic potential G as $\mathbf{m} = \partial G / \partial \boldsymbol{\sigma}$. The yield function with a classical isotropic hardening rule can be written as:

$$F(\boldsymbol{\sigma}, \kappa) = \phi(\boldsymbol{\sigma}) - \bar{\sigma}(\kappa) , \quad (2.36)$$

where $\bar{\sigma}$ is a yield strength and κ is an invariant plastic strain measure. The Kuhn-Tucker conditions must be fulfilled:

$$\dot{\lambda} \geq 0 , \quad F \leq 0 , \quad \dot{\lambda} F = 0 \quad (2.37)$$

and the plastic flow is governed by the consistency condition

$$\dot{F} = \mathbf{n}^T \dot{\boldsymbol{\sigma}} - h \dot{\lambda} = 0 , \quad (2.38)$$

where the gradient to the yield function and the hardening modulus are defined as:

$$\mathbf{n} = \frac{\partial F}{\partial \boldsymbol{\sigma}} = \frac{\partial \phi}{\partial \boldsymbol{\sigma}} \quad (2.39)$$

and

$$h = - \frac{\dot{\kappa}}{\dot{\lambda}} \frac{\partial F}{\partial \kappa} = \frac{\dot{\kappa}}{\dot{\lambda}} \frac{\partial \bar{\sigma}}{\partial \kappa} , \quad (2.40)$$

respectively. We notice that both $\dot{\kappa}$ and $\dot{\lambda}$ are positive. Softening is introduced in the model if we assume a descending relation between the yield strength and the hardening parameter, so that $\bar{\sigma}'(\kappa) < 0$ and $h < 0$ (note that $\bar{\sigma}'(\kappa)$ is constant in Fig. 2.2).

Calculation of $\dot{\lambda}$ from eq. (2.38), substitution into eq. (2.35) and solution for $\dot{\boldsymbol{\epsilon}}$ gives the tangential compliance relation:

$$\dot{\boldsymbol{\epsilon}} = [(\mathbf{D}^e)^{-1} + \frac{1}{h} \mathbf{m}\mathbf{n}^T] \dot{\boldsymbol{\sigma}} \quad (2.41)$$

and with the aid of the Sherman-Morrison formula we obtain the tangential stiffness relation:

$$\dot{\boldsymbol{\sigma}} = \left[\mathbf{D}^e - \frac{\mathbf{D}^e \mathbf{m}\mathbf{n}^T \mathbf{D}^e}{h + \mathbf{n}^T \mathbf{D}^e \mathbf{m}} \right] \dot{\boldsymbol{\epsilon}}, \quad (2.42)$$

which defines the general (nonsymmetric) elasto-plastic stiffness matrix:

$$\mathbf{D}^{ep} = \mathbf{D}^e - \frac{\mathbf{D}^e \mathbf{m}\mathbf{n}^T \mathbf{D}^e}{h + \mathbf{n}^T \mathbf{D}^e \mathbf{m}}. \quad (2.43)$$

We now investigate material stability for this constitutive relation. To this end we substitute the tangent stiffness matrix \mathbf{D}^{ep} into the matrix form of eq. (2.11):

$$\dot{\boldsymbol{\epsilon}}^T \mathbf{D}^{ep} \dot{\boldsymbol{\epsilon}} = \dot{\boldsymbol{\epsilon}}^T \mathbf{D}^e \dot{\boldsymbol{\epsilon}} - \dot{\boldsymbol{\epsilon}}^T \frac{\mathbf{D}^e \mathbf{m}\mathbf{n}^T \mathbf{D}^e}{h + \mathbf{n}^T \mathbf{D}^e \mathbf{m}} \dot{\boldsymbol{\epsilon}} = 0. \quad (2.44)$$

For $\mathbf{n} = \mathbf{m}$ (associated plasticity) the loss of material stability is possible when the hardening modulus h is zero or negative. It can be seen from eq. (2.44) that for $\mathbf{n} = \mathbf{m}$ there exists a critical strain rate $\dot{\boldsymbol{\epsilon}} = \dot{\alpha} \mathbf{n}$ with scalar $\dot{\alpha}$, for which the product $\dot{\boldsymbol{\epsilon}}^T \dot{\boldsymbol{\sigma}} \leq 0$. For $\mathbf{n} \neq \mathbf{m}$ (non-associated plasticity) the loss of material stability may occur even if the hardening modulus is positive (cf. Rudnicki and Rice 1975, Maier and Hueckel 1979, de Borst 1986, Runesson and Mróz 1989). The nonsymmetry of the tangent operator is thus a destabilizing factor.

Substituting the elasto-plastic stiffness matrix from eq. (2.43) into the definition of the acoustic tensor and analyzing eq. (2.29) it is possible to find the critical values of the hardening modulus h , for which ellipticity is lost, and the direction vector \mathbf{v} normal to the discontinuity plane (Rudnicki and Rice 1975, Runesson et al 1991). The critical value of h , which may be positive for non-associated plasticity, and the associated direction \mathbf{v} depend on the stress state as well as on the form of the yield and plastic potential functions. In numerical analysis of discrete systems the condition (2.29) may be used to detect the loss of ellipticity (potential localization) at the integration point level. However, an assessment of the post-critical behaviour of the system is impossible since well-posedness of the boundary value problem is lost.

2.1.3 Mesh sensitivity of results for classical continuum

After a brief physical and mathematical description of the localization problem we will present some results of finite element simulations. First we consider an illustrative example of a bar in tension (de Borst 1986) discretized into m elements as shown in Fig. 2.3. We adopt the uniaxial softening plasticity model from Section 2.1.2 and investigate the strain distribution and the global response of the bar in terms of the stress and average strain $\bar{\boldsymbol{\epsilon}}$ calculated as the displacement of the right end of the bar \bar{u} over its length L .

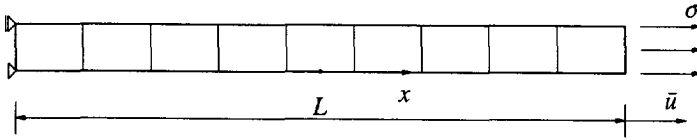


Figure 2.3 Bar in tension discretized into m elements.

We assume that all the elements have exactly the same thickness and material properties. If the computation accuracy is sufficient to rule out perturbations due to round-off errors, all elements are uniformly strained and the response of the bar follows exactly the material model given in Fig. 2.2. However, after the peak load the tangent operator of the finite element model possesses negative eigenvalues introduced by the negative tangent stiffnesses and the solution is unstable. In this situation any round-off error can cause a jump to a more critical solution, in which only a part of the bar softens. In fact, the smallest amount of energy is dissipated during failure when the plastic strains localize in only one element and all other elements unload. Therefore, when the deformation is inhomogeneous (as usually happens for more complex structures), the strains will have a tendency to concentrate in the smallest possible area. The finite element model approximates in this way the classical continuum solution, in which localization takes place in a set of measure zero.

We can induce this solution in our problem by making one element slightly weaker or thinner than the others. The strains then localize in this element and the solution for different discretizations is shown in Fig. 2.4. The average strain can be calculated as

$$\bar{\epsilon} = \frac{\bar{u}}{L} = \epsilon^e + \frac{1}{m} \epsilon^p \tag{2.45}$$

and upon substitution of eqs (2.31) and (2.32):

$$\bar{\epsilon} = \frac{\sigma}{E} + \frac{\sigma - \sigma_y}{mh} \tag{2.46}$$

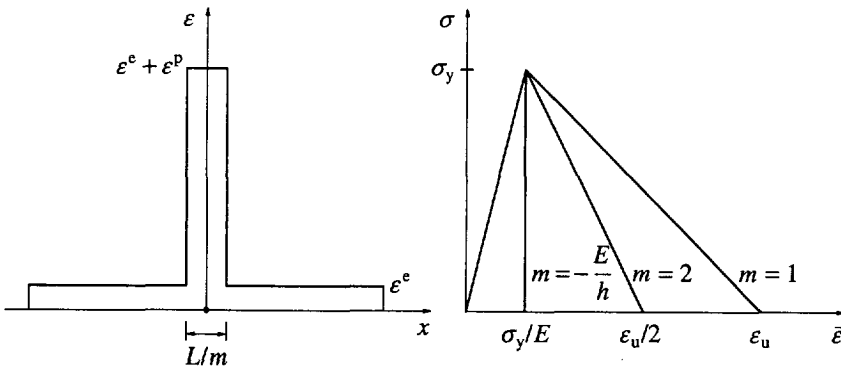


Figure 2.4 Bar response for m -element discretization.

The inclination of the post-peak diagram $\sigma - \bar{\epsilon}$ clearly depends on the number of

elements:

$$\frac{d\bar{\epsilon}}{d\sigma} = \frac{1}{E} - \frac{1}{mh} \quad (2.47)$$

We observe that after the onset of softening the solution is totally determined by the discretization. For the number of elements m going to infinity the post-peak response would follow back the elastic loading path and the Dirac δ distribution of strains would be obtained. This solution is physically unacceptable, since total failure takes place without energy dissipation. We notice that in the absence of a physically motivated length scale which would govern the width of the localization zone, such a scale is introduced in the problem by the discretization (element size L/m). Therefore a way to remedy the spurious mesh sensitivity of numerical results is to incorporate an internal length in the continuum description.

The spurious mesh dependence of finite element predictions can also be illustrated by the example of a plane strain specimen in biaxial compression (Fig. 2.5). The standard plasticity model with the Huber-Mises yield function is used:

$$F = \sqrt{3J_2} - \bar{\sigma}(\kappa) \quad (2.48)$$

with the second invariant of the deviatoric stress tensor J_2 and the linearly descending relation between the yield strength $\bar{\sigma}$ and the hardening parameter κ as in Fig. 2.2. Three meshes with 6×12 , 12×24 and 24×48 selectively integrated four-noded elements are analyzed. To initiate a shear band an area in the bottom left-hand corner of the sample is assigned a slightly lower yield strength σ_y (the imperfect area is the same for each mesh).

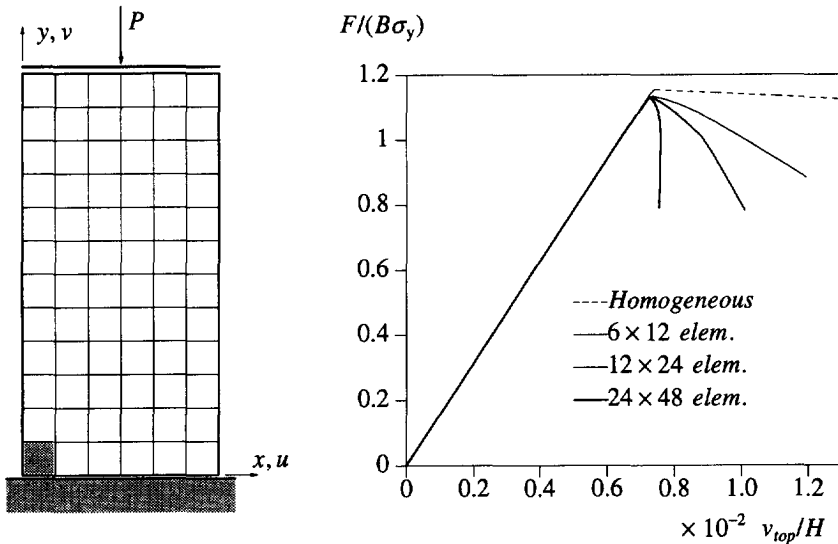


Figure 2.5 Biaxial test configuration (with dimensions $B \times H$ and an imperfection in the bottom left-hand corner) and load-displacement diagrams for three mesh refinements.

It is clearly seen from the load-displacement diagram in Fig. 2.5 that the inclination of the post-peak branch is different for each mesh. Fig. 2.6 shows that the shear band always occupies the smallest possible area. Upon mesh refinement the analytical solution for a standard continuum, i.e. localization in a line is approached. Notice that a large scaling factor is used for the incremental deformations in Fig. 2.6.

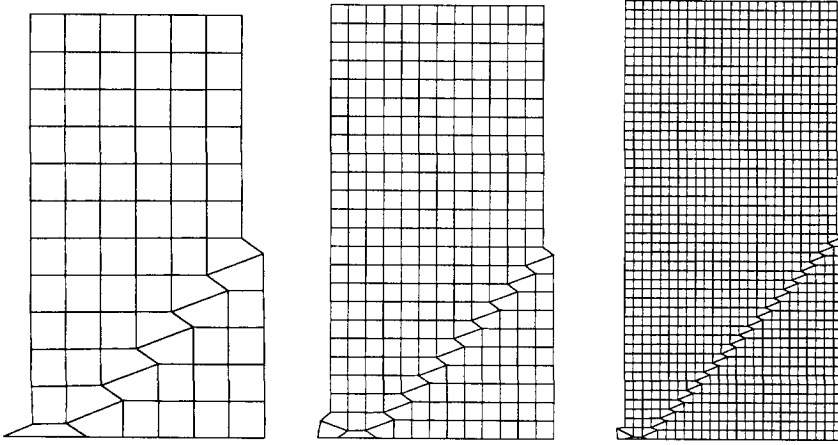


Figure 2.6 Mesh dependence of deformation patterns for classical continuum.

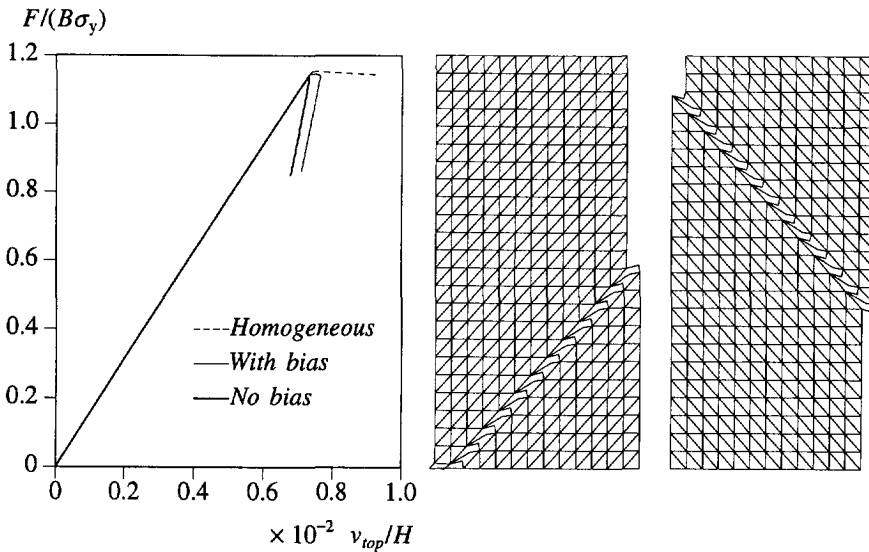


Figure 2.7 Directional bias exhibited by classical continuum elements (imperfection in the bottom left-hand corner for both meshes).

Because of the above phenomenon the results also depend on the arrangement of finite elements, i.e. exhibit a directional bias. Fig. 2.7 shows load-displacement

diagrams and deformation patterns for our problem discretized using six-noded triangles. Two imperfect elements are introduced in the bottom left-hand corner. They initiate a shear band propagating towards the middle of the right-hand side of the specimen. We observe that when the elements are arranged perpendicularly to this direction, localization is delayed. After some accumulation of plastic strains in the area between the imperfect corner and the center of the right-hand side edge of the specimen, a shear band emerges in the upper part along the mesh lines, which is not realistic. Shear bands have thus the incorrect tendency to follow the mesh lines, since in this direction they can be narrower.

It is mentioned in this context, that some finite elements may exhibit strain locking that artificially delays or prevents localization in the narrowest, two-element wide shear band (Steinmann and Willam 1991₁). Therefore it has been suggested to enrich the strain interpolation by incompatible assumed strain functions (Ortiz et al 1987, Fish and Belytschko 1988) and to use an adaptive mesh refinement (Ortiz and Quigley 1990). While the former enhancement improves the element kinematics and the latter is obviously advisable in the presence of large strain gradients, none of them remove the fundamental difficulty associated with the loss of ellipticity.

2.2 Related work and possible solution approaches

2.2.1 Discontinuum versus continuum modelling

In the previous chapter we have shown that within the classical continuum description the strain softening model leads to ill-posed boundary value problems and hence erroneous numerical predictions of localization. This remains true for every type of local continuum model including softening plasticity, continuous damage and smeared cracking.

The problem of material softening and strain localization has been in the focus of theoretical and experimental research during the last ten years. The aim has been to develop reliable phenomenological models (at the macro-level of observation) as well as micromechanical models (at the meso-level) for the analysis of localized deformation. Here we limit the presentation to quasi-brittle and frictional materials like concrete, rock and soil, in which localization takes place in the form of cracks and shear or fracture bands.

Two phenomenological approaches are possible: *discontinuum* modelling and *enhanced continuum* modelling. In the first approach the softening characteristics are attributed to discrete cracks (interfaces), in which continuity of deformation is abandoned. In the second approach the loss of ellipticity of the governing equations is precluded (the equations are regularized, i.e. the possibility of strain localization in a discontinuity is limited by an internal length scale introduced in the continuum description).

In the discontinuum modeling interface elements are introduced between continuum elements. The constitutive relations for the interfaces are written in terms of tractions t

and relative displacements \mathbf{u} of both sides of the interface (Rots 1988, Schellekens 1992):

$$\mathbf{t} = \mathbf{D}^{\text{cr}} \mathbf{u}, \quad (2.49)$$

where the components of the stiffness matrix \mathbf{D}^{cr} (usually assumed to be diagonal) define the softening behaviour and may be related to the energy released in different fracture modes. In the fundamental case of Mode-I crack opening the fracture energy G_f is defined as the amount of energy required to open a unit crack area (cf. Hillerborg et al 1976):

$$G_f = \int \sigma du, \quad (2.50)$$

where σ is the crack normal traction and u is the crack normal displacement (Fig. 2.8). The discontinuum approach is closely related to fracture mechanics and is therefore capable of simulating the deterministic *size effect* (Bažant 1992, Schellekens 1992). The decrease of the load-carrying capacity and of the ductility in the post-peak regime with the increase of the structural size is characteristic for fracturing specimens. The difficulty of the discontinuum modelling lies in the fact, that either the morphology of the cracks must be known a priori, or the interfaces must be assumed between all continuum elements in the potential fracture zone, or that frequent remeshing must be performed during the analysis (Larsson and Runesson 1992).

It is also noted that ‘strong’ discontinuities may also be included in the finite element formulation in the form of internal interfaces (cf. Dvorkin et al 1990, Lotfi and Shing 1994, Oliver and Simo 1994, Olofsson et al 1994). Though the necessity of remeshing is then avoided, this solution involves discontinuous shape functions and seems less natural than the previous one.

On the other hand, it is convenient to remain within the continuum description and use the classical quantities of stress and strain, having now modified definitions in order to reproduce closer the more complex physical reality in degrading materials.

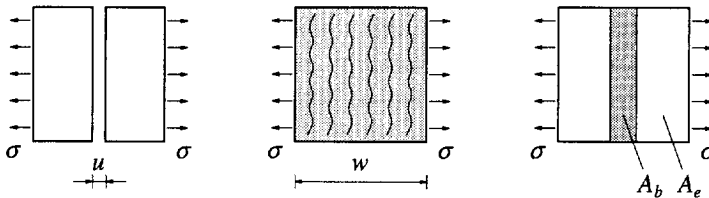


Figure 2.8 Discrete crack and crack band models.

A step in this direction is to relate the classical softening model to the fracture energy treated as a material constant (cf. Bažant and Oh 1983, Willam 1984):

$$G_f = w \int \sigma d\varepsilon, \quad (2.51)$$

where w is the width of the localization zone (the crack band width in terms of the smeared cracking model), in which strains are assumed to be constant, and the integral

is an area under the uniaxial $\sigma - \varepsilon$ (or $\sigma - \varepsilon^p$) diagram. To remedy the spurious mesh dependence of the structural load-deformation response the width w is related to the finite element size (e.g. w is a square root of the element area A_e) and consequently the softening diagram must be adjusted for each finite element mesh. For the uniaxial softening model from Section 2.1.2 we obtain the element size dependent softening modulus h_f :

$$h_f = -\frac{w\sigma_y^2}{2G_f}. \quad (2.52)$$

For the example of a bar in tension in Section 2.1.3 we have $w = L/m$ and the stress-average strain diagram in the post-peak regime has the inclination:

$$\frac{d\bar{\varepsilon}}{d\sigma} = \frac{1}{E} - \frac{2G_f}{L\sigma_y}, \quad (2.53)$$

so that the response depends only on the material properties and the structural size. The results are thus mesh-insensitive and the size effect can be reproduced, but the fracture energy release still takes place in a different area for each mesh, since the loss of ellipticity is not prevented.

A version of the fracture energy approach assumes a localization band embedded in a finite element (Pietruszczak and Mróz 1981) and a modification of the softening modulus according to the area fraction A_b occupied by the band (Fig. 2.8):

$$h_f = \frac{A_e}{A_b} h. \quad (2.54)$$

Applicability of the fracture energy approaches is obviously limited to the cases of cracking and very narrow shear bands ($A_b \leq A_e$).

In an enhanced continuum approach either the continuum kinematics must incorporate the evolution of microstructures or the macroscopic constitutive relations must be nonlocal (de Borst et al 1993). This essentially means a departure from the notion of a simple solid. In contradiction to the definition in eq. (2.1) we now admit that the stress tensor at a material point ξ depends on the motion history of all the material points η in a certain neighbourhood of the point ξ (cf. Becker & B urger 1975):

$$\sigma(\xi, t) = \psi(\xi, \mathbf{x}(\eta, t - \tau)), \quad 0 \leq \tau < \infty, \quad (2.55)$$

where ψ is a *nonlocal* constitutive functional, which may have the form of an integral (an explicit dependence on time or temperature has been neglected). Making use of the principle of material objectivity the functional ψ can be shown to depend only on the relative motion of the points η and ξ , which can be approximated by a Taylor series around ξ :

$$\mathbf{x}(\eta, t) - \mathbf{x}(\xi, t) = \mathbf{F}(\xi, t)(\eta - \xi) + \frac{1}{2} \mathbf{F}_2(\xi, t)(\eta - \xi)^2 + \dots + \frac{1}{n!} \mathbf{F}_n(\xi, t)(\eta - \xi)^n, \quad (2.56)$$

where \mathbf{F}_2 denotes the second order deformation gradient $\partial^2 \mathbf{x} / \partial \xi^2$ and \mathbf{F}_n accordingly the n -th order gradient. We obtain the constitutive relation of a so-called *grade- n* continuum:

$$\sigma(\xi, t) = \psi(\xi, \mathbf{F}(\xi, t - \tau), \mathbf{F}_2(\xi, t - \tau), \dots, \mathbf{F}_n(\xi, t - \tau)), \quad 0 \leq \tau < \infty. \quad (2.57)$$

Three enhanced continuum approaches have so far proved successful (de Borst et al 1993):

- Cosserat (micropolar) continuum,
- nonlocal (integral) model,
- higher-order gradient continuum.

Below we will summarize the first two ideas and show that they both introduce an internal length scale. The third approach will be presented in detail in Chapter 3.

In this thesis we limit ourselves to static localization problems. In the dynamic context the onset of localization in a classical continuum is associated with the emergence of stationary waves and loss of hyperbolicity of the equations of motion. A thorough analysis of the wave propagation in softening media and regularization methods has been presented by Sluys (1992). It is noted that in addition to the above mentioned localization limiters, incorporation of the strain rate dependence (e.g. the viscoplastic model, cf. Needleman 1988, Simo 1989) can also preserve well-posedness of the governing equations and can solve the problem of spurious mesh-sensitivity of numerical results.

2.2.2 Micropolar continuum

The idea of the Cosserat (micropolar) continuum (see e.g. Eringen 1968) is based on the assumption that the forces exerted by one part of a body on another part can be represented on a section surface element by a stress vector (traction) and a couple-stress (Fig. 2.9). This couple-stress is responsible for the existence of microcurvatures supplementing the classical normal and shear strains.

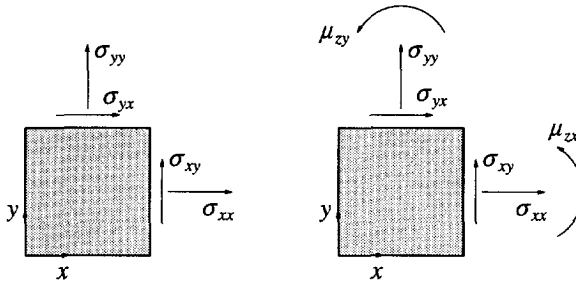


Figure 2.9 Stress components for classical and micropolar continuum.

For a two-dimensional configuration in the (x, y) -plane we have the following microcurvature definitions:

$$\kappa_{zx} = \frac{\partial \omega_z}{\partial x}, \quad \kappa_{zy} = \frac{\partial \omega_z}{\partial y}, \quad (2.58)$$

where ω_z is a microrotation around the z -axis. It is assumed that the couple-stresses μ_{zx} and μ_{zy} are proportional to the respective microcurvatures:

$$\mu_{zx} = Gl^2 \kappa_{zx}, \quad \mu_{zy} = Gl^2 \kappa_{zy}, \quad (2.59)$$

where G is the elastic shear modulus and l is an internal length of the material. From the rotational equilibrium of a material element it can be observed that the stress tensor is nonsymmetric ($\sigma_{yx} \neq \sigma_{xy}$).

The elastic Cosserat continuum theory has been extended to elasto-plasticity and applied in the analysis of strain localization (Mühlhaus and Vardoulakis 1987, de Borst 1991₂, 1993, Steinmann and Willam 1991₂). It is noted that it has been possible to preserve the algorithmic format of classical plasticity and use standard C^0 -continuous finite elements with additional rotational degrees of freedom. The presence of microrotations is especially relevant for granular materials (soils) and the internal length has been shown to determine the thickness of shear bands (Mühlhaus and Vardoulakis 1987). The applicability of this theory is however limited to the cases when the rotational degrees of freedom are activated during the deformation. Therefore the micropolar continuum enhancement is a proper regularization method for shear dominated problems and fails in case of pure tension (decohesion problems).

If we assume that the microrotation ω_z is equal to the local rigid rotation (cf. Mindlin 1962):

$$\omega_z = \frac{1}{2} \left(\frac{\partial v}{\partial x} - \frac{\partial u}{\partial y} \right), \quad (2.60)$$

where u and v are the displacements in the x and y direction, respectively, we can write the microcurvatures as:

$$\kappa_{zx} = \frac{1}{2} \left(\frac{\partial^2 v}{\partial x^2} - \frac{\partial^2 u}{\partial x \partial y} \right), \quad \kappa_{zy} = \frac{1}{2} \left(\frac{\partial^2 v}{\partial x \partial y} - \frac{\partial^2 u}{\partial y^2} \right). \quad (2.61)$$

Substitution of the above formulas in eq. (2.59) shows that second order deformation gradients are incorporated in the formulation, and therefore such a micropolar continuum is a special case of a grade-2 continuum, cf. eq. (2.57).

2.2.3 Nonlocal integral models

The nonlocal continuum approach (see e.g. Eringen and Edelen 1972, Bažant et al 1984) is based on spatial averaging of tensor or scalar state variables (strains, stresses, inelastic strain or damage measures) in a certain neighbourhood of a given point. With the aid of a weighting function $g(\mathbf{s})$ a nonlocal quantity \bar{Y} is defined as:

$$\bar{Y}(\mathbf{x}) = \frac{1}{V_g} \int_V Y(\mathbf{x} + \mathbf{s}) g(\mathbf{s}) dV, \quad V_g = \int_V g(\mathbf{s}) dV, \quad (2.62)$$

where the weighting function is normalized with its integral so that we have $\bar{Y} = Y$ if $Y(\mathbf{x})$ is constant. The weighting function is for instance taken as the Gauss error function:

$$g(\mathbf{s}) = \exp\left(-\frac{|\mathbf{s}|^2}{2l^2}\right), \quad (2.63)$$

which decays with the distance $|\mathbf{s}|$ from the point \mathbf{x} . In formula (2.63) the parameter l

plays the role of an internal length scale, since l determines the size of the neighbourhood of the point \mathbf{x} which affects the nonlocal function $\bar{Y}(\mathbf{x})$.

We will now consider the nonlocal quantity $\bar{Y}(x)$ for an infinite one-dimensional domain. According to eqs (2.62) and (2.63) we have:

$$\bar{Y}(x) = \frac{1}{l\sqrt{2\pi}} \int_{-\infty}^{\infty} \exp\left(\frac{-s^2}{2l^2}\right) Y(x+s) ds . \quad (2.64)$$

We develop the function $Y(x+s)$ in a Taylor series around $s=0$:

$$\begin{aligned} \bar{Y}(x) = \frac{1}{l\sqrt{2\pi}} & \left[\int_{-\infty}^{\infty} \exp\left(\frac{-s^2}{2l^2}\right) Y(x) ds + \int_{-\infty}^{\infty} s \exp\left(\frac{-s^2}{2l^2}\right) \frac{dY(x)}{dx} ds + \int_{-\infty}^{\infty} \frac{s^2}{2} \exp\left(\frac{-s^2}{2l^2}\right) \frac{d^2Y(x)}{dx^2} ds \right. \\ & \left. + \int_{-\infty}^{\infty} \frac{s^3}{6} \exp\left(\frac{-s^2}{2l^2}\right) \frac{d^3Y(x)}{dx^3} ds + \int_{-\infty}^{\infty} \frac{s^4}{24} \exp\left(\frac{-s^2}{2l^2}\right) \frac{d^4Y(x)}{dx^4} ds + \dots \right] \end{aligned} \quad (2.65)$$

and after analytical integration we obtain the formula:

$$\bar{Y}(x) = Y(x) + \frac{l^2}{4} \frac{d^2Y(x)}{dx^2} + \frac{l^4}{16} \frac{d^4Y(x)}{dx^4} + \dots , \quad (2.66)$$

which includes only even order derivatives of the averaged quantity Y at the point x . If the averaging procedure is applied to the strain $Y = \varepsilon$ (or inelastic strain) in a bar with the length L much larger than the internal length l , we observe that the nonlocal relation (2.64) introduces higher order deformation gradients in the formulation.

In the application to strain localization problems the nonlocal (integral) regularization has been most conveniently introduced in the damage theory (Bažant and Pijaudier-Cabot 1988, Pijaudier-Cabot and Benallal 1993). For instance the constitutive relation for the isotropic damage theory (in terms of total quantities)

$$\boldsymbol{\sigma} = (1 - \omega) \mathbf{D}^e \boldsymbol{\varepsilon} \quad (2.67)$$

includes a scalar damage parameter ω , which grows from zero to one and accounts for the degradation of the elastic stiffness matrix. The damage growth is determined by an evolution law:

$$\dot{\omega} = f(\varepsilon^{eq}) , \quad (2.68)$$

in which ε^{eq} is the equivalent strain measure defined as (Mazars and Pijaudier-Cabot 1989):

$$\varepsilon^{eq} = \left[\sum_{i=1}^3 \langle \varepsilon_i \rangle^2 \right]^{1/2} , \quad (2.69)$$

where ε_i are the principal strains, $\langle \varepsilon_i \rangle = \varepsilon_i$ if $\varepsilon_i > 0$ and $\langle \varepsilon_i \rangle = 0$ otherwise. Alternatively ε^{eq} can be a damage energy release rate (Bažant and Pijaudier-Cabot 1988):

$$\varepsilon^{eq} = \frac{1}{2} \boldsymbol{\varepsilon}^T \mathbf{D}^e \boldsymbol{\varepsilon} . \quad (2.70)$$

Suitable loading/unloading conditions are formulated in the strain space similarly to the plasticity theory. In particular the damage grows if the loading condition:

$$F(\varepsilon^{\text{eq}}, K) = \varepsilon^{\text{eq}} - K = 0 \quad (2.71)$$

is fulfilled, where the damage parameter K initially equals the damage threshold level K_0 and during the damage process equals the largest value of ε^{eq} reached during the loading history.

To obtain a nonlocal model either ε^{eq} or the damage ω are replaced by the averaged quantities $\bar{\varepsilon}^{\text{eq}}$ or $\bar{\omega}$ according to eq. (2.62), while all the other quantities remain local. In finite element implementation an additional loop over the elements is required to determine the nonlocal quantity, but standard C^0 -continuous elements can be used.

The microplane model (Bažant and Ožbolt 1990), which combines the volumetric, deviatoric and shear components of the microplane damage response in order to obtain a macroscopic stress-strain relation has been generalized to a nonlocal continuum model by making the strain tensor nonlocal. The averaging procedure has also been applied to the plastic strain tensor (or an invariant plastic strain measure) to obtain a nonlocal yield limit degradation model (Bažant and Lin 1988). However, within the flow plasticity theory an integro-differential consistency condition is then obtained, which cannot be solved easily and makes the implementation awkward (cf. de Borst et al 1993).

If the averaging domain extends to the outside of the given body, the problem of additional boundary conditions occurs. To illustrate this issue we analyze the one-dimensional example of a bar in tension from Chapter 2.1 (Fig. 2.3) and incorporate a nonlocal plastic strain $\bar{\varepsilon}^{\text{p}}$, which is calculated for simplicity as a spatial average of the local plastic strain over a given length a :

$$\bar{\varepsilon}^{\text{p}}(x) = \frac{1}{a} \int_{-a/2}^{a/2} \varepsilon^{\text{p}}(x+s) ds, \quad (2.72)$$

which is equivalent to taking a unit block weighting function in the neighbourhood $[-a/2; a/2]$ of the current point x (we note that this choice is not optimal for convergence, Bažant and Pijaudier-Cabot 1988). In a numerical implementation the plastic strain distribution $\varepsilon^{\text{p}}(x)$ as in Fig. 2.4 is calculated from the yield condition (2.32). Then in an extra loop the nonlocal (smoothed) plastic strain function may be determined from eq. (2.72) and used for the strain and stress update. However, the nonlocal plastic strain does not satisfy the yield condition (2.32), which can be written as:

$$\sigma = \sigma_y + h \bar{\varepsilon}^{\text{p}} = \sigma_y + \frac{h}{a} \int_{-a/2}^{a/2} \varepsilon^{\text{p}}(x+s) ds. \quad (2.73)$$

Since the stress is calculated from eqs (2.30-2.31) as $\sigma = E(\varepsilon - \varepsilon^{\text{p}})$, we obtain an integral equation in ε^{p} as follows:

$$\varepsilon^{\text{p}}(x) = \varepsilon(x) - \frac{\sigma_y}{E} - \frac{h}{aE} \int_{-a/2}^{a/2} \varepsilon^{\text{p}}(x+s) ds. \quad (2.74)$$

If we then approximate the integral by a finite sum with the weight factors w_j :

$$\varepsilon^{\text{p}}(x_i) = \varepsilon(x_i) - \frac{\sigma_y}{E} - \frac{h}{aE} \sum_{j=1}^n w_j \varepsilon^{\text{p}}(x_i + s_j), \quad (2.75)$$

we can observe that for $x_i + s_j$ larger than the bar length L the plastic strain ϵ^p is not defined. It is also visible that an iterative process is necessary to satisfy eq. (2.75), since at the moment of calculation of $\epsilon^p(x_i)$ the updated values of ϵ^p are known only for $s_j < 0$.

The nonlocal approach is appealing from a physical point of view and has a convincing micromechanical motivation (Bažant 1994, Ožbolt et al 1994). A general constitutive law as follows is considered:

$$\Delta\sigma = \mathbf{D}^e \Delta\epsilon - \Delta\bar{\mathbf{S}}, \quad (2.76)$$

where $\Delta\bar{\mathbf{S}}$ is a spatial averaging of the inelastic stress increment tensor $\Delta\mathbf{S}$ according to eq. (2.62). The nonlocality of the inelastic stress increment is substantiated by interaction of growing microcracks.

In the micromechanical argument an increment of imposed deformations is decomposed into two steps: the first with temporarily ‘frozen’ microcracks, and the second with the crack growth (propagation and opening) and formation of new microcracks. During the second step surface tractions are applied on the crack faces to relax the stresses transmitted across the cracks in the first step. The first step corresponds to the elastic predictor in the macro-model of eq. (2.76) (segment 1-3 in Fig. 2.10) and the second step is related to the inelastic stress relaxation term.

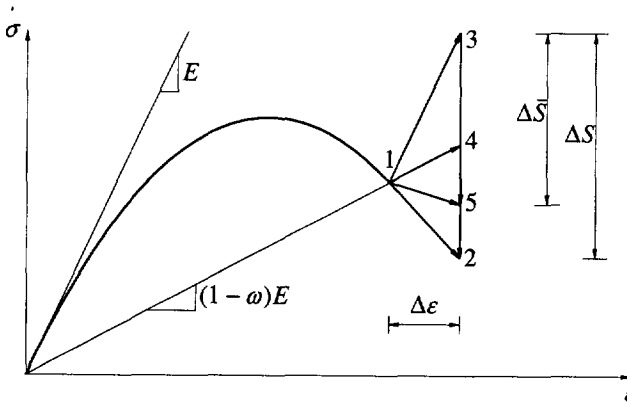


Figure 2.10 Local and nonlocal inelastic stress increments (based on Bažant 1994).

If the damage state does not change during the strain increment, i.e. if no microcracks initiate or grow, the stress drop to point 4 determined by the secant stiffness takes place. Since the process of crack formation and propagation continues during the step, the stress relaxation is larger. In case of local strain softening relation the stress drop to point 2 is obtained, and when the microcrack interactions are incorporated the stress is relaxed to point 5.

In the proposed nonlocal model (Bažant 1994) the maximum principal inelastic stress $\Delta\bar{S}_1$ at a point is shown to be a continuum counterpart of an average normal traction of a microcrack located at this point. This traction is composed of an average

traction, obtained when all the other cracks are 'frozen', and contributions due to the evolution of all the other cracks (determined by crack influence coefficients). The continuum formulation of the problem leads to an integral equation in $\Delta\bar{S}_1$, which includes short-range inelastic stress averaging and long-range microcrack interactions. This approach is a generalization of the nonlocal damage model (Bažant and Pijaudier-Cabot 1988).

The nonlocal damage model has been combined with a stochastic approach to determine the structural reliability in presence of localization (Carmeliet 1992). Because of a random distribution of material properties and initial defects, a heterogeneous continuum can be realistically described by stochastic variables. Random fields of material properties (e.g. the damage threshold K_0 and the ultimate value of ϵ^{eq}) are described by their distribution and mutual correlations in space. The correlation function has a form similar to (2.63) and hence introduces a length parameter defining the distance beyond which the correlation is not important. The failure probability (or reliability) may be determined using the Monte Carlo technique, in which the response of a large number of similar samples is simulated. It has been shown (Carmeliet and de Borst 1994), that the introduction of the spatial correlation distance in the stochastic description is not sufficient to regularize the governing equations and incorporation of a localization limiter (e.g. nonlocal damage averaging) is necessary to avoid the spurious discretization sensitivity.

3. Gradient-dependent softening plasticity theory

3.1 Essentials of the theory

In order to obtain a meaningful representation of the continuum response in the presence of strain softening and localization, the governing partial differential equations must be regularized. It means ellipticity must be preserved in the static case (which guarantees the continuity of the solution) and an internal length scale must be introduced (which defines the size of the localization zone). To achieve this goal an enhanced continuum theory can be used.

In Chapter 2.2 we have observed that the grade- n continuum may be conceived as an approximation of the general nonlocal constitutive law. We have also shown that the nonlocal integral model and the Cosserat continuum model introduce higher-order (inelastic) deformation gradients in the formulation. Since both these approaches have a clear micromechanical interpretation, we can associate the presence of higher-order gradients in a macroscopic constitutive model with the (nonlocal) interaction between microstructural deformation carriers.

We now focus our interest on the gradient-dependent continuum formulation. Incorporation of the gradient-dependence into (large deformation) plasticity theory has been made plausible by consideration of dislocation motion and evolution (Aifantis 1984,1987). The gradient-dependence has first been used within the theory of rigid-plastic material for the analysis of persistent slip bands (Aifantis 1984,1987) and shear bands (Coleman and Hodgdon 1985) in metals. The second order derivative of an accumulated shear strain $\bar{\gamma}$ has been included in the shear stress-strain rate equation (Coleman and Hodgdon 1985) in accordance with the material frame indifference argument:

$$\tau = \left[\bar{\tau}(\bar{\gamma}) - c \frac{d^2 \bar{\gamma}}{dx^2} \right] \frac{\dot{\gamma}}{|\dot{\gamma}|}, \quad (3.1)$$

where τ is the shear stress, $\dot{\gamma}$ the shear strain rate, $\bar{\tau}(\bar{\gamma})$ is the yield stress and c is a positive phenomenological constant. This approach has been used as a localization limiter by Belytschko and Lasry (1989) and the constitutive law has been written in a uniaxial case as follows:

$$\sigma = f(\varepsilon) - c \frac{d^2 \varepsilon}{dx^2}, \quad c > 0, \quad (3.2)$$

where $f(\varepsilon)$ defines a nonlinear relation.

In a more general approach the Laplacian of an effective deformation measure γ has been included in the yield condition (Zbib and Aifantis 1988), which has been written as:

$$\tau = \bar{\tau}(\gamma) - c \nabla^2 \gamma, \quad c > 0, \quad (3.3)$$

where τ is the second invariant of the deviatoric stress tensor and $\bar{\tau}(\gamma)$ is the hardening law. Gradients of higher order (when isotropy is assumed only even orders are relevant) have been introduced in the yield function (Zbib and Aifantis 1988, Mühlhaus and

Aifantis 1991). The dependence of the hardening law on the first-order gradient of an inelastic strain invariant has also been examined (Schreyer and Chen 1986).

For the analysis of shear bands in granular materials the gradient dependence has been postulated in both the flow rule (Vardoulakis and Aifantis 1991):

$$\dot{\varepsilon}^p = \beta(\gamma^p)\dot{\gamma}^p - d\nabla^2\dot{\gamma}^p, \quad d > 0, \quad (3.4)$$

in which $\dot{\varepsilon}^p$ is the volumetric plastic strain rate, $\dot{\gamma}^p$ is the shear plastic strain rate and β is the dilatancy coefficient, and in the Coulomb yield condition:

$$\tau/p = \mu(\gamma^p) - c\nabla^2\gamma^p, \quad c > 0, \quad (3.5)$$

where p is the mean pressure and μ is the friction coefficient. It has been shown (Vardoulakis and Aifantis 1991) that the modified flow rule and yield condition are coupled and the constants d and c are related to a unique internal length. In principle it can be associated with the grain size, but general theories or experimental data concerning this association do not seem to have appeared yet.

In this thesis we make use of a gradient-dependent plasticity theory (de Borst and Mühlhaus 1991, 1992), in which the yield condition is similar to eq. (3.3):

$$\phi(\sigma) = \bar{\sigma}(\kappa) - g\nabla^2\kappa, \quad (3.6)$$

where $\phi(\sigma)$ is an equivalent stress (e.g. $\sqrt{3J_2}$ for Huber-Mises plasticity), κ is an invariant plastic strain measure, $\bar{\sigma}$ is the yield strength (isotropic softening is assumed) and g is a positive coefficient with the dimension of force. It is emphasized that the gradient terms disappear from the constitutive equations if a homogeneous state of strain and stress is analyzed. In this sense they can be treated as a singular perturbation of the standard equations. The gradient terms are negligible if strains vary slowly in space (in the pre-peak regime of softening problems), but have a significant influence in the presence of strain localization (in the post-peak regime).

Before presenting the general theory and rate boundary value problem, we will illustrate the introduction of the second order gradient in a simple uniaxial problem and present the analytical solution. We will also prove the stabilizing and regularizing effect of this enhancement in the elasto-plastic continuum theory.

3.1.1 Analytical solution for one-dimensional case

We analyze again the one-dimensional example of a bar in tension from Chapter 2.1 and we include the nonlocal plastic strain $\bar{\varepsilon}^p$ from eq. (2.72) in the derivation. Seeking a more efficient approach than the nonlocal integral model we develop the function $\varepsilon^p(x+s)$ in a Taylor series around $s=0$ and obtain:

$$\begin{aligned} \bar{\varepsilon}^p(x) &= \frac{1}{a} \int_{-a/2}^{a/2} [\varepsilon^p(x) + \varepsilon^{p'}(x)s + \frac{1}{2}\varepsilon^{p''}(x)s^2 + \dots] ds \approx \\ &\approx \frac{1}{a} \left[\varepsilon^p(x)s + \frac{1}{2}\varepsilon^{p'}(x)s^2 + \frac{1}{6}\varepsilon^{p''}(x)s^3 \right]_{-a/2}^{a/2} = \varepsilon^p(x) + \frac{a^2}{24}\varepsilon^{p''}(x), \end{aligned} \quad (3.7)$$

where ' denotes differentiation with respect to x and the fourth and higher order terms

have been neglected. In fact, the derivation is strict only when the averaging is performed inside the bar, and if the higher order terms are negligible (Huerta and Pijaudier-Cabot, 1994). From eq. (3.7) we notice that the difference between the plastic strain function and its average over a certain length is approximately proportional to the second order gradient of the function:

$$\bar{\varepsilon}^p(x) \approx \varepsilon^p(x) + l^2 \varepsilon^{p''}(x), \quad (3.8)$$

and the proportionality factor can be associated with a length scale l .

Now we want to find a plastic strain function $\varepsilon^p(x)$ such that the average plastic strain fulfils immediately the yield condition:

$$\sigma = \sigma_y + h \bar{\varepsilon}^p, \quad (3.9)$$

where h is the softening modulus, assumed to be negative and constant. We substitute eq. (3.8) into eq. (3.9) and we obtain a gradient-dependent yield condition:

$$\sigma = \sigma_y + h \varepsilon^p + hl^2 \varepsilon^{p''}. \quad (3.10)$$

Comparing this equation with the gradient-dependent yield condition in eq. (3.6) we observe that the length scale l is related to the gradient-dependence coefficient g by

$$g = -hl^2, \quad l = \sqrt{-g/h}. \quad (3.11)$$

Eq. (3.10) is an inhomogeneous second order ordinary differential equation:

$$l^2 \varepsilon^{p''} + \varepsilon^p = \frac{\sigma - \sigma_y}{h}. \quad (3.12)$$

We assume localization of plastic strains within a length w in the centre of the beam (Fig. 3.1). Using the boundary condition that $\varepsilon^p = 0$ for $x = \pm w/2$ and assuming symmetry of the plastic strain distribution with respect to $x = 0$ the solution of eq. (3.12) can be derived as (cf. de Borst and Mühlhaus 1992):

$$\varepsilon^p = \frac{\sigma - \sigma_y}{h} \left[1 - \frac{\cos(x/l)}{\cos(w/2l)} \right]. \quad (3.13)$$

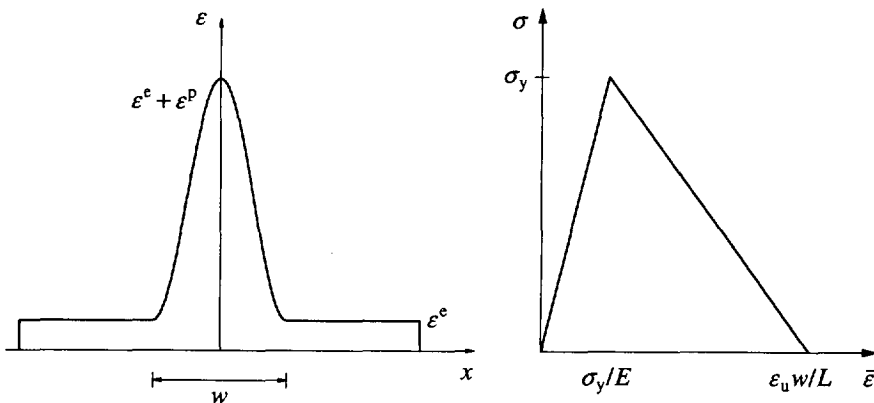


Figure 3.1 Bar response for gradient-dependent material.

Next, we determine the response of the beam in terms of stress and average strain. We calculate the displacement of the right end of the bar \bar{u} :

$$\bar{u} = \int_{-L/2}^{L/2} \varepsilon^e dx + \int_{-w/2}^{w/2} \varepsilon^p dx, \quad (3.14)$$

substitute $\varepsilon^e = \sigma/E$ and eq. (3.13) and divide by the length of the bar L :

$$\bar{\varepsilon} = \frac{\bar{u}}{L} = \frac{\sigma}{E} + \frac{\sigma - \sigma_y}{Lh} [w - 2l \tan(w/2l)]. \quad (3.15)$$

So far the values of the internal length scale l and the width of the localization zone w have not been related. However, we are interested in the most critical solution, i.e. the one that gives the steepest $\sigma - \bar{\varepsilon}$ diagram. This gives the following condition for w :

$$\frac{d\bar{\varepsilon}}{dw} = 0, \quad (3.16)$$

which leads to the equation

$$\cos^2(w/2l) = 1. \quad (3.17)$$

This equation has the smallest non-trivial solution $w/2l = \pi$, so that

$$w = 2\pi l. \quad (3.18)$$

For this width of the localization zone the plastic strain function reads:

$$\varepsilon^p = \frac{\sigma - \sigma_y}{h} [1 + \cos(x/l)] \quad (3.19)$$

and we observe that the function is at least C^1 -continuous ($\varepsilon^{p'} = 0$ for $x = \pm w/2$). Substitution of eq. (3.18) into eq. (3.15) gives:

$$\bar{\varepsilon} = \frac{\sigma}{E} + \frac{\sigma - \sigma_y}{h} \frac{2\pi l}{L} \quad (3.20)$$

and the inclination of the post-peak branch in Fig. 3.1 can be calculated as:

$$\frac{d\bar{\varepsilon}}{d\sigma} = \frac{1}{E} + \frac{2\pi}{h} \frac{l}{L}. \quad (3.21)$$

The solution is obviously governed by the ratio of the internal length l and the structural size L and therefore the size effect is incorporated in the model. It is also noted that for small values of l and large values of L (when $l/L < -h/(2\pi E)$) we obtain a *snap-back* response, which means that both the stress and strain decrease with the increase of loading.

If we treat ε^p as a plastic strain measure and σ as an equivalent stress, we can obtain a similar solution for the case of a bar in pure shear (Pamin and de Borst 1992).

3.1.2 Material stability and ellipticity

Considering further the uniaxial example from the previous section, we take the rate form of eq. (3.10):

$$\dot{\sigma} = h \dot{\varepsilon}^p + hl^2 \dot{\varepsilon}^{p''} \quad (3.22)$$

and calculate the second order work according to the material stability condition (2.9). The destabilizing effect of softening is introduced only by the plastic (inelastic) action and the work corresponding to the plastic strains ε^p equals:

$$\int_{-L/2}^{L/2} \dot{\sigma} \varepsilon^p dx = \int_{-w/2}^{w/2} [h(\dot{\varepsilon}^p)^2 + hl^2 \dot{\varepsilon}^{p''} \dot{\varepsilon}^p] dx = \int_{-w/2}^{w/2} h(\dot{\varepsilon}^p)^2 dx - \int_{-w/2}^{w/2} hl^2 (\dot{\varepsilon}^{p'})^2 dx, \quad (3.23)$$

where the boundary condition $\dot{\varepsilon}^p = 0$ for $x = \pm w/2$ has been used. We observe that for $h < 0$ the first term in eq. (3.23) introduces instability, while the second (gradient) term acts as a stabilizer. On the other hand for $h > 0$ (hardening) the gradient term would act in a destabilizing manner. For this reason an independent positive gradient coefficient has been introduced in eqs (3.1-3.6), cf. Mühlhaus and Aifantis (1991). In eq. (3.6) we have $g = -hl^2$ in case of softening, while for hardening $g = +hl^2$ in order that the second term in eq. (3.23) acts as a stabilizer.

Next, we write the assumed yield condition (3.6) in the form:

$$F = \phi(\boldsymbol{\sigma}) - \bar{\sigma}(\kappa) + g \nabla^2 \kappa = 0 \quad (3.24)$$

and notice that the consistency argument now yields the following equation:

$$\dot{F} = \mathbf{n}^T \dot{\boldsymbol{\sigma}} - h \dot{\lambda} + g \nabla^2 \dot{\kappa} = 0, \quad (3.25)$$

where \mathbf{n} and h have been defined in eqs (2.39-2.40). We calculate $\dot{\lambda}$ from eq. (3.25) and substitute into the constitutive relation, see eq. (2.35):

$$(\mathbf{D}^e)^{-1} \dot{\boldsymbol{\sigma}} = \dot{\boldsymbol{\varepsilon}} - \dot{\lambda} \mathbf{m}. \quad (3.26)$$

After regrouping we obtain:

$$\dot{\boldsymbol{\varepsilon}} - \frac{g}{h} \nabla^2 \dot{\kappa} \mathbf{m} = [(\mathbf{D}^e)^{-1} + \frac{1}{h} \mathbf{m} \mathbf{n}^T] \dot{\boldsymbol{\sigma}} \quad (3.27)$$

and with the aid of the Sherman-Morrison formula:

$$\dot{\boldsymbol{\sigma}} = \left(\mathbf{D}^e - \frac{\mathbf{D}^e \mathbf{m} \mathbf{n}^T \mathbf{D}^e}{h + \mathbf{n}^T \mathbf{D}^e \mathbf{m}} \right) \left(\dot{\boldsymbol{\varepsilon}} - \frac{g}{h} \nabla^2 \dot{\kappa} \mathbf{m} \right). \quad (3.28)$$

This modified elasto-plastic stress-strain relation can be written as

$$\dot{\boldsymbol{\sigma}} = \mathbf{D}^{ep} \dot{\boldsymbol{\varepsilon}} + g \nabla^2 \dot{\kappa}, \quad (3.29)$$

with the standard tangent stiffness matrix \mathbf{D}^{ep} and the vector \mathbf{g} as follows:

$$\mathbf{D}^{ep} = \mathbf{D}^e - \frac{\mathbf{D}^e \mathbf{m} \mathbf{n}^T \mathbf{D}^e}{h + \mathbf{n}^T \mathbf{D}^e \mathbf{m}}, \quad \mathbf{g} = -g \frac{\mathbf{D}^e \mathbf{m}}{h + \mathbf{n}^T \mathbf{D}^e \mathbf{m}}. \quad (3.30)$$

In analogy to the ellipticity analysis in Section 2.1.2 we now consider the possibility of emergence of a discontinuity across a plane with a normal ν_i , which in addition to a jump in the deformation gradient involves a jump in the second order gradient of the equivalent plastic strain (cf. Willam and Dietsche 1992). The first jump can be represented as in eq. (2.25) and the second can be written as follows:

$$[[\nabla^2 \dot{\kappa}]] = \nu_k \alpha_k, \quad (3.31)$$

with an arbitrary vector α_k . Using the equilibrium condition (2.27), which requires the

continuity of tractions across the discontinuity plane, and the elasto-plastic constitutive relation (3.29) written in the tensor form:

$$\dot{\sigma}_{ij} = D_{ijkl} \dot{\epsilon}_{kl} + g_{ij} \nabla^2 \dot{\kappa} , \quad (3.32)$$

we can write:

$$[[\dot{i}_j]] = v_i [[\dot{\sigma}_{ij}]] = (v_i D_{ijkl} v_l) \mu_k + (v_i g_{ij} v_k) \alpha_k = 0 . \quad (3.33)$$

Emergence of the discontinuity plane is possible only if, for arbitrary μ_k and α_k , both contributions in eq. (3.33) vanish simultaneously. This does not normally happen except possibly for some special structure of the constitutive operator. Since violation of the bifurcation condition as defined by eqs. (2.23) and (2.27) guarantees ellipticity, we conclude that the gradient-dependence has a regularizing effect. Consequently the rate boundary value problem for a gradient-dependent elasto-plastic continuum remains well-posed in the softening regime and localization in a set of measure zero is prevented.

It is noted that for the gradient dependent continuum the critical value of the hardening modulus and the direction of the localization band, defined in Chapter 2.1, can be determined from the classical condition of the acoustic tensor singularity (2.29), since prior to the moment of bifurcation into a localized deformation pattern the gradient terms have no influence on the solution.

3.2 Rate boundary value problem

We now present the rate boundary value problem of gradient plasticity (cf. de Borst and Mühlhaus 1991, 1992). We introduce the displacement vector $\mathbf{u} = (u_x, u_y, u_z)$, the strain tensor in a vector form $\boldsymbol{\varepsilon} = (\varepsilon_{xx}, \varepsilon_{yy}, \varepsilon_{zz}, \gamma_{xy}, \gamma_{yz}, \gamma_{zx})$ and the stress tensor in a vector form $\boldsymbol{\sigma} = (\sigma_{xx}, \sigma_{yy}, \sigma_{zz}, \sigma_{xy}, \sigma_{yz}, \sigma_{zx})$. Under the assumption of small deformations and static loading we have the following equations for an elasto-plastic body occupying a volume V (Fig. 3.2):

$$\mathbf{L}^T \dot{\boldsymbol{\sigma}} + \dot{\mathbf{b}} = \mathbf{0} , \quad (3.34)$$

$$\dot{\boldsymbol{\varepsilon}} = \mathbf{L} \dot{\mathbf{u}} , \quad (3.35)$$

$$\dot{\boldsymbol{\sigma}} = \mathbf{D}^e (\dot{\boldsymbol{\varepsilon}} - \dot{\lambda} \mathbf{m}) , \quad (3.36)$$

where superimposed dots denote the derivative with respect to time and the superscript T is the transpose symbol. In the above equations \mathbf{L} is a differential operator matrix:

$$\mathbf{L}^T = \begin{bmatrix} \frac{\partial \cdot}{\partial x} & 0 & 0 & \frac{\partial \cdot}{\partial y} & 0 & \frac{\partial \cdot}{\partial z} \\ 0 & \frac{\partial \cdot}{\partial y} & 0 & \frac{\partial \cdot}{\partial x} & \frac{\partial \cdot}{\partial z} & 0 \\ 0 & 0 & \frac{\partial \cdot}{\partial z} & 0 & \frac{\partial \cdot}{\partial y} & \frac{\partial \cdot}{\partial x} \end{bmatrix} , \quad (3.37)$$

\mathbf{b} is a body-force vector and \mathbf{D}^e is the elastic stiffness matrix (written in terms of Young's modulus E and Poisson's ratio ν):

$$\mathbf{D}^e = \frac{E}{(1+\nu)(1-2\nu)} \begin{bmatrix} 1-\nu & \nu & \nu & 0 & 0 & 0 \\ \nu & 1-\nu & \nu & 0 & 0 & 0 \\ \nu & \nu & 1-\nu & 0 & 0 & 0 \\ 0 & 0 & 0 & \frac{1}{2}(1-2\nu) & 0 & 0 \\ 0 & 0 & 0 & 0 & \frac{1}{2}(1-2\nu) & 0 \\ 0 & 0 & 0 & 0 & 0 & \frac{1}{2}(1-2\nu) \end{bmatrix} \quad (3.38)$$

Eq. (3.36) contains the definition of the plastic strain rate vector, called the flow rule:

$$\dot{\epsilon}^p = \dot{\lambda} \mathbf{m}, \quad \mathbf{m} = \frac{\partial G}{\partial \boldsymbol{\sigma}}, \quad (3.39)$$

in which $\dot{\lambda}$ is a plastic multiplier and \mathbf{m} defines the direction of the plastic flow. The vector \mathbf{m} is derived from a plastic potential function $G = G(\boldsymbol{\sigma})$.

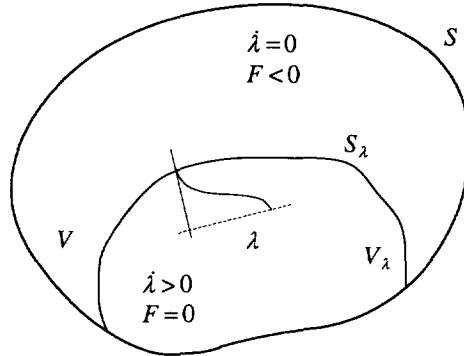


Figure 3.2 Elastic-plastic body.

The gradient dependence is included solely in the definition of the yield function F

$$F = F(\boldsymbol{\sigma}, \kappa, \nabla^2 \kappa), \quad (3.40)$$

in which κ is an invariant plastic strain measure (the hardening parameter). Together with eqs (3.34)-(3.36) the Kuhn-Tucker conditions

$$\dot{\lambda} \geq 0, \quad F \leq 0, \quad \dot{\lambda} F = 0 \quad (3.41)$$

must be fulfilled. To complete the rate boundary value problem we specify the standard static and kinematic boundary conditions on complementary parts of the body surface S :

$$\dot{\boldsymbol{\Sigma}} \mathbf{v}_s = \dot{\mathbf{t}}, \quad \dot{\mathbf{u}} = \dot{\mathbf{u}}_s, \quad (3.42)$$

where $\boldsymbol{\Sigma}$ is the stress tensor in a matrix form, \mathbf{v}_s denotes the outward normal to the surface S and \mathbf{t} is the boundary traction vector. It is mentioned that with the motion equation instead of the equilibrium eq. (3.34) and with additional initial conditions an initial boundary value problem of gradient plasticity can be formulated for dynamic loading (Sluys et al 1993).

In what follows we consider the case of isotropic hardening (softening) and gradient

dependence, so the yield function may be rewritten as

$$F = \phi(\boldsymbol{\sigma}) - \bar{\sigma}_g(\kappa, \nabla^2 \kappa) \quad (3.43)$$

and the yield strength $\bar{\sigma}_g \geq 0$ is gradient-dependent. In general the hardening parameter κ may be a function of plastic strains and stresses:

$$\kappa = \kappa(\boldsymbol{\varepsilon}^p, \boldsymbol{\sigma}) . \quad (3.44)$$

Since this definition would lead to the presence of second order spatial stress gradients in the formulation (while we would like the plastic strains only to be nonlocal), and because of the algorithmic convenience we limit our interest to the yield functions and some form of a strain hardening hypothesis, for which we can write that

$$\dot{\kappa} = \eta \dot{\lambda} , \quad (3.45)$$

with η constant and positive. This definition is broad enough to encompass the Huber-Mises, Drucker-Prager and Rankine yield functions. Their particular forms and definitions of the plastic strain measure will be presented together with the applications in Chapters 5-7.

The gradient dependence of the yield function makes the plastic consistency condition $\dot{F} = 0$ become a differential equation:

$$\left(\frac{\partial F}{\partial \boldsymbol{\sigma}} \right)^T \dot{\boldsymbol{\sigma}} + \frac{\partial F}{\partial \kappa} \dot{\kappa} + \frac{\partial F}{\partial \nabla^2 \kappa} \nabla^2 \dot{\kappa} = 0 . \quad (3.46)$$

We introduce the gradient of the yield function \mathbf{n} :

$$\mathbf{n} = \frac{\partial F}{\partial \boldsymbol{\sigma}} = \frac{\partial \phi}{\partial \boldsymbol{\sigma}} , \quad (3.47)$$

the (variable) hardening modulus h :

$$h(\kappa, \nabla^2 \kappa) = - \frac{\dot{\kappa}}{\dot{\lambda}} \frac{\partial F}{\partial \kappa} = \eta \frac{\partial \bar{\sigma}_g}{\partial \kappa} , \quad (3.48)$$

and the gradient influence variable g :

$$g(\kappa) = \frac{\dot{\kappa}}{\dot{\lambda}} \frac{\partial F}{\partial \nabla^2 \kappa} = - \eta \frac{\partial \bar{\sigma}_g}{\partial \nabla^2 \kappa} , \quad (3.49)$$

which is assumed to be a function of κ only. We can now write eq. (3.46) in the form:

$$\mathbf{n}^T \dot{\boldsymbol{\sigma}} - h \dot{\lambda} + g \nabla^2 \dot{\lambda} = 0 . \quad (3.50)$$

The hardening modulus h is a negative variable and the additional variable g is positive (see Section 3.1.2). It is noted that in the simplest case h and g are constants (softening is linear) and that $g(\kappa)$ will be further treated as a given function (or constant), related to the internal length scale of the modelled material.

For $g = 0$ the classical flow theory of plasticity is retrieved. The consistency condition is then a nonlinear algebraic equation, see eq. (2.38), from which the plastic multiplier can be determined locally. The problem of solving eq. (3.50) is thus characteristic for the present theory. Eq. (3.50) is essentially valid in the plastic part of the body V_λ (Fig. 3.2), but according to eqs (3.41) $\dot{\lambda} = 0$ on the elastic-plastic boundary (internal part of S_λ) and in the elastic subdomain.

Eq. (3.50) is a Helmholtz type of inhomogeneous partial differential equation. An analytical solution of this equation has not been attempted (for a fixed subdomain a solution in terms of eigenfunctions of the homogeneous problem or in terms of Green functions could be proposed), since it is not useful for numerical applications. Consequently we make use of a discretization method. One possibility is to use finite differences (cf. Belytschko and Lasry 1989). The algorithm is then a sequence of separate solutions of the equilibrium problem using finite elements and the plastic yielding problem using finite differences. A more consistent approach, followed in this thesis, is to use only finite element discretization (e.g. the same mesh for the equilibrium and the consistency equations) and solve the two (coupled) problems simultaneously. To achieve this goal, it is necessary to assume the weak satisfaction of the consistency condition and discretize the plastic strain field (cf. Mühlhaus and Aifantis 1991, de Borst and Mühlhaus 1992).

3.3 Weak form of field equations

Eqs (3.34) and (3.50) describe the incremental equilibrium and evolution of the plastic process in a strong sense. For the finite element formulation a weak form of these rate equations is necessary. The plastic multiplier field is then discretized in addition to the displacements and a mixed finite element formulation ensues.

Firstly we consider a set of all admissible displacement rates, fulfilling eq. (3.35) and (3.42)₂. Eq. (3.34) is multiplied by a virtual displacement rate vector $\delta \dot{\mathbf{u}}$ and an integral over the body volume gives the equation:

$$\int_V \delta \dot{\mathbf{u}}^T [\mathbf{L}^T \dot{\boldsymbol{\sigma}}] dV = 0, \quad (3.51)$$

which must be true for all variations $\delta \dot{\mathbf{u}}$ (the body forces \mathbf{b} have been skipped for convenience). Using integration by parts and eqs (3.35), (3.42)₁ it is possible to write the equation:

$$\int_V \delta \dot{\boldsymbol{\varepsilon}}^T \dot{\boldsymbol{\sigma}} dV - \int_S \delta \dot{\mathbf{u}}^T \dot{\mathbf{t}} dS = 0, \quad (3.52)$$

which is essentially the virtual displacement principle. Substitution of eq. (3.36) in eq. (3.52) subsequently leads to the following weak equilibrium condition for the elastoplastic body:

$$\int_V \delta \dot{\boldsymbol{\varepsilon}}^T \mathbf{D}^e (\dot{\boldsymbol{\varepsilon}} - \dot{\boldsymbol{\lambda}} \mathbf{m}) dV - \int_S \delta \dot{\mathbf{u}}^T \dot{\mathbf{t}} dS = 0. \quad (3.53)$$

Secondly we consider a set of admissible plastic multipliers $\dot{\boldsymbol{\lambda}}$, sufficiently continuous and equal to zero on the elastic-plastic boundary. Multiplying eq. (3.50) by a variation of the plastic multiplier $\delta \dot{\boldsymbol{\lambda}}$ and integrating over the plastic volume of the body V_λ we can write:

$$\int_{V_\lambda} \delta \dot{\boldsymbol{\lambda}} (\mathbf{n}^T \dot{\boldsymbol{\sigma}} - h \dot{\boldsymbol{\lambda}} + g \nabla^2 \dot{\boldsymbol{\lambda}}) dV = 0. \quad (3.54)$$

This identity must hold for any admissible $\delta\lambda$. After substitution of the relationship between the stress and the elastic strain rate (3.36) we obtain:

$$\int_{V_\lambda} \delta\lambda [\mathbf{n}^T \mathbf{D}^e \dot{\boldsymbol{\varepsilon}} - (h + \mathbf{n}^T \mathbf{D}^e \mathbf{m}) \dot{\lambda}] dV + \int_{V_\lambda} \delta\lambda (g \nabla^2 \dot{\lambda}) dV = 0 \quad (3.55)$$

and after integration of the last term in eq. (3.55) by parts we obtain:

$$\int_{V_\lambda} \delta\lambda [\mathbf{n}^T \mathbf{D}^e \dot{\boldsymbol{\varepsilon}} - (h + \mathbf{n}^T \mathbf{D}^e \mathbf{m}) \dot{\lambda}] dV - \int_{V_\lambda} g (\nabla \delta\lambda)^T (\nabla \dot{\lambda}) dV + \int_{S_\lambda} g \delta\lambda (\nabla \dot{\lambda})^T \mathbf{v}_\lambda dS = 0, \quad (3.56)$$

where \mathbf{v}_λ defines the outward normal to the boundary of the plastic part of the body S_λ . For the boundary integral to vanish one of the conditions

$$\delta\dot{\lambda} = 0 \quad \text{or} \quad (\nabla \dot{\lambda})^T \mathbf{v}_\lambda = 0, \quad (3.57)$$

must be fulfilled on the external part of S_λ , since the first condition is true for the admissible $\delta\dot{\lambda}$ on the elastic-plastic boundary.

With the idea of using the same finite element mesh for both the equilibrium and consistency conditions, integrals in eqs (3.55) and (3.56) can be extended over the whole volume V and surface S , since according to the Kuhn-Tucker conditions (3.41) $\dot{\lambda} = \delta\dot{\lambda} = 0$ in the elastic part of the body. The discretization of the displacement and plastic multiplier fields will be presented for the incremental formulation in the following chapter.

As has been shown by de Borst and Mühlhaus (1992), even for the case of associated plasticity (i.e. when $G = \phi$ and $\mathbf{m} = \mathbf{n}$), eqs (3.53) and (3.55) lead to a nonsymmetric matrix problem due to the presence of the Laplacian term. C^1 -continuous interpolation functions for $\dot{\lambda}$ are then required, which involves the derivatives of the plastic multiplier as nodal degrees of freedom. On the other hand eqs (3.53) and (3.56) lead to a symmetric matrix problem that can also be derived from a variational principle for gradient plasticity (Mühlhaus and Aifantis 1991), see also the next section. In this case standard C^0 -continuous shape functions suffice for both $\dot{\mathbf{u}}$ and $\dot{\lambda}$.

3.3.1 Variational formulation

We limit our discussion to the case of associated plasticity and use a functional similar to that considered by Mühlhaus and Aifantis (1991), with only second order gradients of the equivalent plastic strain retained:

$$\Pi(\dot{\mathbf{u}}, \dot{\lambda}) = \frac{1}{2} \int_V [(\dot{\boldsymbol{\varepsilon}} - \dot{\lambda} \mathbf{n})^T \mathbf{D}^e (\dot{\boldsymbol{\varepsilon}} - \dot{\lambda} \mathbf{n}) + h \dot{\lambda}^2 + g (\nabla \dot{\lambda})^T (\nabla \dot{\lambda})] dV - \int_S \dot{\mathbf{u}}^T \dot{\mathbf{t}} dS. \quad (3.58)$$

The functional is subject to the constraints (3.41). We require the stationarity of Π with respect to arbitrary small changes of $(\dot{\mathbf{u}}, \dot{\lambda})$ and obtain:

$$\delta \Pi = \int_V [(\delta \dot{\boldsymbol{\varepsilon}} - \delta \dot{\lambda} \mathbf{n})^T \mathbf{D}^e (\dot{\boldsymbol{\varepsilon}} - \dot{\lambda} \mathbf{n}) + h \dot{\lambda} \delta \dot{\lambda} + g (\nabla \dot{\lambda})^T (\nabla \delta \dot{\lambda})] dV - \int_S \delta \dot{\mathbf{u}}^T \dot{\mathbf{t}} dS = 0. \quad (3.59)$$

Applying Green's formula and noting that $\delta \dot{\lambda} = 0$ in $V - V_\lambda$, eq. (3.59) can be transformed into:

$$\int_V -\delta \dot{\mathbf{u}}^T [\mathbf{L}^T \mathbf{D}^e (\dot{\boldsymbol{\varepsilon}} - \dot{\boldsymbol{\lambda}} \mathbf{n})] dV + \int_S \delta \dot{\mathbf{u}}^T (\dot{\boldsymbol{\Sigma}} \mathbf{v}_s - \dot{\mathbf{t}}) dS +$$

$$+ \int_{V_\lambda} -\delta \dot{\lambda} [\mathbf{n}^T \mathbf{D}^e \dot{\boldsymbol{\varepsilon}} - (h + \mathbf{n}^T \mathbf{D}^e \mathbf{n}) \dot{\lambda} + g \nabla^2 \dot{\lambda}] dV + \int_{S_\lambda} g \delta \dot{\lambda} (\nabla \dot{\lambda})^T \mathbf{v}_\lambda dS = 0, \quad (3.60)$$

where as before $\boldsymbol{\Sigma}$ is the stress tensor in a matrix form, S and S_λ are the boundaries of the body and its plastified part, \mathbf{v}_s and \mathbf{v}_λ denote the outward normals to the surfaces S and S_λ , respectively. Eq. (3.42) must hold for arbitrary $\delta \dot{\mathbf{u}}$ and $\delta \dot{\lambda}$, so from the first line we obtain the first Euler equation:

$$\mathbf{L}^T \mathbf{D}^e (\dot{\boldsymbol{\varepsilon}} - \dot{\boldsymbol{\lambda}} \mathbf{n}) = 0 \quad (3.61)$$

and the standard boundary conditions (3.42), while the second line of eq. (3.42) gives the second Euler equation:

$$\mathbf{n}^T \mathbf{D}^e \dot{\boldsymbol{\varepsilon}} - (h + \mathbf{n}^T \mathbf{D}^e \mathbf{n}) \dot{\lambda} + g \nabla^2 \dot{\lambda} = 0 \quad (3.62)$$

and the non-standard boundary conditions (3.57). The Euler equations ensure in a pointwise manner the equilibrium and the plastic flow consistency, respectively.

4. Algorithm and finite elements

4.1 Incremental formulation

An incremental formulation of the above boundary value problem gives rise to residual terms, which make the stress update necessary. The movement of the elastic-plastic boundary within a loading step must also be considered.

The aim is to derive an incremental-iterative algorithm enforcing the equilibrium and the yield condition at the end of every loading step (cf. de Borst and Mühlhaus 1992). We require a weak satisfaction of the equilibrium condition

$$\int_V \delta \mathbf{u}^T (\mathbf{L}^T \boldsymbol{\sigma}_{j+1}) dV = 0 \quad (4.1)$$

and the yield condition

$$\int_{V_A} \delta \lambda F(\boldsymbol{\sigma}_{j+1}, \kappa_{j+1}, \nabla^2 \kappa_{j+1}) dV = 0 \quad (4.2)$$

at the end of iteration $j+1$ of the current loading step. Unlike in the usual algorithms for plasticity, the latter condition is satisfied in a distributed sense. Furthermore, it is only fulfilled when convergence is reached and not necessarily during the iterative process.

Eq. (4.1) can be modified using integration by parts and the standard boundary conditions (3.42)₁, and decomposing $\boldsymbol{\sigma}_{j+1}$ as $\boldsymbol{\sigma}_j + d\boldsymbol{\sigma}$, where 'd' indicates an increment, i.e. the difference between the values of a variable at the end of iteration $j+1$ and iteration j :

$$\int_V \delta \boldsymbol{\varepsilon}^T d\boldsymbol{\sigma} dV = \int_S \delta \mathbf{u}^T \mathbf{t}_{j+1} dS - \int_V \delta \boldsymbol{\varepsilon}^T \boldsymbol{\sigma}_j dV . \quad (4.3)$$

Using the incremental form of the relationship between the stress and the elastic strain vector

$$d\boldsymbol{\sigma} = \mathbf{D}^e (d\boldsymbol{\varepsilon} - d\lambda \mathbf{m}) , \quad (4.4)$$

we obtain the following integral equation:

$$\int_V \delta \boldsymbol{\varepsilon}^T \mathbf{D}^e (d\boldsymbol{\varepsilon} - d\lambda \mathbf{m}) dV = \int_S \delta \mathbf{u}^T \mathbf{t}_{j+1} dS - \int_V \delta \boldsymbol{\varepsilon}^T \boldsymbol{\sigma}_j dV . \quad (4.5)$$

We observe that this equation does not depend explicitly on the Laplacian of the plastic multiplier and has a form similar to the incremental equilibrium equations used for classical plasticity.

The yield function F in eq. (4.2) is developed in a Taylor series around $(\boldsymbol{\sigma}_j, \kappa_j, \nabla^2 \kappa_j)$ and truncated after the linear terms:

$$F(\boldsymbol{\sigma}_{j+1}, \kappa_{j+1}, \nabla^2 \kappa_{j+1}) = F(\boldsymbol{\sigma}_j, \kappa_j, \nabla^2 \kappa_j) + \left(\frac{\partial F}{\partial \boldsymbol{\sigma}} \right)^T \Big|_j d\boldsymbol{\sigma} + \frac{\partial F}{\partial \kappa} \Big|_j d\kappa + \frac{\partial F}{\partial \nabla^2 \kappa} \Big|_j \nabla^2 (d\kappa) , \quad (4.6)$$

where $d\kappa = \kappa_{j+1} - \kappa_j$. With the definitions (3.47-3.49) we obtain the following form of eq. (4.6):

$$F(\sigma_{j+1}, \kappa_{j+1}, \nabla^2 \kappa_{j+1}) = F(\sigma_j, \kappa_j, \nabla^2 \kappa_j) + \mathbf{n}^T d\boldsymbol{\sigma} - h d\lambda + g \nabla^2(d\lambda), \quad (4.7)$$

which, after substitution into eq. (4.2), gives the following integral equation:

$$\int_{V_\lambda} \delta \lambda [\mathbf{n}^T \mathbf{D}^e d\boldsymbol{\varepsilon} - (h + \mathbf{n}^T \mathbf{D}^e \mathbf{m}) d\lambda + g \nabla^2(d\lambda)] dV = - \int_{V_\lambda} \delta \lambda F(\sigma_j, \kappa_j, \nabla^2 \kappa_j) dV. \quad (4.8)$$

It is noted that the values of \mathbf{n} , \mathbf{m} , h and g on the left-hand side of eq. (4.8) are determined at the end of iteration j , i.e. for the state defined by $(\sigma_j, \kappa_j, \nabla^2 \kappa_j)$. Using integration by parts for the last term on the left-hand side of eq. (4.8) we obtain

$$\begin{aligned} & \int_{V_\lambda} \delta \lambda [\mathbf{n}^T \mathbf{D}^e d\boldsymbol{\varepsilon} - (h + \mathbf{n}^T \mathbf{D}^e \mathbf{m}) d\lambda] dV - \int_{V_\lambda} g (\nabla d\lambda)^T (\nabla d\lambda) dV = \\ & = - \int_{V_\lambda} \delta \lambda F(\sigma_j, \kappa_j, \nabla^2 \kappa_j) dV, \end{aligned} \quad (4.9)$$

provided the non-standard boundary conditions

$$\delta d\lambda = 0 \quad \text{or} \quad (\nabla d\lambda)^T \mathbf{v}_\lambda = 0 \quad (4.10)$$

are fulfilled on the whole boundary S_λ of the plastic part of the body. The first condition is delicate for finite increments, since the elastic-plastic boundary moves when the plastic zone in the body evolves. During this process the boundary condition $\delta \lambda = 0$ on the momentary elastic-plastic boundary may be not true and $(4.10)_2$ must hold.

If the same mesh is to be used for both the equilibrium and yield condition, i.e. if integrals over the whole volume V are to appear in eqs (4.8) and (4.9), either the admissible $\delta \lambda$ must vanish in the elastic part of the body (which would set constraints on the shape functions to be used) or we must enforce there $F = 0$, $\mathbf{n} = \mathbf{m} = \mathbf{0}$ and $d\lambda = 0$.

In the residual terms on the right-hand side of eqs (4.5) and (4.8) or (4.9) there appears the total value of the stress σ_j . It is determined using the standard elastic predictor-plastic corrector algorithm (backward Euler type) at each integration point in a plastic state:

$$\sigma_j = \sigma_0 + \mathbf{D}^e \Delta \boldsymbol{\varepsilon}_j - \Delta \lambda_j \mathbf{D}^e \mathbf{m}_j, \quad (4.11)$$

where σ_0 is the stress state at the end of the previous (converged) load increment and ' Δ ' denotes a 'total' increment (from iteration 0 to iteration j). The values of κ_j and $\nabla^2 \kappa_j$ are also updated using 'total' increments. Since the vector \mathbf{m}_j is known only after the mapping in eq. (4.11), it is approximated by the gradient \mathbf{m}_t calculated for the 'trial' stress:

$$\sigma_t = \sigma_0 + \mathbf{D}^e \Delta \boldsymbol{\varepsilon}_j. \quad (4.12)$$

To decide whether an elastic point enters the plastic regime or whether a plastic point begins elastic unloading the trial value of the yield function F_t is calculated at each integration point:

$$F_t = \phi(\sigma_t) - \bar{\sigma}_g(\kappa_j, \nabla^2 \kappa_j), \quad (4.13)$$

where the gradient-dependent yield strength is determined as follows:

$$\bar{\sigma}_g = \bar{\sigma}(\kappa_j) - g(\kappa_j) \nabla^2 \lambda_j . \quad (4.14)$$

An integration point is assumed to be in the plastic state when $F_i > 0$ and in the elastic state when $F_i < 0$. Notice that in the elastic elements $\lambda = 0$, so for spreading of the plastic zone it is important that the numerical solution allows $\nabla^2 \lambda > 0$ at the elastic-plastic boundary. The nonlocal yield strength $\bar{\sigma}_g$ is then reduced as a result of the plastic process in the neighbourhood.

The dependence of the yield function on the Laplacian of the plastic strain measure is thus essential for the plastification condition and for the determination of the non-standard residual forces on the right-hand side of eqs (4.8)/(4.9). The boundary conditions (4.10)₂ call for the existence of derivatives of λ as nodal degrees of freedom. Therefore C^1 -continuous interpolation functions are necessary for λ whether eq. (4.8) or eq. (4.9) is discretized. This issue has raised some doubts in the past (cf. de Borst and Mühlhaus 1992), since the formulation of the variational principle for gradient plasticity (Mühlhaus and Aifantis 1991) suggested that the use of a standard C^0 -interpolation for the plastic multiplier would be sufficient.

However, it has become clear that it is not enough to symmetrize the tangent stiffness operator to reduce the continuity requirements, but the residual terms must also be reformulated. For example the yield condition (3.40) written as

$$F = f(\boldsymbol{\sigma}, \kappa) + g \nabla^2 \lambda = 0 \quad (4.15)$$

must be recast in an integral form at an element level. To this end F is multiplied by λ and integrated over the element volume. The Laplacian is then eliminated upon integration by parts:

$$\bar{F} = \int_{V_e} \lambda f(\boldsymbol{\sigma}, \kappa) dV - \int_{V_e} g(\nabla \lambda)^T (\nabla \lambda) dV + \int_{S_e} g \lambda \nabla \lambda \mathbf{v}_e dS = 0 . \quad (4.16)$$

Unfortunately, this integral condition cannot perform well in elastic elements, since, numerically, λ is zero there and the second integral gives a negative contribution preventing the yield condition from being violated. It seems that in the standard C^0 -approach, without the Laplacian-dependent yield condition, a method of distinguishing the elastic and plastic state is lost and consequently the plastic zone does not spread from the imperfect elements.

If we reformulate the right-hand side of eq. (4.9) using the form (4.15) of the yield function as follows

$$\begin{aligned} & - \int_{V_\lambda} \delta \lambda [f(\boldsymbol{\sigma}_j, \kappa_j) + g \nabla^2 \lambda_j] dV = \\ & = - \int_{V_\lambda} \delta \lambda f(\boldsymbol{\sigma}_j, \kappa_j) dV + \int_{V_\lambda} g(\nabla \delta \lambda)^T (\nabla \lambda_j) dV - \int_{S_\lambda} g \delta \lambda (\nabla \lambda_j)^T \mathbf{v}_\lambda dS , \end{aligned} \quad (4.17)$$

numerical experiments give incorrect values of the two last terms, since they are equivalent to the Laplacian term which is not well defined if C^1 -continuity is not fulfilled.

In special situations, i.e. when the plastic flow directions are the same in the trial and

final state, softening is linear and no stress redistributions take place, an immediate mapping to the yield surface is observed and the residual term on the right-hand side of eqs (4.8)/(4.9) is non-zero only in the step, in which the plastic regime is entered. This suggests that the consistency condition could be used instead of the yield condition to derive the algorithm. However, in the absence of the residuals, the stresses in an arbitrary case are not correctly returned to the yield surface.

4.1.1 C^1 -continuous element formulation

This formulation has originally been suggested by de Borst and Mühlhaus (1991). In the field equations (4.5) and (4.8)/(4.9) there appear at most first order derivatives of the displacements and second order derivatives of the plastic multiplier. Therefore the discretization procedure for the displacement field \mathbf{u} requires C^0 -continuous interpolation functions \mathbf{N} :

$$\mathbf{u} = \mathbf{N} \mathbf{a} , \quad (4.18)$$

where \mathbf{a} is a nodal displacement vector, and the discretization of the plastic multiplier λ requires C^1 -continuous shape functions \mathbf{h}

$$\lambda = \mathbf{h}^T \mathbf{\Lambda} , \quad (4.19)$$

where $\mathbf{\Lambda}$ denotes a vector of nodal degrees of freedom for the plastic multiplier field.

According to the linear kinematic relation (3.35) the discretization of strains has the form:

$$\boldsymbol{\varepsilon} = \mathbf{B} \mathbf{a} , \quad (4.20)$$

where $\mathbf{B} = \mathbf{L}\mathbf{N}$. Substitution of the above identities in eq. (4.5) gives the discretized equilibrium condition:

$$\delta \mathbf{a}^T \int_V [\mathbf{B}^T \mathbf{D}^e \mathbf{B} \mathbf{d} \mathbf{a} - \mathbf{B}^T \mathbf{D}^e \mathbf{m} \mathbf{h}^T \mathbf{d} \mathbf{\Lambda}] dV = \delta \mathbf{a}^T \int_S \mathbf{N}^T \mathbf{t}_{j+1} dS - \delta \mathbf{a}^T \int_V \mathbf{B}^T \boldsymbol{\sigma}_j dV . \quad (4.21)$$

Introducing a matrix \mathbf{q} which contains the derivatives of the shape functions in \mathbf{h} we obtain the discretization of the gradient of the plastic multiplier:

$$\nabla \lambda = \mathbf{q}^T \mathbf{\Lambda} , \quad \mathbf{q}^T = \nabla \mathbf{h}^T . \quad (4.22)$$

Introducing a vector \mathbf{p} which contains the Laplacians of the shape functions in \mathbf{h} we find the discretization formula for the Laplacian of the plastic multiplier:

$$\nabla^2 \lambda = \mathbf{p}^T \mathbf{\Lambda} . \quad (4.23)$$

Substitution of eqs (4.19), (4.20) and (4.23) in eq. (4.8) gives the discretized yield condition in the following form:

$$\begin{aligned} & \delta \mathbf{\Lambda}^T \int_V [-\mathbf{h} \mathbf{n}^T \mathbf{D}^e \mathbf{B} \mathbf{d} \mathbf{a} + (\mathbf{h} + \mathbf{n}^T \mathbf{D}^e \mathbf{m}) \mathbf{h} \mathbf{h}^T \mathbf{d} \mathbf{\Lambda} - \mathbf{g} \mathbf{h} \mathbf{p}^T \mathbf{d} \mathbf{\Lambda}] dV = \\ & = \delta \mathbf{\Lambda}^T \int_V F(\boldsymbol{\sigma}_j, \kappa_j, \nabla^2 \kappa_j) \mathbf{h} dV . \end{aligned} \quad (4.24)$$

Eqs (4.21) and (4.24) must hold for any admissible variation of $\delta \mathbf{a}$ and $\delta \Lambda$, so we obtain the following set of algebraic equations (de Borst and Mühlig 1992):

$$\begin{bmatrix} \mathbf{K}_{aa} & \mathbf{K}_{a\lambda} \\ \mathbf{K}_{\lambda a} & \mathbf{K}_{\lambda\lambda} \end{bmatrix} \begin{bmatrix} d\mathbf{a} \\ d\Lambda \end{bmatrix} = \begin{bmatrix} \mathbf{f}_e + \mathbf{f}_a \\ \mathbf{f}_\lambda \end{bmatrix}, \quad (4.25)$$

with the elastic stiffness matrix:

$$\mathbf{K}_{aa} = \int_V \mathbf{B}^T \mathbf{D}^e \mathbf{B} dV, \quad (4.26)$$

the off-diagonal matrices:

$$\mathbf{K}_{a\lambda} = - \int_V \mathbf{B}^T \mathbf{D}^e \mathbf{m} \mathbf{h}^T dV, \quad \mathbf{K}_{\lambda a} = - \int_V \mathbf{h} \mathbf{n}^T \mathbf{D}^e \mathbf{B} dV, \quad (4.27)$$

the nonsymmetric gradient-dependent matrix:

$$\mathbf{K}_{\lambda\lambda} = \int_V [(\mathbf{h} + \mathbf{n}^T \mathbf{D}^e \mathbf{m}) \mathbf{h} \mathbf{h}^T - g \mathbf{h} \mathbf{p}^T] dV, \quad (4.28)$$

the external force vector and the vector of nodal forces equivalent to internal stresses:

$$\mathbf{f}_e = \int_S \mathbf{N}^T \mathbf{t}_{j+1} dS, \quad \mathbf{f}_a = - \int_V \mathbf{B}^T \boldsymbol{\sigma}_j dV, \quad (4.29)$$

and the vector of residual forces emerging from the inexact fulfilment of the yield condition:

$$\mathbf{f}_\lambda = \int_V F(\boldsymbol{\sigma}_j, \lambda_j, \nabla^2 \lambda_j) \mathbf{h} dV. \quad (4.30)$$

If we make use of eq. (4.9) instead of eq. (4.8), substitution of eqs (4.19), (4.20) and (4.22) gives the second form of the discretized yield condition:

$$\begin{aligned} & \delta \Lambda^T \int_V [-\mathbf{h} \mathbf{n}^T \mathbf{D}^e \mathbf{B} d\mathbf{a} + (\mathbf{h} + \mathbf{n}^T \mathbf{D}^e \mathbf{m}) \mathbf{h} \mathbf{h}^T d\Lambda + g \mathbf{q} \mathbf{q}^T d\Lambda] dV = \\ & = \delta \Lambda^T \int_V F(\boldsymbol{\sigma}_j, \kappa_j, \nabla^2 \kappa_j) \mathbf{h} dV, \end{aligned} \quad (4.31)$$

which leads to a similar matrix problem as in eq. (4.25), but now the nonsymmetry due to the Laplacian term vanishes, i.e. the matrix $\mathbf{K}_{\lambda\lambda}$ is nonsymmetric only for the non-associated flow:

$$\mathbf{K}_{\lambda\lambda} = \int_V [(\mathbf{h} + \mathbf{n}^T \mathbf{D}^e \mathbf{m}) \mathbf{h} \mathbf{h}^T + g \mathbf{q} \mathbf{q}^T] dV \quad (4.32)$$

However, the additional boundary conditions (4.10) have to be enforced in this case.

The set of equations (4.25) governs the element behaviour during the plastic flow. We will now consider the actual problem of a structure which is initially elastic and then due to an inhomogeneous stress distribution exhibits a partial plastification. If all elements are elastic, we have $\mathbf{K}_{\lambda a} = \mathbf{K}_{a\lambda} = \mathbf{0}$ since the gradient vectors \mathbf{n} and \mathbf{m} are set to

zero. Then we obtain from eq. (4.25) the classical set of equations in $d\mathbf{a}$

$$\mathbf{K}_{aa} d\mathbf{a} = \mathbf{f}_e + \mathbf{f}_a \quad (4.33)$$

and the additional set of equations in $d\Lambda$

$$\mathbf{K}_{\lambda\lambda}^e d\Lambda = \mathbf{f}_\lambda . \quad (4.34)$$

For the elastic state we have $F < 0$ and we set the residual forces \mathbf{f}_λ to zero. Eq. (4.34) then yields the desired solution $d\Lambda = 0$ if the global matrix $\bar{\mathbf{K}}^e$ is non-singular after the element assembly and after the introduction of boundary conditions for the Λ degrees of freedom, which is always necessary for the symmetric formulation and may be necessary also for the nonsymmetric one.

If, however, plastic elements appear in the structure, then in elastic elements adjacent to the plastic zone we have $\mathbf{f}_\lambda \neq 0$ and we have non-zero $d\Lambda$ from eq. (4.34). The C^1 -continuous finite elements have the feature, that these nodal values of plastic multiplier $d\Lambda$ yield $d\lambda \approx 0$ and $\nabla^2(d\lambda) > 0$ at the integration points. As a result the yield strength $\bar{\sigma}_g = \bar{\sigma} - g\nabla^2\lambda$ is reduced and new elastic elements can enter the plastic regime.

It is observed that it is not necessary to input the value of hardening modulus h equal to a large number in the formula (4.28) to constrain the value of λ to zero for elastic elements as has been suggested by de Borst and Mühlhaus (1992). In fact, this substitution adversely affects the conditioning of the global tangential operator $\bar{\mathbf{K}}$, which in turn affects the accuracy of the local return mapping in eq. (4.11). For some elements it may cause containment of the plastic flow in the initially imperfect zones and prevent the regularization effect.

In this thesis h is taken equal to Young's modulus E for elastic elements. The gradient term may be neglected in the matrix $\mathbf{K}_{\lambda\lambda}^e$ for elastic elements (its inclusion only slightly influences the results). Using numerical integration the matrix $\mathbf{K}_{\lambda\lambda}^e$ is then determined as:

$$\mathbf{K}_{\lambda\lambda}^e = \sum_{ip=1}^{ip} E \mathbf{h}_{ip} \mathbf{h}_{ip}^T V_{ip} , \quad (4.35)$$

where V_{ip} is a volume contribution of an integration point (a product of the integration weight, cross-section area or thickness and Jacobian of the transformation from unit reference coordinates to Cartesian coordinates). It is useful to examine the rank of submatrices \mathbf{K}_{aa} and $\mathbf{K}_{\lambda\lambda}^e$ in order to determine the number of integration points and extra boundary conditions sufficient to avoid spurious modes for both the displacement and plastic multiplier fields. The elastic stiffness matrix \mathbf{K}_{aa} should have zero eigenvalues associated only with the rigid body motions. The matrix $\mathbf{K}_{\lambda\lambda}^e$ should have at most as many zero eigenvalues as the available boundary conditions for the plastic multiplier field can remove, while it has a number of non-zero eigenvalues equal to the number of integration points (matrix $\mathbf{h}\mathbf{h}^T$ has only one non-zero eigenvalue). As we will see in the following, some elements do not satisfy these requirements.

It should also be taken into account, that a high-order integration scheme and too many additional boundary conditions for λ (even if they comply with the theory) may

lead to an overconstrained plastic flow problem and have a negative influence on the accuracy of finite element predictions. Since the yield condition may be conceived as a differential constraint to the equilibrium condition of a nonlinear solid, we realize that the number of constraints for the plastic multiplier field must be limited, otherwise the solution will be inaccurate or will lock, as happens for instance with some standard elements for the incompressible limit. In other words, we now have a two-field theory similar to the mixed formulation with independent displacement and pressure interpolation and a proper constraint ratio between the displacement and λ degrees of freedom should be preserved.

4.1.2 C^0 -approach with a penalty constraint

In order to be able to use C^0 -continuous interpolation functions for the plastic multiplier field, we introduce new variables φ_x , φ_y and φ_z :

$$\varphi_x = \frac{\partial \lambda}{\partial x}, \quad \varphi_y = \frac{\partial \lambda}{\partial y}, \quad \varphi_z = \frac{\partial \lambda}{\partial z} \quad (4.36)$$

and collect them in a vector $\phi = (\varphi_x, \varphi_y, \varphi_z)$. In this way we can write the gradient of the plastic multiplier as

$$\nabla \lambda = \phi \quad (4.37)$$

and represent the Laplacian of λ as

$$\nabla^2 \lambda = \frac{\partial \varphi_x}{\partial x} + \frac{\partial \varphi_y}{\partial y} + \frac{\partial \varphi_z}{\partial z} = \nabla^T \phi, \quad (4.38)$$

where the scalar product of the operator ∇^T and the vector field ϕ denotes the divergence operator. The result of eq. (4.38) can be substituted in eq. (4.8) or (4.9), but the constraint (4.37) must be added to the formulation.

Since we want to avoid the introduction of a Lagrangian multiplier field in addition to the already defined three fields \mathbf{u} , λ and ϕ , we will make use of the penalty approach. We can include the constraint by means of an additional variational equation:

$$\int_V k(\nabla \lambda - \phi)^T [\nabla(\delta \lambda) - \delta \phi] dV = 0, \quad (4.39)$$

where k is a penalty factor. In calculations we use $k = E^3$, where E is Young's modulus. Using the incremental form of eq. (4.39) together with eqs (4.5) and (4.8) we obtain the set of three integral equations:

$$\int_V \delta \varepsilon^T \mathbf{D}^e (d\varepsilon - d\lambda \mathbf{m}) dV = \int_S \delta \mathbf{u}^T \mathbf{t}_{j+1} dS - \int_V \delta \varepsilon^T \sigma_j dV, \quad (4.40)$$

$$\int_V \delta \lambda [\mathbf{n}^T \mathbf{D}^e d\varepsilon - (h + \mathbf{n}^T \mathbf{D}^e \mathbf{m}) d\lambda + g \nabla^T d\phi] dV = - \int_V \delta \lambda F(\sigma_j, \kappa_j, \nabla^2 \kappa_j) dV, \quad (4.41)$$

where according to eqs (3.45) and (4.38) we calculate $\nabla^2 \kappa = \eta \nabla^T \phi$ and

$$k \int_V \delta \lambda \nabla^T [\nabla(d\lambda) - d\phi] dV - k \int_V \delta \phi^T [\nabla(d\lambda) - d\phi] dV = 0. \quad (4.42)$$

The above equations are discretized using the formulas (4.19), (4.20) and (4.22), but now with C^0 -continuous shape functions in \mathbf{h} , and the following interpolation for the new variables in ϕ :

$$\phi = \mathbf{P} \Phi, \quad (4.43)$$

where Φ contains the nodal values of ϕ_x , ϕ_y and ϕ_z and \mathbf{P} is a matrix of shape functions, similar to \mathbf{N} in eq. (4.18). Upon the discretization of eqs (4.40-4.42) and the usual argument that the resulting equations

$$\delta \mathbf{a}^T \int_V [\mathbf{B}^T \mathbf{D}^e \mathbf{B} \mathbf{d} \mathbf{a} - \mathbf{B}^T \mathbf{D}^e \mathbf{m} \mathbf{h}^T d\Lambda] dV = \delta \mathbf{a}^T \int_S \mathbf{N}^T \mathbf{t}_{j+1} dV - \delta \mathbf{a}^T \int_V \mathbf{B}^T \sigma_j dV, \quad (4.44)$$

$$\begin{aligned} & \delta \Lambda^T \int_V [-\mathbf{h} \mathbf{n}^T \mathbf{D}^e \mathbf{B} \mathbf{d} \mathbf{a} + (h + \mathbf{n}^T \mathbf{D}^e \mathbf{m}) \mathbf{h} \mathbf{h}^T d\Lambda - g \mathbf{h} \nabla^T \mathbf{P} d\Phi] dV = \\ & = \delta \Lambda^T \int_V F(\sigma_j, \kappa_j, \nabla^2 \kappa_j) \mathbf{h} dV \end{aligned} \quad (4.45)$$

and

$$k \delta \Lambda^T \int_V \mathbf{q} (\mathbf{q}^T d\Lambda - \mathbf{P} d\Phi) dV - k \delta \Phi^T \int_V \mathbf{P}^T (\mathbf{q}^T d\Lambda - \mathbf{P} d\Phi) dV = 0 \quad (4.46)$$

must hold for any admissible $\delta \mathbf{a}$, $\delta \Lambda$ and $\delta \Phi$, we obtain the following set of algebraic equations in a matrix form:

$$\left\{ \begin{bmatrix} \mathbf{K}_{aa} & \mathbf{K}_{a\lambda} & \mathbf{0} \\ \mathbf{K}_{\lambda a} & \mathbf{K}_{\lambda\lambda} & \mathbf{K}_{\lambda\phi} \\ \mathbf{0} & \mathbf{0} & \mathbf{0} \end{bmatrix} + k \begin{bmatrix} \mathbf{0} & \mathbf{0} & \mathbf{0} \\ \mathbf{0} & \mathbf{K}_{\lambda\lambda}^c & \mathbf{K}_{\lambda\phi}^c \\ \mathbf{0} & \mathbf{K}_{\lambda\phi}^{cT} & \mathbf{K}_{\phi\phi}^c \end{bmatrix} \right\} \begin{bmatrix} d\mathbf{a} \\ d\Lambda \\ d\Phi \end{bmatrix} = \begin{bmatrix} \mathbf{f}_c + \mathbf{f}_a \\ \mathbf{f}_\lambda \\ \mathbf{0} \end{bmatrix}. \quad (4.47)$$

In eq. (4.47) the submatrices \mathbf{K}_{aa} , $\mathbf{K}_{a\lambda}$ and $\mathbf{K}_{\lambda a}$ are given in eqs (4.26) and (4.27), $\mathbf{K}_{\lambda\lambda}$ and $\mathbf{K}_{\lambda\phi}$ are defined as

$$\mathbf{K}_{\lambda\lambda} = \int_V (h + \mathbf{n}^T \mathbf{D}^e \mathbf{m}) \mathbf{h} \mathbf{h}^T dV, \quad \mathbf{K}_{\lambda\phi} = - \int_V [g \mathbf{h} \nabla^T \mathbf{P}] dV, \quad (4.48)$$

and the submatrices with the superscript c in the additional (symmetric) matrix introducing the constraint (4.37) are defined as

$$\mathbf{K}_{\lambda\lambda}^c = \int_V \mathbf{q} \mathbf{q}^T dV, \quad \mathbf{K}_{\phi\phi}^c = \int_V \mathbf{P}^T \mathbf{P} dV, \quad \mathbf{K}_{\lambda\phi}^c = \int_V -\mathbf{q} \mathbf{P} dV. \quad (4.49)$$

In this formulation all the interpolation functions in \mathbf{N} , \mathbf{h} and \mathbf{P} are C^0 -continuous.

If we substitute the new variables from eqs (4.37) and (4.38) into eq. (4.9), which leads to the symmetric formulation, instead of using eq. (4.8), from which the above nonsymmetric form follows, we obtain the weak form of the yield condition as follows:

$$\int_V \delta \lambda [\mathbf{n}^T \mathbf{D}^e d\boldsymbol{\varepsilon} - (h + \mathbf{n}^T \mathbf{D}^e \mathbf{m}) d\lambda] dV - \int_V g \delta \phi d\phi dV = - \int_V \delta \lambda F(\sigma_j, \kappa_j, \nabla^2 \kappa_j) dV, \quad (4.50)$$

in which the derivatives of ϕ appear only on the right-hand side in $\nabla^2 \kappa_j$. Substitution of the discretization formulas (4.19), (4.20) and (4.43) gives the second, now symmetric,

form of the discretized yield condition:

$$\begin{aligned} & \delta \Lambda^T \int_V [-\mathbf{h}\mathbf{n}^T \mathbf{D}^e \mathbf{B} \mathbf{d}\mathbf{a} + (h + \mathbf{n}^T \mathbf{D}^e \mathbf{m}) \mathbf{h} \mathbf{h}^T \mathbf{d}\Lambda] dV + \int_V g \delta \Phi^T \mathbf{P}^T \mathbf{P} d\Phi dV = \\ & = \delta \Lambda^T \int_V F(\sigma_j, \kappa_j, \nabla^2 \kappa_j) \mathbf{h} dV \end{aligned} \quad (4.51)$$

and in result the symmetric tangent operator:

$$\left\{ \begin{bmatrix} \mathbf{K}_{aa} & \mathbf{K}_{a\lambda} & \mathbf{0} \\ \mathbf{K}_{\lambda a} & \mathbf{K}_{\lambda\lambda} & \mathbf{0} \\ \mathbf{0} & \mathbf{0} & \mathbf{K}_{\phi\phi} \end{bmatrix} + k \begin{bmatrix} \mathbf{0} & \mathbf{0} & \mathbf{0} \\ \mathbf{0} & \mathbf{K}_{\lambda\lambda}^c & \mathbf{K}_{\lambda\phi}^c \\ \mathbf{0} & \mathbf{K}_{\lambda\phi}^{cT} & \mathbf{K}_{\phi\phi}^c \end{bmatrix} \right\} \begin{bmatrix} \mathbf{d}\mathbf{a} \\ \mathbf{d}\Lambda \\ \mathbf{d}\Phi \end{bmatrix} = \begin{bmatrix} \mathbf{f}_e + \mathbf{f}_a \\ \mathbf{f}_\lambda \\ \mathbf{0} \end{bmatrix}, \quad (4.52)$$

where

$$\mathbf{K}_{\phi\phi} = \int_V g \mathbf{P}^T \mathbf{P} dV \quad (4.53)$$

and all the other submatrices have been defined previously. With the set (4.52) the additional boundary conditions (4.10), now written in the form:

$$\delta d\lambda = 0 \quad \text{or} \quad \mathbf{d}\phi^T \mathbf{v}_\lambda = 0 \quad (4.54)$$

must be fulfilled on the boundary S_λ of the plastic part of the body.

It is important that for the penalty method of introducing the constraint (4.37) to be successful the penalty submatrix \mathbf{K}^c must be singular (otherwise non-zero Φ values are not admitted). To achieve this goal, reduced numerical integration should be used (cf. for instance Zienkiewicz and Nakazawa 1982). Since the penalty constraint assures the satisfaction of eq. (4.37) only in the sampling points, the best results are expected while the uniformly reduced integration is employed for all the matrices. If eq. (4.37) is not true at a Gauss point, the return mapping in eq. (4.11) yields a stress point inside or outside (and not on) the yield surface and convergence is violated.

As explained in the previous section, the sets of equations (4.47) and (4.52) are also required to hold in the elastic subdomain. We should have a sufficient rank of the elastic stiffness matrix \mathbf{K}_{aa} to prevent the presence of spurious deformation modes. Simultaneously we should have a sufficient rank of the matrix $\mathbf{K}_{\lambda\lambda}^c$ from eq. (4.35) to prevent the presence of the spurious non-zero modes of both λ and ϕ in the elastic elements. This suggests the use of a full integration scheme, but in view of the argument that the penalty submatrix \mathbf{K}^c must be singular, we must then resort to extra boundary conditions. It also turns out advantageous to include the gradient submatrix $\mathbf{K}_{\lambda\phi}$ (or $\mathbf{K}_{\phi\phi}$) in the tangent operator for the elastic elements, since it perturbs the singularity of the tangent operator in eqs (4.47) and (4.52), making the emergence of the spurious modes less easy.

It is noted that for a two-dimensional case (cf. Pamin and de Borst 1994) the element structure in the above approach shows similarities to the Reissner-Mindlin plate bending elements and that the penalty method has also been used within the context of plate bending to introduce the Kirchhoff constraints in the formulation (cf. Ortiz and

Morris 1988).

4.2 Algorithmic problems

4.2.1 Consistent linearization

In the classical elasto-plastic continuum model we determine the new stress update as an integral along a given path from the initial (equilibrium) state defined by $(\boldsymbol{\varepsilon}_0, \boldsymbol{\sigma}_0)$ to the final state:

$$\boldsymbol{\sigma} = \boldsymbol{\sigma}_0 + \int_{\boldsymbol{\varepsilon}_0}^{\boldsymbol{\varepsilon}} \mathbf{D}^{\text{ep}}(\boldsymbol{\varepsilon}) \, d\boldsymbol{\varepsilon} , \quad (4.55)$$

where the continuous tangent operator is defined as

$$\mathbf{D}^{\text{ep}}(\boldsymbol{\varepsilon}) = \left. \frac{\partial \boldsymbol{\sigma}}{\partial \boldsymbol{\varepsilon}} \right|_{\boldsymbol{\varepsilon}} . \quad (4.56)$$

However, in the algorithm the stress is updated in iteration j according to:

$$\boldsymbol{\sigma}_j = \boldsymbol{\sigma}_0 + \mathbf{S}(\boldsymbol{\varepsilon}_0, \Delta \boldsymbol{\varepsilon}_j) , \quad (4.57)$$

where \mathbf{S} is a nonlinear mapping operator, which depends on the numerical method of plastic strain integration within the increment (e.g. generalized midpoint rule), and Δ denotes a ‘total’ increment, which is a sum of ‘delta’ increments in the iterations:

$$\Delta \boldsymbol{\varepsilon}_j = \sum_{i=1}^j d\boldsymbol{\varepsilon}_i . \quad (4.58)$$

The consistent (algorithmic) tangent operator is then defined as (cf. for instance Simo and Taylor 1985):

$$\mathbf{D}^{\text{cons}}(\boldsymbol{\varepsilon}_0, \Delta \boldsymbol{\varepsilon}_j) = \left. \frac{\partial \boldsymbol{\sigma}_j}{\partial \Delta \boldsymbol{\varepsilon}} \right|_{\boldsymbol{\varepsilon}_0, \Delta \boldsymbol{\varepsilon}_j} = \left. \frac{\partial \mathbf{S}}{\partial \Delta \boldsymbol{\varepsilon}} \right|_{\boldsymbol{\varepsilon}_0, \Delta \boldsymbol{\varepsilon}_j} \quad (4.59)$$

and is in general nonsymmetric. For finite, especially large, steps the second operator \mathbf{D}^{cons} differs significantly from the continuous operator \mathbf{D}^{ep} . To achieve a quadratic convergence rate of Newton’s algorithm, used for the solution of the set of incremental equations, the consistent linearization as above must be performed. In other words, the way in which the element tangent stiffness matrix is constructed must be consistent with the algorithmic relationship between the stress increment and the strain increment.

The elastic predictor - plastic corrector formula from eq. (4.11):

$$\boldsymbol{\sigma}_j = \boldsymbol{\sigma}_0 + \mathbf{D}^e \Delta \boldsymbol{\varepsilon}_j - \Delta \lambda_j \mathbf{D}^e \mathbf{m}_j , \quad (4.60)$$

used in the gradient plasticity algorithm to calculate $\boldsymbol{\sigma}_j$ at an integration point, is essentially an Euler backward algorithm (cf. for instance Crisfield 1991) and falls within the format (4.57). Therefore, the algorithmic tangent operator can be derived as in (4.59). To this end we calculate the ‘time’ derivative of eq. (4.60):

$$d\boldsymbol{\sigma} = \mathbf{D}^e d\boldsymbol{\varepsilon} - d\lambda \mathbf{D}^e \mathbf{m} - \Delta \lambda \mathbf{D}^e \frac{\partial \mathbf{m}}{\partial \boldsymbol{\sigma}} d\boldsymbol{\sigma} , \quad (4.61)$$

where the subscript j has been skipped for convenience and 'd' is used to denote the 'time' derivative at the state j . We can reformulate eq. (4.61):

$$\left[(\mathbf{D}^e)^{-1} + \Delta\lambda \frac{\partial \mathbf{m}}{\partial \boldsymbol{\sigma}} \right] d\boldsymbol{\sigma} = d\boldsymbol{\varepsilon} - d\lambda \mathbf{m} \quad (4.62)$$

and obtain an algorithmic relation between the stress increment and the elastic strain increment in the form:

$$d\boldsymbol{\sigma} = \mathbf{H} (d\boldsymbol{\varepsilon} - d\lambda \mathbf{m}), \quad (4.63)$$

where \mathbf{H} is the algorithmic stiffness operator:

$$\mathbf{H} = \left[(\mathbf{D}^e)^{-1} + \Delta\lambda \frac{\partial^2 G}{\partial \boldsymbol{\sigma}^2} \right]^{-1}, \quad (4.64)$$

in which the definition (3.39)₂ has been substituted for \mathbf{m} . In the present gradient plasticity algorithm the elastic stiffness matrix \mathbf{D}^e must thus be replaced by the algorithmic operator \mathbf{H} in the equilibrium equation (4.5) and in the yield (plastic consistency) condition (4.8)/(4.9).

It is mentioned that for classical plasticity we would make use of the consistency condition $dF=0$ written at the state j , which for a general definition of the hardening parameter $\kappa = \kappa(\boldsymbol{\varepsilon}^p, \boldsymbol{\sigma})$ looks as follows:

$$dF = \mathbf{n}^T d\boldsymbol{\sigma} + \frac{\partial F}{\partial \kappa} d\kappa = \mathbf{n}^T d\boldsymbol{\sigma} + \frac{\partial F}{\partial \kappa} \left(\frac{\partial \kappa}{\partial \boldsymbol{\varepsilon}^p} \right)^T d\boldsymbol{\varepsilon}^p + \frac{\partial F}{\partial \kappa} \left(\frac{\partial \kappa}{\partial \boldsymbol{\sigma}} \right)^T d\boldsymbol{\sigma}. \quad (4.65)$$

Upon substitution of $d\boldsymbol{\sigma}$ from eq. (4.61) and $d\boldsymbol{\varepsilon}^p$ from the strain rate decomposition:

$$d\boldsymbol{\varepsilon} = d\boldsymbol{\varepsilon}^e + d\boldsymbol{\varepsilon}^p = (\mathbf{D}^e)^{-1} d\boldsymbol{\sigma} + d\lambda \mathbf{m} + \Delta\lambda \frac{\partial \mathbf{m}}{\partial \boldsymbol{\sigma}} d\boldsymbol{\sigma}, \quad (4.66)$$

we can determine the derivative $d\lambda$ and proceed as in Section 2.1.2 to obtain the algorithmic relation between $d\boldsymbol{\sigma}$ and $d\boldsymbol{\varepsilon}$. This relation defines the (nonsymmetric) consistent tangent operator (cf. for instance Schellekens 1992, Lourenço et al 1994), which is used further to calculate the element tangent stiffness matrix. It is noticed that only for the case $\dot{\kappa} = \eta \dot{\lambda}$ ($\eta = \text{constant}$) the algorithmic tangent operator \mathbf{D}^{cons} is obtained by a substitution of the algorithmic stiffness \mathbf{H} for the elastic stiffness \mathbf{D}^e in the continuum operator \mathbf{D}^{ep} from eq. (2.43).

4.2.2 Comparison with a standard plasticity algorithm

In algorithms for standard plasticity the constitutive relations are satisfied locally and we solve the set of equilibrium equations:

$$\hat{\mathbf{K}}_{aa} d\mathbf{a} = \mathbf{f}_c + \mathbf{f}_a, \quad (4.67)$$

where

$$\hat{\mathbf{K}}_{aa} = \int_V \mathbf{B}^T \left(\mathbf{H} - \frac{\mathbf{H} \mathbf{m} \mathbf{n}^T \mathbf{H}}{h + \mathbf{n}^T \mathbf{H} \mathbf{m}} \right) \mathbf{B} dV \quad (4.68)$$

Box 1. An algorithm for standard plasticity (iteration j).

1. Compute $\hat{\mathbf{K}}_{aa}$, \mathbf{f}_e and \mathbf{f}_a according to eqs (4.67), (4.29).

2. Solve eq. (4.67) for $d\mathbf{a}$ and update $\Delta\mathbf{a}_j = \Delta\mathbf{a}_{j-1} + d\mathbf{a}$.

3. For each integration point compute:

$$\Delta\boldsymbol{\varepsilon}_j = \mathbf{B}\Delta\mathbf{a}_j,$$

$$\boldsymbol{\sigma}_t = \boldsymbol{\sigma}_0 + \mathbf{D}^e \Delta\boldsymbol{\varepsilon}_j \text{ (trial stress).}$$

$$\text{If } F(\boldsymbol{\sigma}_t, \kappa_0) \geq 0,$$

$$\text{then plastic state: } i = 0, \Delta\lambda_0 = 0, \boldsymbol{\sigma}_0 = \boldsymbol{\sigma}_t,$$

$$\text{do } \left\{ \begin{array}{l} \Delta\lambda_{i+1} = \Delta\lambda_i + \frac{F(\boldsymbol{\sigma}_i, \kappa_i)}{h_i + \mathbf{n}_i^T \mathbf{D}^e \mathbf{m}_i}, \\ \boldsymbol{\sigma}_{i+1} = \boldsymbol{\sigma}_i - \Delta\lambda_{i+1} \mathbf{D}^e \mathbf{m}_i, \\ \kappa_{i+1} = \kappa_0 + \eta \Delta\lambda_{i+1}, \\ i = i + 1, \end{array} \right.$$

$$\} \text{ while } F(\boldsymbol{\sigma}_i, \kappa_i) \geq \varepsilon,$$

$$\Delta\lambda_j = \Delta\lambda_i, \boldsymbol{\sigma}_j = \boldsymbol{\sigma}_i,$$

$$\text{else elastic state: } \boldsymbol{\sigma}_j = \boldsymbol{\sigma}_t.$$

4. Check global convergence criterion. If not converged, go to 1.

is the consistent tangent operator, in which the algorithmic matrix \mathbf{H} is used instead of the elastic stiffness matrix \mathbf{D}^e . To determine the increment of plastic strains and the new stress state from the incremental displacements, the return mapping algorithms can be applied (cf. Ortiz and Simo 1986). One of the possibilities is the implicit Euler backward scheme (cf. de Borst and Feenstra 1990), which involves the calculation of $\Delta\lambda$ from a nonlinear algebraic equation (yield condition). Another one (see Box 1) is an explicit algorithm resulting from a Taylor expansion of the yield function F around the current values of stress $\boldsymbol{\sigma}_i$ and the hardening parameter κ_i (cf. the *tangent-cutting-plane* algorithm, Ortiz and Simo 1986). In the first iteration linearization around $\boldsymbol{\sigma}_i$ and κ_0 is performed. For some yield functions (e.g. Huber-Mises in plane strain conditions) and linear hardening it can be shown that the formula for $\Delta\lambda$ in Box 1 assures a one-step return to the yield surface (de Borst 1991₂). Otherwise internal iterations are performed in step 3 of the algorithm to bring the stress point to the yield surface.

The solution procedure ensuing from Chapter 4.1 for the case of C^1 -continuous gradient plasticity elements is presented in Box 2. The algorithm for C^0 -elements is similar. For integration points in the elastic state an artificial hardening modulus $h = E$ is

Box 2. An algorithm for gradient plasticity (iteration j , C^1 -elements).

1. Compute \mathbf{K}_{aa} , $\mathbf{K}_{a\lambda}$, $\mathbf{K}_{\lambda a}$, $\mathbf{K}_{\lambda\lambda}$, \mathbf{f}_e , \mathbf{f}_a and \mathbf{f}_λ according to eqs (4.26)-(4.28), (4.29), and (4.30).

2. Solve for $d\mathbf{a}$ and $d\Lambda$ according to eq. (4.25) and update $\Delta\mathbf{a}_j = \Delta\mathbf{a}_{j-1} + d\mathbf{a}$, $\Delta\Lambda_j = \Delta\Lambda_{j-1} + d\Lambda$.

3. For each integration point compute:

$$\Delta\boldsymbol{\varepsilon}_j = \mathbf{B}\Delta\mathbf{a}_j,$$

$$\Delta\lambda_j = \mathbf{h}^T\Delta\Lambda_j,$$

$$\nabla^2(\Delta\lambda_j) = \mathbf{p}^T\Delta\Lambda_j,$$

$$\kappa_j = \kappa_0 + \eta\Delta\lambda_j,$$

$$\nabla^2\kappa_j = \nabla^2\kappa_0 + \eta\nabla^2(\Delta\lambda_j),$$

$$\boldsymbol{\sigma}_t = \boldsymbol{\sigma}_0 + \mathbf{D}^e\Delta\boldsymbol{\varepsilon}_j \text{ (trial stress).}$$

$$\text{If } F(\boldsymbol{\sigma}_t, \kappa_j, \nabla^2\kappa_j) \geq -\varepsilon,$$

$$\text{then plastic state: } \boldsymbol{\sigma}_j = \boldsymbol{\sigma}_t - \Delta\lambda_j\mathbf{D}^e\mathbf{m}_t,$$

$$\text{else elastic state: } \boldsymbol{\sigma}_j = \boldsymbol{\sigma}_t.$$

4. Check global convergence criterion. If not converged, go to 1.

substituted in submatrix $\mathbf{K}_{\lambda\lambda}$ of the tangent operator to avoid singularity. Some more algorithmic consequences of the employed mixed element formulation have been described in Sections 4.1.1 and 4.1.2.

The update of the nodal variables is done in a 'total-incremental' way, i.e. in every iteration total increments from the equilibrium state at the end of the previous loading step are calculated. The advantage of this approach is that spurious unloading can be avoided. The increment of plastic multiplier $\Delta\lambda$ is determined from the nodal values of $\Delta\Lambda$ and there are no additional iterations at the integration point level as in the standard algorithm in Box 1. The stresses are analyzed starting from the equilibrium state $\boldsymbol{\sigma}_0$. For integration points in a plastic state the idea of elastic predictor (trial stress $\boldsymbol{\sigma}_t$) and plastic corrector $-\Delta\lambda\mathbf{D}^e\mathbf{m}$ is followed. The updated values of the hardening parameter κ_j and its Laplacian $\nabla^2\kappa_j$ are already available at the trial stress state and are used in the yield condition, but alternatively the memorized values from the previous increment κ_0 and $\nabla^2\kappa_0$ can be used, which results in a slightly delayed plastification. The relation of the present algorithm to the tangent-cutting-plane algorithm (Ortiz and Simo 1986) is not so close as in the 'delta-incremental' algorithm used by de Borst and Mühlhaus (1992).

Because the plastic multiplier is an independent variable determined in the solution

of the global set of equations, the weak form of the yield condition (4.2) is not satisfied until convergence is achieved. It can happen that due to stress redistribution or nonlinear softening the increment $\Delta\lambda$ results in a return mapping to the inside of the yield surface. In the present total-incremental algorithm this does not cause the detection of unloading, but changes sign of the residual forces, which results further in a proper correction (decrease) of $\Delta\lambda$. However, difficulties may arise, if the value of the yield function has different signs at the integration points within one element. The respective contributions to residual force \mathbf{f}_λ get averaged because of the weak formulation and improper values of corrections $d\mathbf{\Lambda}$ are obtained from the global set of equations. Therefore the best convergence is found for those finite elements (see Chapter 4.4), in which, at the sampling points, the value of the yield function F converges to zero with the decrease of the residual force norm.

On the other hand a corrective procedure has been suggested previously (de Borst and Mühlhaus 1992) in order to bring the stress point, mapped inside, back to the yield contour. This correction at the integration point level introduces an inconsistency between nodal and local updates of the plastic multiplier and sets residual force \mathbf{f}_λ to zero for a state with no equilibrium, which disturbs convergence of the incremental-iterative procedure. Therefore this method has been abandoned in the present algorithm.

The algorithm in Box 2 can also be used for gradient-independent plasticity. However, the introduction of additional nodal degrees of freedom makes it seem inferior to the standard return mapping algorithms. It is noted that for a homogeneous stress state the new formulation can be proved equivalent to the standard one. The degrees of freedom $d\mathbf{\Lambda}$ in eq. (4.25) can then be condensed and the interpolation of λ by means of a constant (unit) function leads to the tangent operator $\hat{\mathbf{K}}_{aa}$ in eq. (4.68).

4.2.3 Gradient-dependent yield strength

We will now present the adopted softening rules and the consequences of their gradient dependence. In eq. (4.14) we have already introduced a nonlinear softening rule

$$\bar{\sigma}_g(\kappa, \nabla^2 \kappa) = \bar{\sigma}(\kappa) - g(\kappa) \nabla^2 \lambda = \bar{\sigma}(\kappa) - \frac{g(\kappa)}{\eta} \nabla^2 \kappa, \quad (4.69)$$

in which $\bar{\sigma}(\kappa)$ is a given standard softening rule (Fig. 4.1), $g(\kappa)$ is a given gradient influence function and η is a positive constant according to eq. (3.45), introduced in order to comply with the definitions (3.48) and (3.49). The hardening modulus is then obtained from the definition (3.48):

$$h = \eta \frac{\partial \bar{\sigma}_g}{\partial \kappa} = \eta \bar{\sigma}'(\kappa) - g'(\kappa) \nabla^2 \kappa, \quad (4.70)$$

where the Laplacian is treated as an independent variable during differentiation. The third order terms are difficult to determine numerically and are neglected. We now generalize the relation between the variable g , the classical hardening modulus $\bar{\sigma}'$ and the internal length scale l , found for the one-dimensional analytical solution in Chapter 3.1,

to the case of nonlinear softening

$$g(\kappa) = -\eta l^2 \bar{\sigma}'(\kappa), \tag{4.71}$$

with l constant, and obtain for the gradient-dependent softening law:

$$\bar{\sigma}_g(\kappa, \nabla^2 \kappa) = \bar{\sigma}(\kappa) + l^2 \bar{\sigma}'(\kappa) \nabla^2 \kappa, \tag{4.72}$$

which reflects the decrease of the gradient influence with the increase of the accumulated plastic (inelastic) strain, corresponding to the gradual failure of microstructural deformation carriers for a fully developed plastic flow or progressive material damage.

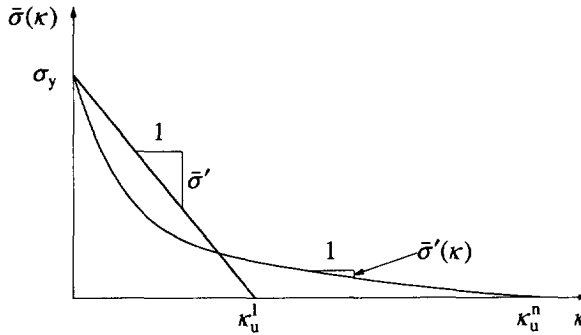


Figure 4.1 Linear and nonlinear softening diagrams.

The hardening modulus is then obtained from eq. (4.70):

$$h = \eta \bar{\sigma}'(\kappa) + \eta l^2 \bar{\sigma}''(\kappa) \nabla^2 \kappa. \tag{4.73}$$

The simplest case is to assume linear softening ($\bar{\sigma}' = \text{constant}$, Fig. 4.1) and a constant gradient influence coefficient g :

$$\bar{\sigma}_g(\kappa, \nabla^2 \kappa) = \sigma_y + \frac{h}{\eta} \kappa - \frac{g}{\eta} \nabla^2 \kappa, \quad h = \eta \bar{\sigma}'. \tag{4.74}$$

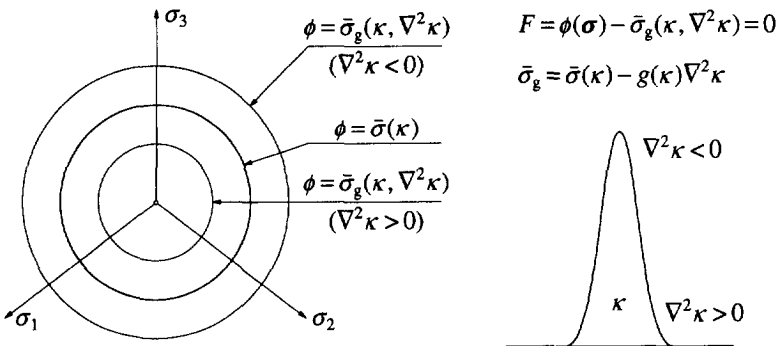


Figure 4.2 Gradient contribution to the yield strength.

In the following interpretation we will assume for simplicity that $\kappa = \lambda$ ($\eta = 1$). The

gradient-dependent yield strength in eq. (4.69) is composed of two contributions. The gradient contribution $-g(\kappa)\nabla^2\kappa$ may be positive or negative as presented in Fig. 4.2. The former case occurs in the middle of the localization band, giving additional carrying capacity to the gradient-dependent material in this area (even if $\bar{\sigma}$ already equals zero, the yield strength $\bar{\sigma}_g$ is still larger than zero). The case of negative gradient contribution occurs at the elastic-plastic boundary, making it possible for the localization zone to spread (the elastic elements close to the elastic-plastic boundary have apparently a reduced yield strength). These modifications of the standard yield strength function $\bar{\sigma}(\kappa)$ are the algorithmic essence of the gradient regularization.

We will further illustrate this feature on the one-dimensional stress-strain law used for the bar in tension in Chapters 2.1 and 3.1. With reference to the classical strain softening model plotted in Fig. 2.2 we present in Fig. 4.3 the gradient-dependent case. The distribution of equivalent plastic strains along the bar according to the analytical solution from Chapter 3.1 and the distribution of the second derivatives are plotted in Fig. 4.3 on the right. The influence of the gradient term on the $\sigma - \varepsilon$ diagrams, valid in different parts of the bar, is shown on the left. We analyze the equilibrium state $\sigma = \bar{\sigma}_g = \text{constant}$. For the largest strains ε^M (in the middle of the localization zone) we have a negative curvature of the function $\kappa(x)$ and an increased strength of the material. For the smaller strains ε^S corresponding to the saddle point of $\kappa(x)$ the original diagram is valid. For the even smaller strains ε^B observed at the points close to the elastic-plastic boundary we have a positive curvature and the strength of the material decreases. Because of the evolution of the plastic zone, the diagrams have a momentary character and change with the value of $\kappa_{,xx}$. This is also the case for the points in the elastic state close to the plastic zone (strain ε^E). With the further increase of $\kappa_{,xx}$ and associated decrease of the yield strength $\bar{\sigma}_g$ the elastic points can enter the plastic regime and start softening. This will happen rapidly at the beginning of the plastic process, when the plastic zone spreads from the imperfect elements to the size determined by the internal length scale.

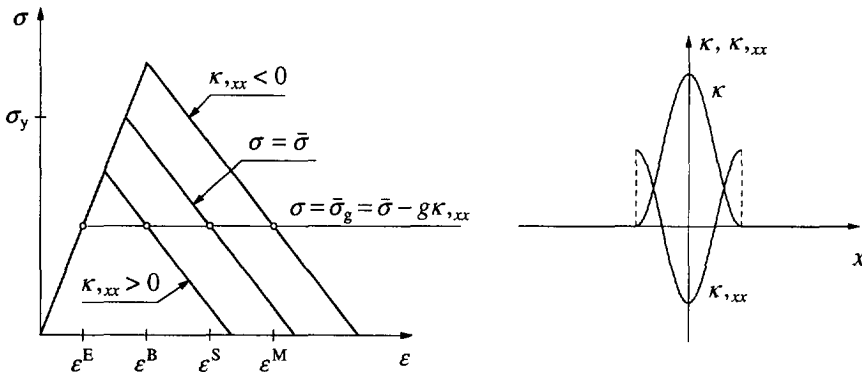


Figure 4.3 Gradient term influence on the strain-softening model for a uniaxial case; the equivalent plastic strain function $\kappa(x)$ and its second derivative.

We will now address the problem of the vanishing yield strength. When the local residual strength is exhausted in classical softening plasticity, i.e. when the yield surface has shrunk to zero ($\bar{\sigma}(\kappa) \rightarrow 0$), the further calculations should still be possible under displacement control (the whole further deformation should be plastic and the stresses should vanish). However, in this limiting case the yield function becomes singular and the tangent operator becomes ill-conditioned. To prevent this a small positive number can be introduced instead of zero as the limit value of the yield strength $\bar{\sigma}(\kappa_0)$ (cf. Fig. 4.1).

The problem is even more delicate in gradient plasticity. As shown in Figs 4.2 and 4.3, the limit case $\bar{\sigma}_g \rightarrow 0$ can be reached at a state, for which the softening diagram is still followed ($\bar{\sigma} > 0$ and $\kappa < \kappa_0$). This happens easily for linear softening and is less severe for the nonlinear softening in Fig. 4.1, since the gradient contribution in eq. (4.72) goes to zero together with $\bar{\sigma}(\kappa)$.

To prevent numerical difficulties occurring when the yield strength reaches zero as well as the unacceptable situation of a negative $\bar{\sigma}_g$, its value is bounded by a small positive number (e.g. $\bar{\sigma}_g > 10^{-3}$) and a corrective procedure is suggested to avoid a spurious return mapping to stress states of the opposite sign. The procedure resolves in one additional (global) iteration the case of return mapping to the other side of the shrinking yield surface as well as to the inside of the yield surface (cf. Fig. 4.2). From the numerical viewpoint, for nonlinear softening both limits $\bar{\sigma}_g \rightarrow 0$ and $g \rightarrow 0$ should be avoided, the latter one because when the gradient contribution vanishes the calculations will become mesh-dependent again. Therefore nonlinear softening to zero is not allowed and the values of $\bar{\sigma}$ and g for $\kappa = 0.98\kappa_0$ are kept constant for $\kappa > 0.98\kappa_0$. From the physical viewpoint, the element topology should be modified at this stage by introducing interface elements modelling a discrete displacement discontinuity.

4.3 Two-dimensional cases

For the finite element approximation in two dimensions the displacement field $\mathbf{u} = (u, v)$ is interpolated within an element according to:

$$\mathbf{u} = \mathbf{N}\mathbf{a} = \sum_{i=1}^n \mathbf{N}_i(\xi, \eta) \mathbf{a}_i, \quad (4.75)$$

where the shape function matrix and the nodal displacement vector for each node i are:

$$\mathbf{N}_i = \begin{bmatrix} N_i & 0 \\ 0 & N_i \end{bmatrix}, \quad \mathbf{a}_i = \begin{bmatrix} a_{xi} \\ a_{yi} \end{bmatrix} \quad (4.76)$$

and n is the number of element nodes.

In the plane strain conditions $\varepsilon_z = 0$ we will use the strain vector $\boldsymbol{\varepsilon} = (\varepsilon_x, \varepsilon_y, \gamma_{xy}, \varepsilon_z)$ and the stress vector $\boldsymbol{\sigma} = (\sigma_x, \sigma_y, \sigma_{xy}, \sigma_z)$. In the plane stress state $\sigma_z = 0$ we will use the strain vector $\hat{\boldsymbol{\varepsilon}} = (\varepsilon_x, \varepsilon_y, \gamma_{xy})$ and the stress vector $\hat{\boldsymbol{\sigma}} = (\sigma_x, \sigma_y, \sigma_{xy})$.

The gradient-dependent plasticity relations for the plane strain conditions can be obtained directly from the general continuum case by removing the components associated with the out-of-plane shear and setting ε_z to zero. In the next section we will only

address briefly the classical problem of kinematic constraints in finite element approximations, which is relevant also for gradient plasticity elements.

The adaptation of the general theory is slightly more complex for the plane stress conditions, since the algorithm of stress computation is strain-driven. In Section 4.3.2 we will summarize the possible solutions applied to gradient plasticity.

4.3.1 Plane strain case

The differential operator matrix \mathbf{L} for the plane strain case has the form:

$$\mathbf{L}^T = \begin{bmatrix} \frac{\partial \cdot}{\partial x} & 0 & \frac{\partial \cdot}{\partial y} & 0 \\ 0 & \frac{\partial \cdot}{\partial y} & \frac{\partial \cdot}{\partial x} & 0 \end{bmatrix}. \quad (4.77)$$

The strains are then represented as:

$$\boldsymbol{\varepsilon} = \mathbf{B}\mathbf{a} = \sum_{i=1}^n \mathbf{B}_i(\xi, \eta) \mathbf{a}_i, \quad (4.78)$$

with the strain-nodal displacement matrix $\mathbf{B}_i = \mathbf{L}\mathbf{N}_i$ for node i as follows

$$\mathbf{B}_i = \begin{bmatrix} B_1 & 0 \\ 0 & B_2 \\ B_2 & B_1 \\ 0 & 0 \end{bmatrix}, \quad (4.79)$$

where $B_1 = \partial N_i / \partial x$, and $B_2 = \partial N_i / \partial y$. The form of \mathbf{B} assures the satisfaction of the plane strain condition $\varepsilon_z = 0$. The elastic stiffness matrix \mathbf{D}^e reads:

$$\mathbf{D}^e = \frac{E}{(1+\nu)(1-2\nu)} \begin{bmatrix} 1-\nu & \nu & 0 & \nu \\ \nu & 1-\nu & 0 & \nu \\ 0 & 0 & \frac{1-2\nu}{2} & 0 \\ \nu & \nu & 0 & 1-\nu \end{bmatrix}, \quad (4.80)$$

where E is Young's modulus and ν is Poisson's ratio.

In elastically volume-preserving solids, i.e. when Poisson's ratio approaches $1/2$, the \mathbf{D}^e matrix becomes unbounded (with the exception of shear terms) and some standard plane strain (and axisymmetric) elements exhibit locking behaviour. Material incompressibility introduces a kinematic constraint imposing increased requirements on the finite element approximation. The remedy for this difficulty has first been found in mixed formulations (see e.g. Hughes 1987), in which the hydrostatic pressure is treated as an independent unknown and is interpolated separately. This approach has been shown to be similar to the technique of selective reduced integration of the volumetric part of the virtual strain energy.

A similar locking phenomenon appears, when a perfect plasticity model is used with a pressure independent yield criterion (plastically volume-preserving solid). At collapse the stress rate vanishes and so does the elastic strain rate. Since the plastic deformation is isochoric, the volumetric strain rate must vanish. Moreover, it has been shown

recently (de Borst and Groen 1994) that in case of pressure dependent yield functions, which lead to a dilatant or contractant plastic flow, a kinematic constraint is also present in the problem and may cause locking similar to the case of isochoric conditions.

A fairly simple solution of the incompressibility problems has been found in the modification of the strain-nodal displacement matrix \mathbf{B} based on the mean-dilatation approach (Nagtegaal et al 1974). This \bar{B} -enhancement is a generalization of the reduced integration concept and can be easily applied to nonlinear analysis (Hughes 1980). For gradient plasticity it is especially convenient, as it allows to avoid the mixed approach at this level of formulation. Therefore it is used in this thesis for the four-noded plane strain elements. The eight-noded and nine-noded elements are less sensitive to volumetric locking, but the use of reduced integration is advisable.

4.3.2 Plane stress case

For the case of plane stress conditions the matrices $\hat{\mathbf{L}}$ and $\hat{\mathbf{B}}_i$ are obtained by removing the fourth rows in matrices defined in (4.77) and (4.79), respectively. The stiffness matrix $\hat{\mathbf{D}}^e$ reads:

$$\hat{\mathbf{D}}^e = \frac{E}{(1-\nu^2)} \begin{bmatrix} 1 & \nu & 0 \\ \nu & 1 & 0 \\ 0 & 0 & (1-\nu)/2 \end{bmatrix}. \quad (4.81)$$

In the first approach to the plane stress problem (cf. de Borst 1991₁) the strain state is expanded to a four-component case, plane strain constitutive equations are used with the additional condition $\sigma_z = 0$ and finally the stress state is compressed to three components. The derivation leads to modified versions of the algorithmic matrix \mathbf{H} and the vector of internal forces \mathbf{f}_a .

Starting from the consistent linearization (4.63) in iteration j we can write:

$$\boldsymbol{\sigma}^j = \mathbf{H}d\boldsymbol{\varepsilon} - \mathbf{H}d\lambda\mathbf{m} + \boldsymbol{\sigma}^{j-1}, \quad (4.82)$$

where \mathbf{H} for the plane strain (continuum) case is defined by (4.64), $d\boldsymbol{\varepsilon}$ and $d\lambda$ are calculated on the basis of the nodal increments $d\mathbf{a}$ and $d\Lambda$, respectively. We perform a partition of all the vectors and matrices:

$$\begin{bmatrix} \boldsymbol{\sigma}^j \\ \sigma_z^j \end{bmatrix} = \begin{bmatrix} \mathbf{H}_{11} & \mathbf{H}_{12} \\ \mathbf{H}_{21} & H_{22} \end{bmatrix} \begin{bmatrix} d\hat{\boldsymbol{\varepsilon}} \\ d\varepsilon_z \end{bmatrix} - d\lambda \begin{bmatrix} \mathbf{H}_{11} & \mathbf{H}_{12} \\ \mathbf{H}_{21} & H_{22} \end{bmatrix} \begin{bmatrix} \hat{\mathbf{m}} \\ m_{22} \end{bmatrix} + \begin{bmatrix} \boldsymbol{\sigma}^{j-1} \\ \sigma_z^{j-1} \end{bmatrix}. \quad (4.83)$$

Next, we enforce the plane stress condition $\sigma_z^j = 0$:

$$\sigma_z^j = \mathbf{H}_{21}d\hat{\boldsymbol{\varepsilon}} + H_{22}d\varepsilon_z - d\lambda(\mathbf{H}_{21}\hat{\mathbf{m}} + H_{22}m_{22}) + \sigma_z^{j-1} = 0 \quad (4.84)$$

and calculate the increment of the normal strain in z -direction

$$d\varepsilon_z = -\frac{1}{H_{22}} [\mathbf{H}_{21}d\hat{\boldsymbol{\varepsilon}} - d\lambda(\mathbf{H}_{21}\hat{\mathbf{m}} + H_{22}m_{22}) + \sigma_z^{j-1}], \quad (4.85)$$

where σ_z^{j-1} may be non-zero until convergence is reached. Substitution of eq. (4.85) into eq. (4.83) gives after reformulation:

$$\hat{\sigma}^j = \tilde{\mathbf{H}}_{11} d\hat{\varepsilon} - d\lambda \tilde{\mathbf{H}}_{11} \hat{\mathbf{m}} + \hat{\sigma}^{j-1} - \frac{\mathbf{H}_{12}}{H_{22}} \sigma_z^{j-1} \quad (4.86)$$

with

$$\tilde{\mathbf{H}}_{11} = \mathbf{H}_{11} - \frac{\mathbf{H}_{12}\mathbf{H}_{21}}{H_{22}}. \quad (4.87)$$

Eq. (4.86) is then inserted in the equation of equilibrium:

$$\int_V \hat{\mathbf{B}}^T \hat{\sigma}^j dV = \hat{\mathbf{f}}_e, \quad (4.88)$$

which results in:

$$\int_V (\hat{\mathbf{B}}^T \tilde{\mathbf{H}}_{11} \hat{\mathbf{B}} da) dV - \int_V (\hat{\mathbf{B}}^T \tilde{\mathbf{H}}_{11} \hat{\mathbf{m}} h^T d\Lambda) dV = \hat{\mathbf{f}}_e - \int_V \hat{\mathbf{B}}^T \left(\hat{\sigma}^{j-1} - \frac{\mathbf{H}_{12}}{H_{22}} \sigma_z^{j-1} \right) dV. \quad (4.89)$$

This is similar to the set of equilibrium equations (4.21). The comparison with the original algorithm (de Borst 1991₁) proves that the necessary correction in the consistent algorithmic matrix \mathbf{H} in eq. (4.87) and in the internal force vector in eq. (4.89) are similar to those derived for the standard plasticity algorithm. Only the strain increment $d\varepsilon_z$ must be calculated according to eq. (4.85).

If the yield criterion is formulated only in the plane stress state, the above approach cannot be used. Therefore a separate formulation of the constitutive equations for the plane stress case has additionally been developed (cf. Crisfield 1991). It appears that with the three-component definitions of strain and stress and relevant yield conditions the whole theory and algorithm described previously remain valid for the case of plane stress. This includes also the derivation of the algorithmic matrix $\hat{\mathbf{H}}$ consistent with the used stress update method (cf. Simo and Taylor 1986).

4.4 Finite elements

All two-dimensional elements implemented in a pilot version of the DIANA code are listed in Table 1 after the references (plane stress and plane strain versions are included). To analyze the ability of the elements to give proper convergence and distribution of plastic strains, a simple one-dimensional deformation patch test has been used. Since the regularization effect of gradient plasticity is only activated in a state of non-uniform plastic deformation, the behaviour of the mixed approximation can only be tested on an imperfect model and in the nonlinear regime.

We examine a beam of length L in a state of pure shear (Fig. 4). The beam has a 10% weaker zone of length $L/2$ in the middle. Discretization with four rectangular elements or eight triangular elements is used. Linear dependence relations and supports enforcing a symmetric one-dimensional deformation are introduced in addition to the boundary conditions for λ ($\Lambda_x = 0$ at both ends). Since the configuration is strongly constrained, the results should not be automatically extended to other models. However, some insight into the distribution of the plastic multiplier and its derivatives as well as convergence characteristics are obtained. The manner, in which C^0 -continuous interpolation of λ is enhanced using an extra variable φ (constrained to be equal to $\lambda_{,x}$ in the

integration points), is also illustrated.

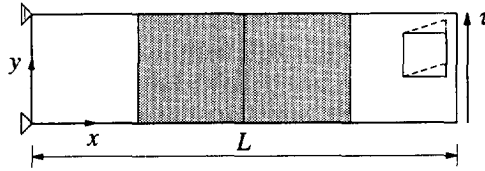


Figure 4.4 Configuration of the patch test for gradient plasticity elements (weaker zone shaded).

We will now review the features and performance of all developed elements. Some more tests and comparisons will be presented in Chapter 5.

4.4.1 One-dimensional elements

Fig. 4.5 shows the simplest one-dimensional gradient plasticity elements with C^1 -continuity (see Section 4.1.1). The only displacement u_x (extension of the bar) is interpolated linearly or quadratically and for the plastic multiplier λ the cubic hermitian shape functions are used.

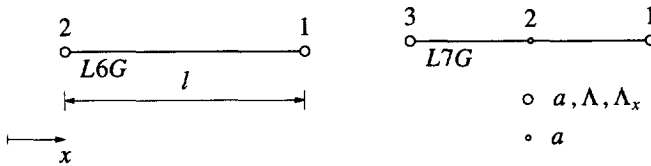


Figure 4.5 One-dimensional C^1 -elements.

For element $L6G$ two-point Gaussian integration is employed. Matrix $K_{\lambda\lambda}$ includes polynomials of the sixth order and is not integrated accurately. Translation in the x direction must be prevented and two additional constraints (e.g. symmetry) or boundary conditions for the λ field should be introduced in a model. The number of extra constraints is determined as follows: 2×2 degrees of freedom for λ minus 2×1 relations in Gauss points equals 2. The element yields an exact fulfilment of the yield condition at the integration points, which means that when $f_\lambda \rightarrow 0$, then $F_{ip} \rightarrow 0$, but stress oscillations are observed. This phenomenon may cause a failure of convergence at an early stage of softening as soon as the oscillating stresses reach a state with $\bar{\sigma}_g \rightarrow 0$.

For element $L7G$ with two-point integration the balance between the interpolation for u_x and λ is optimal, i.e. the return mapping in eq. (4.60) gives a stress state σ_j , which is constant within an element and which fulfils exactly the yield condition (convergence in one iteration is observed unless the softening zone spreads or nonlinear softening is used). This behaviour is attributed to the special qualities of the integration stations, so-called Barlow points (Barlow 1976), at which higher order accuracy of interpolated field derivatives is obtained. In fact, these are the only points, in which the third order terms in $F_j(\sigma_j, \lambda_j, \nabla^2 \lambda_j)$ coincide with the first order terms, so that the yield

function itself equals zero.

The above properties are exhibited by the nonsymmetric formulation with $\mathbf{K}_{\lambda\lambda}$ from eq. (4.28). If the symmetric format for $\mathbf{K}_{\lambda\lambda}$ according to eq. (4.32) is used together with the required boundary conditions and two-point (reduced) integration, convergence is lost. This behaviour is attributed to an unfavourable numerical integration error, since for three-point (full) integration the symmetric and nonsymmetric formulation give the same results. However, for the three-point integration too many constraints are introduced and inaccurate results are obtained. The stresses at one or more points are then mapped to the inside of the yield surface ($F_j < 0$), which violates the Kuhn-Tucker conditions (3.41) and results in a disturbance of convergence: F_{ip} does not converge to zero in the iterative process and stress oscillations are present.

Fig. 4.6 shows the one-dimensional C^0 -elements with separate Lagrange interpolation of the longitudinal displacement u_x , the plastic multiplier λ and the additional variable φ (see Section 4.1.2).

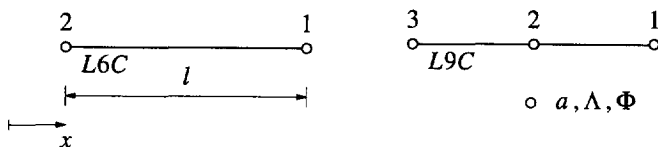


Figure 4.6 One-dimensional C^0 -elements with a constraint.

Element L6C uses linear shape functions and one integration point. It is the point, in which the constraint $\varphi = \lambda_{,x}$ is fulfilled (cf. the illustration for the patch test with element Q20MC in the next section). The longitudinal translation must be prevented and two boundary conditions for λ or φ should be introduced in a model (2×3 degrees of freedom minus 3 relations in the Gauss point equals 3; the tangent operator for an elastic element has 3 zero eigenvalues). The element is perfectly convergent since the integration station is a Barlow point (Barlow 1976). Element L9C uses quadratic shape functions and two Gauss points, which are optimal for convergence. Boundary conditions similar to the previous element must be introduced and as for L6C the return mapping in eq. (4.60) is exact.

In the presence of the additional boundary conditions (4.54) the symmetric and nonsymmetric formulations give the same results for the one-dimensional C^0 -elements, because the employed numerical integration schemes are sufficient for an exact integration of the shape function polynomials. Application to a test of strain localization in a bar is given in Chapter 5.2.

4.4.2 Quadrilateral elements

Fig. 4.7 shows a family of rectangular elements with a varying interpolation of the displacements and the same bi-hermitian shape functions for the plastic strain field. The elements are formulated in a Cartesian global reference system and cannot be transformed because of the presence of the mixed derivative degrees of freedom Λ_{xy} in the

C^1 -interpolation of λ . Only the nonsymmetric formulation of the problem (4.25) yields fully convergent results.

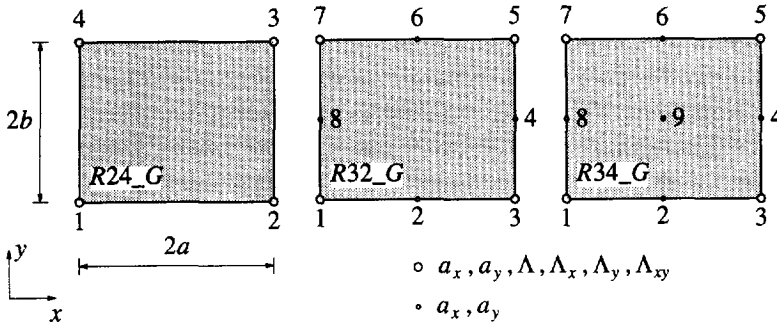


Figure 4.7 Rectangular C^1 -elements.

Element $R24_G$, introduced by Pamin and de Borst (1992), employs bilinear interpolation of displacements and 2×2 point integration (notice that the names of the plane stress and plane strain versions of the elements are obtained by substitution of M and E , respectively, for the underscore mark, cf. Table 1 after the references). To avoid volumetric locking in plane strain problems, \bar{B} -enhancement is used (Hughes 1980). To avoid shear locking, the shear terms are integrated using only 1 Gauss point. Matrix \mathbf{K}_{aa} possesses the correct rank, see also the discussion after eq. (4.35). The matrix $\mathbf{K}_{\lambda\lambda}^c$ requires 12 additional constraints ($4 \times 4 - 4 \times 1 = 12$) and they can be introduced by extra boundary conditions for derivatives of λ . For an arbitrary assembly the conditions $\Lambda_n = 0$ and $\Lambda_{xy} = 0$ on the whole model boundary supply exactly the required number of constraints. Element $R24_G$ gives $F_{ip} \rightarrow 0$, but like $L6G$ shows stress oscillations due to the lack of balance between the employed interpolations.

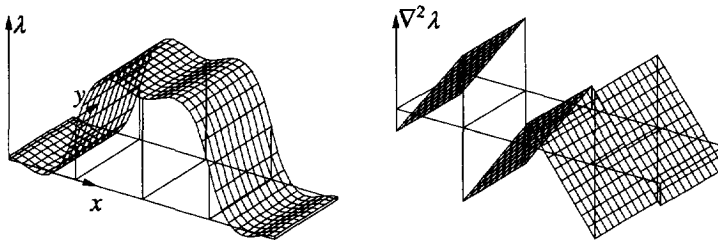


Figure 4.8 Patch test for $R24_G$ ($2 \times 2/1$ Gauss points), $\nabla^2 \lambda$ is not optimal (stress oscillations observed).

Fig. 4.8 shows the distribution of the plastic multiplier and its Laplacian along the bar plotted in Fig. 4.4. All integration points in the two centre elements exhibit the plastic state. The integration points in the elements at the bar ends are elastic and it is observed that while the plastic multiplier is zero at these points, the Laplacian has a non-zero value. In the middle of the plastic zone the Laplacian is positive, which results in stress

oscillations.

Element $R32_G$ employs eight-noded serendipity interpolation of displacements and 2×2 Gauss integration. The matrix \mathbf{K}_{aa} possesses one zero-energy mode that disappears in an assembly of elements. With the matrix $\mathbf{K}_{\lambda\lambda}^c$ described above, this element shows proper convergence to a state with $F_{ip} \rightarrow 0$ and vanishing stress oscillations and is the most reliable of C^1 -elements. The behaviour of this element in the patch test from Fig. 4.4 is illustrated in Fig. 4.9. We observe that owing to a proper balance of interpolations the Laplacian is negative in the middle of the plastic zone, which results in a pointwise satisfaction of equilibrium (the stress is constant along the bar).

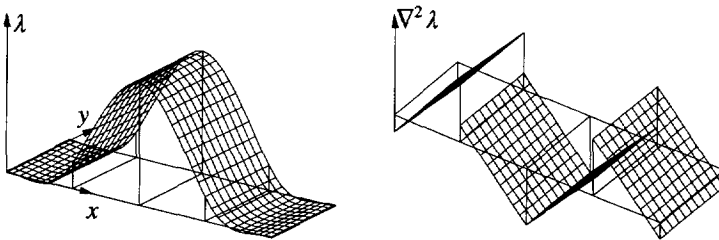


Figure 4.9 Patch test for $R32_G/R34_G(2 \times 2)$, optimal behaviour.

Table 1 includes also the plane strain non-conforming version of this element called $R28EG$, in which the $\Lambda_{xy} = 0$ degrees of freedom are skipped, but this element has worse convergence characteristics.

Element $R34_G$ employs bi-quadratic lagrangian interpolation of displacements and 2×2 numerical integration. The element shows excellent behaviour, but only in sufficiently constrained configurations, since the matrix \mathbf{K}_{aa} possesses three zero-energy modes, two of which propagate in an assembly of elements. With 3×3 integration the rank of \mathbf{K}_{aa} is correct and in an assembly no extra boundary conditions for λ are necessary. However, these sampling points are not optimal for our problem (cf. the description of element $L7G$), mapping of stresses to the inside of the yield surface takes place at some Gauss points and convergence is gradually lost. Selective $(3 \times 3/2 \times 2)$ integration of matrices \mathbf{K}_{aa} and $\mathbf{K}_{\lambda\lambda}$ is not easily achieved because of the presence of the coupling matrices $\mathbf{K}_{\lambda a}$ in eq. (4.25). To preserve the optimal integration scheme for the yield condition and remove zero-energy deformation modes from element $R34_G$, hour-glass control techniques could be used (cf. Wong and Belytschko 1987, Liu et al 1985), but the addition of a stabilization matrix to \mathbf{K}_{aa} affects the consistency of linearization and the presence of incompatible modes affects the accuracy of the return mapping, which leads to convergence deterioration.

Fig. 4.10 shows three penalty-enhanced C^0 -continuous quadrilaterals employing linear, quadratic serendipity and quadratic lagrangian interpolation functions for all the unknowns. The elements are formulated in a Cartesian global reference system, but they can be transformed. Both the nonsymmetric and symmetric formulation from

Section 4.1.2 yield convergent results.

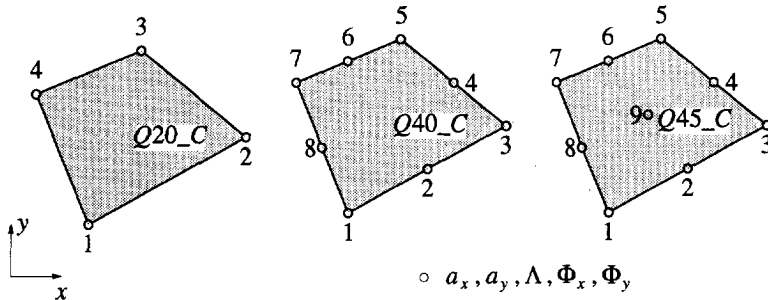


Figure 4.10 Quadrilateral penalty-enhanced C^0 -elements.

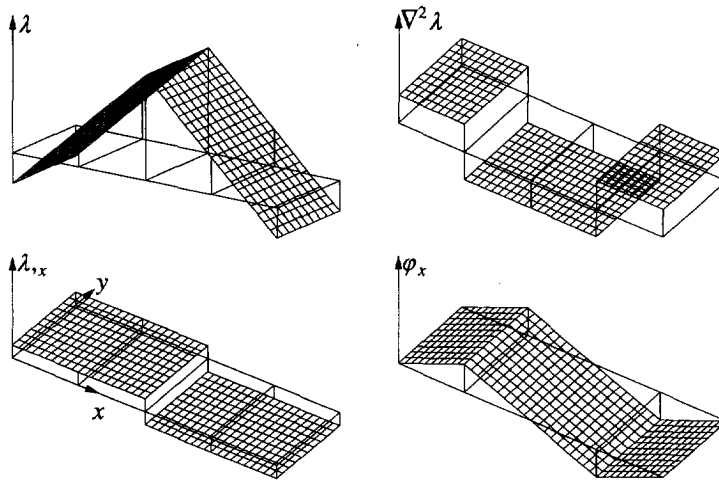


Figure 4.11 Patch test for $Q20_C(1)$, optimal penalty constraint and $\nabla^2 \lambda$.

All shape functions for element $Q20_C$ are linear. Because of the penalty constraint this element can yield proper convergence only if one-point integration is used. Fig. 4.11 shows that in the patch test the linear distribution of the plastic multiplier is then associated with the optimal constant values of the Laplacian calculated as $\nabla^T \phi$. The constant distribution of $\lambda_{,x}$ is enhanced by the use of the additional variable ϕ_x , which is linear and equal to $\lambda_{,x}$ at the element centre. With 2×2 Gauss integration the element locks (no zero eigenvalues exist in $\mathbf{K}_{\lambda\lambda}^e$, the constraint $\phi_x = \lambda_{,x}$ is true everywhere and as a result the Laplacian is zero).

However, a large number of zero-energy modes are present if one-point integration is employed: 2 hourglass modes for the displacement field \mathbf{u} (5 zero eigenvalues in \mathbf{K}_{aa}) and 9 hourglass modes for the λ field (9 zero eigenvalues in $\mathbf{K}_{\lambda\lambda}^e$) unless extra boundary conditions are introduced. The hourglass deformations can in principle be controlled, but as in the case of the nine-noded element $R34_G$ the anti-hourglass stiffness based

on γ fields (Belytschko et al 1984) or assumed strain fields (Jetteur and Cescotto 1991) would most probably interfere with the gradient plasticity algorithm. No satisfactory way of controlling the spurious modes for λ has been found and the number of available boundary conditions is in general insufficient. Consequently the element cannot be applied unless one point integration is used in strongly constrained configurations.

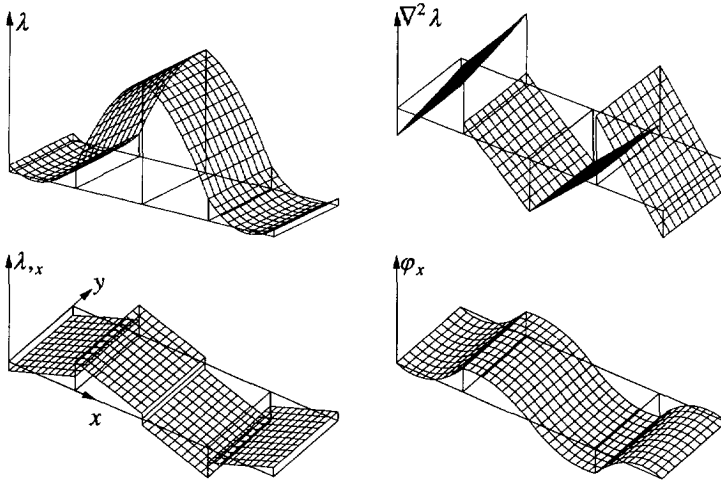


Figure 4.12 Patch test results for $Q45_C(2 \times 2)$.

The quadratic Lagrange element $Q45_C$ with 2×2 integration converges perfectly (both $f_\lambda \rightarrow 0$ and then $F_{ip} \rightarrow 0$). The results of the patch test in Fig. 4.12 show the proper distribution of λ and $\nabla^2 \lambda$ obtained owing to the introduction of the additional variable ϕ_x and the optimal number of penalty constraints. However, element $Q45_C$ possesses zero-energy modes for \mathbf{u} (see the description of the nine-noded element $R34_G$) and also spurious modes for λ . In an arbitrary mesh the boundary conditions for ϕ_x or ϕ_y are not sufficient to assure the correct rank of the $\mathbf{K}_{\lambda\lambda}^e$ matrix and additional conditions for λ itself on part of the boundary are necessary to obtain a correct solution.

The quadratic serendipity element $Q40_C$ with 2×2 integration does not converge very well, since the return mapping in eq. (4.60) is inaccurate. Apparently the quadratic terms missing in the serendipity interpolation are important for interpolation compatibility. Since an assembly of elements $Q40_C$ does not possess hourglass deformation modes, a combination of 8-noded interpolation of displacements and 9-noded interpolation of the λ and ϕ fields is suggested and gives rise to element $Q43_C$ (a similar modification has been suggested for ‘heterosis’ plate bending elements, cf. for instance Zienkiewicz and Taylor 1991). This element converges better and is a C^0 equivalent of the eight-noded element $R32_G$.

4.4.3 Triangular elements

For a triangular element geometry the problem of choosing well-balanced interpolations of displacements and plastic multiplier as well as an optimal integration scheme becomes more difficult. Experience with rectangles suggests the use of the lowest possible interpolation order and reduced integration. Fig. 4.13 shows two triangular elements, which have a quadratic interpolation of displacements. The elements are formulated in area coordinates and, to avoid transformations, are referred to the global axes.

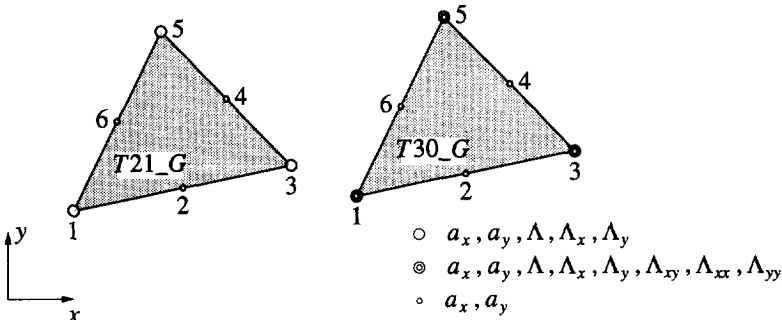


Figure 4.13 Triangular C^1 -elements.

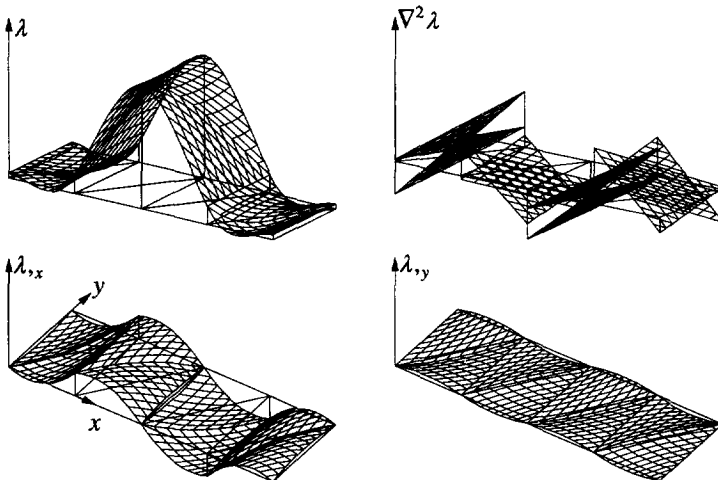


Figure 4.14 Patch test for $T_{21_G}(3)$, not converged, $F_{ip} \neq 0$ and stress oscillations observed.

The first element, called T_{21_G} , has a cubic interpolation of λ based on a non-conforming plate bending triangle (Zienkiewicz and Taylor 1991). The element does not fulfil the continuity requirements for λ_n on its boundary and is included in the present group because of the presence of Λ_x and Λ_y degrees of freedom. In the patch test the

plastic multiplier shows a reasonable distribution (Fig. 4.14), but λ_x is indeed discontinuous and λ_y is non-zero even though the problem is one-dimensional. Integration with 3 Gauss points is used, but the use of 3 Hammer points at midsides of the triangle does not improve the accuracy or convergence. These points are not optimal: $F_{ip} < 0$ and stress oscillations are found. Additional boundary conditions for the plastic multiplier field are necessary to prevent the existence of non-zero λ modes in elastic elements. If the λ field is sufficiently constrained (like in the pure shear patch test from Fig. 4.4), the use of one-point integration may improve convergence, but spurious non-zero values of λ are found in elastic elements.

Element *T30_G* employs the shape functions derived by Dasgupta and Sengupta (1990) and is fully C^1 -compatible, has a quintic interpolation of λ and cubic distribution of λ_n along the sides. To prevent spurious λ modes 6 integration points and extra boundary conditions, involving Λ_n or Λ (and sometimes also second order derivatives of the plastic multiplier) are usually necessary.

It seems that for the above elements it is not possible to find sampling points, in which higher order accuracy of stress approximation and convergence of F_{ip} to zero is obtained. Consequently neither of them exhibits fast convergence and stress oscillations are observed that may lead to violation of the positive yield strength condition and sometimes also to local unloading. Nevertheless, in our tests (see Chapter 5.3) they give reasonable predictions of the global response and shear banding.

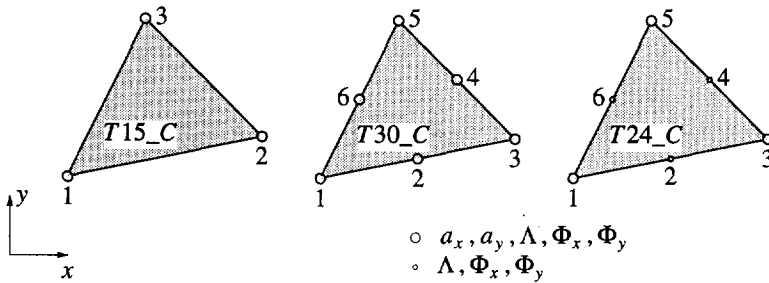


Figure 4.15 Triangular penalty-enhanced C^0 -elements.

It is also more difficult to find C^0 -continuous triangular elements satisfying the requirements for interpolation and numerical integration mentioned in Section 4.1.2. We have limited our research to a low order interpolation. Fig. 4.15 shows the three tested elements. The elements are formulated in area coordinates and referred to the global axes, but their transformations are possible.

The first element, called *T15_C*, has a linear interpolation of all fields and uses one-point integration. The element has too many constraints in both standard and crossed diagonal meshes and does not converge.

Element *T30_C* has a uniform quadratic interpolation and is integrated using 3 Gauss points. Though full convergence is not achieved, $F_{ip} < 0$ and stress oscillations are found, this element gives acceptable results. In constrained configurations the use of

one-point integration yields fast convergence and three integration points may cause locking. This is illustrated in Fig. 4.16, where the fields of φ_x and $\lambda_{,x}$ are the same and the Laplacian $\nabla^2 \lambda = \nabla^T \phi$ is incorrect.

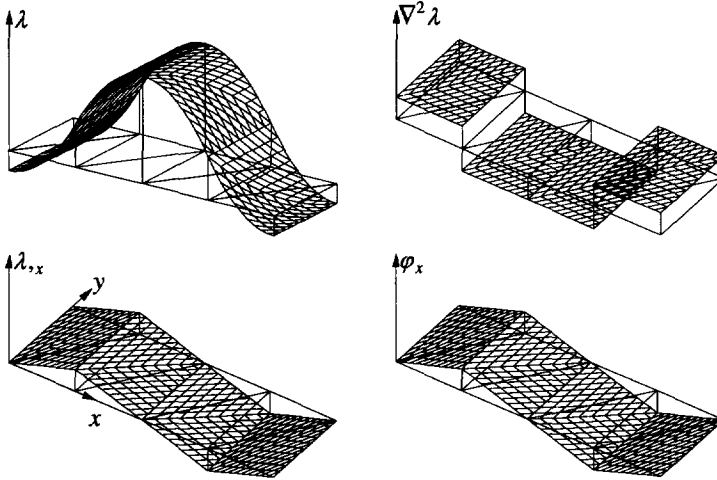


Figure 4.16 Patch test for $T30_C(3)$, not converged, $F_{ip} \neq 0$, too many penalty constraints, $\nabla^2 \lambda$ incorrect.

In an arbitrary configuration the tangent operator determined using only one Gauss point is strongly rank-deficient and a solution cannot be obtained. This suggests the implementation of element $T24_C$, having a linear interpolation of displacements and quadratic shape functions for the other fields, to be used with one-point integration. However, this element shows an acceptable performance only in strongly constrained configurations, but fails otherwise as the previous one.

5. Mesh-sensitivity studies

In this chapter we will present some results of one-dimensional and two-dimensional localization tests to demonstrate that the present formulation removes the spurious mesh sensitivity of finite element simulations. We will also compare the performance of available gradient plasticity elements, described in the previous chapter. We will limit our consideration to a gradient-enhanced J_2 plasticity with an associated flow rule.

5.1 Huber-Mises gradient plasticity

The Huber-Mises gradient-dependent yield function can be written in the following format:

$$F = \sqrt{3J_2} - \bar{\sigma}_g(\kappa, \nabla^2 \kappa), \quad (5.1)$$

where J_2 is the second invariant of the deviatoric stress tensor and $\bar{\sigma}_g$ is the yield strength. Introducing a symmetric matrix \mathbf{P} , which for plane strain conditions has the form:

$$\mathbf{P} = \begin{bmatrix} 2/3 & -1/3 & 0 & -1/3 \\ -1/3 & 2/3 & 0 & -1/3 \\ 0 & 0 & 2 & 0 \\ -1/3 & -1/3 & 0 & 2/3 \end{bmatrix}, \quad (5.2)$$

the function F can be written in the following form:

$$F = \left(\frac{3}{2} \boldsymbol{\sigma}^T \mathbf{P} \boldsymbol{\sigma}\right)^{1/2} - \bar{\sigma}_g(\kappa, \nabla^2 \kappa). \quad (5.3)$$

The gradient to the yield function equals

$$\mathbf{n} = \frac{\partial F}{\partial \boldsymbol{\sigma}} = \frac{3\mathbf{P}\boldsymbol{\sigma}}{2\left(\frac{3}{2} \boldsymbol{\sigma}^T \mathbf{P} \boldsymbol{\sigma}\right)^{1/2}} \quad (5.4)$$

and the second derivative, necessary to determine the algorithmic matrix \mathbf{H} in the consistent approach follows from:

$$\frac{\partial^2 F}{\partial \boldsymbol{\sigma}^2} = \left(\frac{3}{2}\right)^{1/2} \frac{\boldsymbol{\sigma}^T \mathbf{P} \boldsymbol{\sigma} \mathbf{P} - \mathbf{P} \boldsymbol{\sigma} \boldsymbol{\sigma}^T \mathbf{P}}{(\boldsymbol{\sigma}^T \mathbf{P} \boldsymbol{\sigma})^{3/2}}. \quad (5.5)$$

To determine the value of the constant η from eq. (3.45) we adopt the strain-hardening hypothesis:

$$\dot{\kappa} = \left(\frac{2}{3} \dot{\boldsymbol{\varepsilon}}_ij^p \dot{\boldsymbol{\varepsilon}}_ij^p\right)^{1/2} = \left[\frac{2}{3} (\dot{\boldsymbol{\varepsilon}}^p)^T \mathbf{Q} \dot{\boldsymbol{\varepsilon}}^p\right]^{1/2}, \quad (5.6)$$

with $\mathbf{Q} = \text{diag}[1, 1, 1/2, 1]$ for plane strain conditions. Substituting the plastic strain rate vector $\dot{\boldsymbol{\varepsilon}}^p = \dot{\lambda} \mathbf{n}$ into the definition of $\dot{\kappa}$ and noting that $\mathbf{P}\mathbf{Q}\mathbf{P} = \mathbf{P}$ we obtain:

$$\dot{\kappa} = \dot{\lambda}. \quad (5.7)$$

Accordingly for Huber-Mises gradient plasticity the softening rules and the algorithm in

Chapter 4 hold with $\eta = 1$.

5.2 One-dimensional tests

We will analyze numerically the imperfect bar in tension shown in Fig. 5.1 (cf. de Borst and Mühlhaus 1992 and Section 2.1.3).

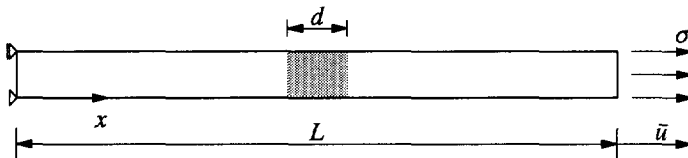


Figure 5.1 Imperfect bar in pure tension.

For this problem the equivalent stress in the Huber-Mises yield function reduces to the normal stress σ_x and the following failure condition is obtained:

$$F = \sigma_x - \bar{\sigma}_g, \quad \bar{\sigma}_g = \bar{\sigma}(\kappa) - g(\kappa) \frac{d^2 \kappa}{dx^2}. \quad (5.8)$$

The hardening parameter κ is now equal to the plastic multiplier λ and the plastic strain ϵ_x^p . According to the analytical solution derived in Section 3.1.1 for the case of linear softening the width of the localization zone w is related to the constant g via the internal length l and the hardening (softening) modulus $h = \bar{\sigma}'$:

$$w = 2\pi l, \quad l = \sqrt{-g/h}. \quad (5.9)$$

In the calculations the length of the bar is $L = 100 \text{ mm}$, Young's modulus $E = 20000 \text{ N/mm}^2$, the tensile strength $\sigma_y = 2 \text{ N/mm}^2$. One-dimensional gradient plasticity elements described in Section 4.4.1 have been employed. Two meshes of 20 and 80 elements have been used to examine the mesh-dependence of results. The elements in the middle of the bar ($d = 10 \text{ mm}$) have a 10% smaller value of σ_y . The derivative of the plastic multiplier is set to zero at both ends of the bar.

First the case of linear softening is analyzed with the softening modulus $h = -0.1 E$. The internal length $l = 5 \text{ mm}$ is assumed, giving according to eq. (5.9) the gradient constant $g = -l^2 h = 50000 \text{ N}$ and the width of the localization zone $w = 31.4 \text{ mm}$. We begin the comparison with C^0 -continuous penalty-enhanced elements. The left diagram in Fig. 5.2 shows load-displacement paths obtained using elements *L6C* and *L9C* with the (optimal) one-point and two-point Gauss integration, respectively. In the same figure on the right stress-strain relations exhibited by different elements in the 20-element mesh are shown (element 10 lies at the symmetry axis, element 9 to the left etc.). As can be seen for elements 8 and 7, the yield strength is correctly reduced owing to the evolving plastic process in the adjacent elements (nonlocal behaviour). It is also recalled that in the absence of a localization limiter only the weaker element 10 would follow the softening path and the other elements would unload.

Immediate convergence has been observed in the calculations. While the coarse

mesh with 20 linear elements $L6C$ still gives a slightly too stiff response and a disturbed λ distribution (Fig. 5.3), the fine mesh and both meshes for the quadratic $L9C$ element yield identical results. It is observed, that when all the inelastic points in the structure are in the softening regime, the slope of the load-displacement diagram is equal to the analytical value derived in Section 3.1.1.

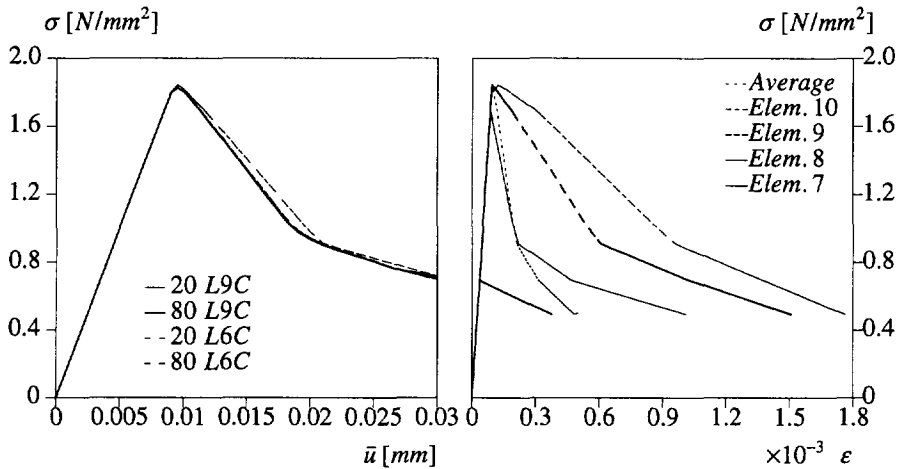


Figure 5.2 Load-displacement diagrams for C^0 one-dimensional elements (left) and stress-strain paths followed by different elements in the middle of the bar discretized with 20 linear elements $L6C$ (right).

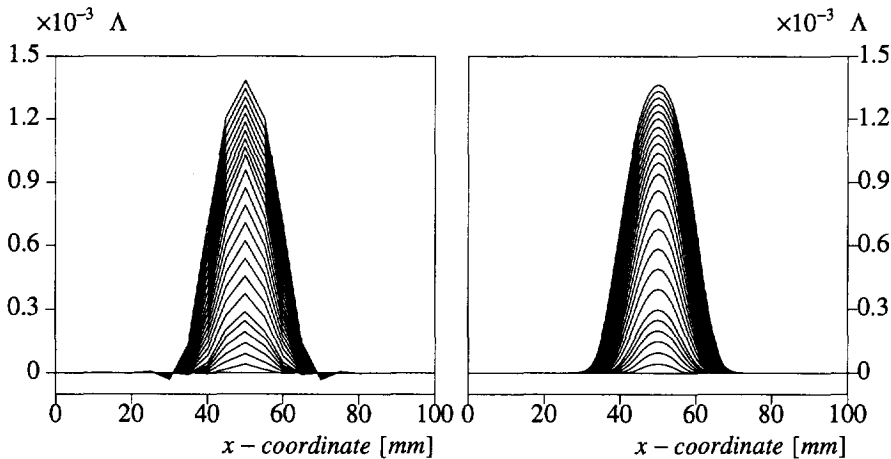


Figure 5.3 Evolution of the plastic strain distribution in the bar for 20 (left) and 80 (right) elements $L6C$.

The calculations are also stable when the strain in the centre elements exits the softening branch ($\kappa > \kappa_0$). The load-displacement diagrams then bend upwards and the

localization zone broadens. This behaviour is a result of the fact that the softening modulus h goes to zero in the centre elements and g is kept constant, so that the internal length l locally increases to infinity.

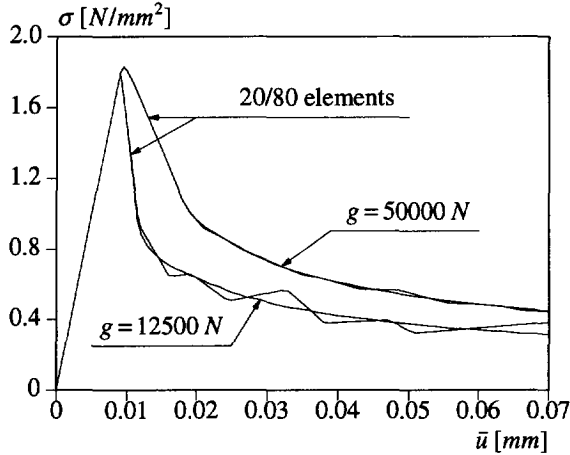


Figure 5.4 Mesh-sensitivity of load-displacement diagrams for linear softening and constant gradient coefficient g (elements $L7G$).

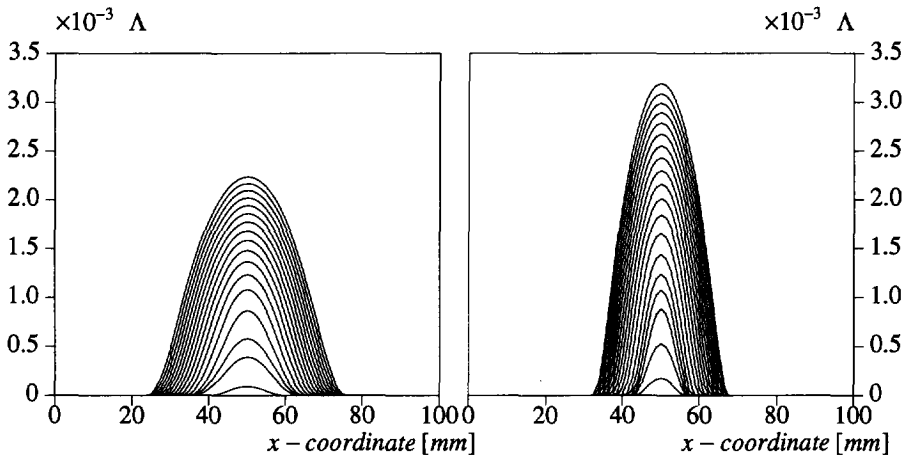


Figure 5.5 Evolution of plastic strains for linear softening and constant gradient variable $g = 50000 N$ (left) and $g = 12500 N$ (right).

Next, we apply the C^1 -continuous elements $L7G$ with quadratic interpolation of the displacement and hermitian interpolation of the plastic multiplier. Two different values of the internal length l are assumed: $l = 5 mm$ (giving $g = 50000 N$ and $w = 31.4 mm$) and $l = 2.5 mm$ ($g = 12500 N$ and $w = 15.7 mm$). Fig. 5.4 shows the load-displacement diagrams for these cases. It is observed, that the C^0 and C^1 element formulations yield similar results. As long as all the points in the structure remain in the softening regime,

the results for the two meshes with 20 and 80 elements are practically the same. This is not the case for the linear-hermitian element $L6G$ (cf. de Borst and Mühlhaus 1992), for which the orders of interpolation are not properly balanced. When in the centre points the softening branch is exited the calculations are stable only if a dense enough discretization is used. In Fig. 5.4 the results for both meshes are similar for the larger regularization coefficient $g = 50000 N$, but for $g = 12500 N$ and the coarse mesh oscillations are observed.

The comparison of the two diagrams in Fig. 5.5 shows that the internal length l (or equivalently the gradient constant g) governs the width of localization zone in the linear softening regime. When for an increasing number of points h equals zero, the width of the localization zone increases.

Next, we adopt a nonlinear softening relation, proposed for cracking in concrete under uniaxial tension (cf. Hordijk 1991). The softening rule $\bar{\sigma}(\kappa)$ has been plotted in Fig. 4.1. The gradient influence is now proportional to the decreasing softening modulus, cf. Section 4.2.3:

$$g(\kappa) = -l^2 \bar{\sigma}'(\kappa), \quad l = \text{constant}. \quad (5.10)$$

Fig. 5.6 shows the results for two values of the ultimate inelastic strain $\kappa_u = 0.003$ and $\kappa_u = 0.006$ (see Fig. 4.1). The same load-displacement diagrams are obtained for both meshes. The error of 10^{-6} in the energy norm is obtained after 2-3 iterations.

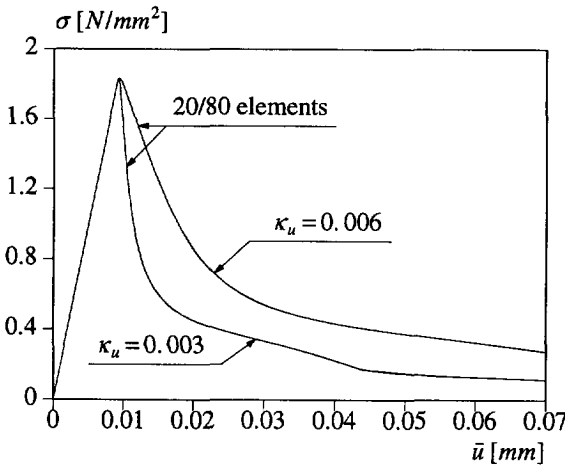


Figure 5.6 Load-displacement diagrams for nonlinear softening and decreasing gradient variable $g(\kappa) = -\bar{\sigma}'(\kappa)l^2$ (elements $L7G$).

Fig. 5.7 shows the distribution of inelastic strains in the bar for the two analyzed cases. In the more brittle case, i.e. $\kappa_u = 0.003$, softening is exhausted in the middle of the bar at the elongation $\bar{u} \approx 0.043$ and therefore the width of the localization zone in the left picture of Fig. 5.7 grows over the analytical value $w = 31.4 \text{ mm}$, which is well predicted for $\kappa_u = 0.006$. For nonlinear softening and gradient dependence proportional to the

decreasing softening modulus, the internal length l clearly also governs the localization band width.

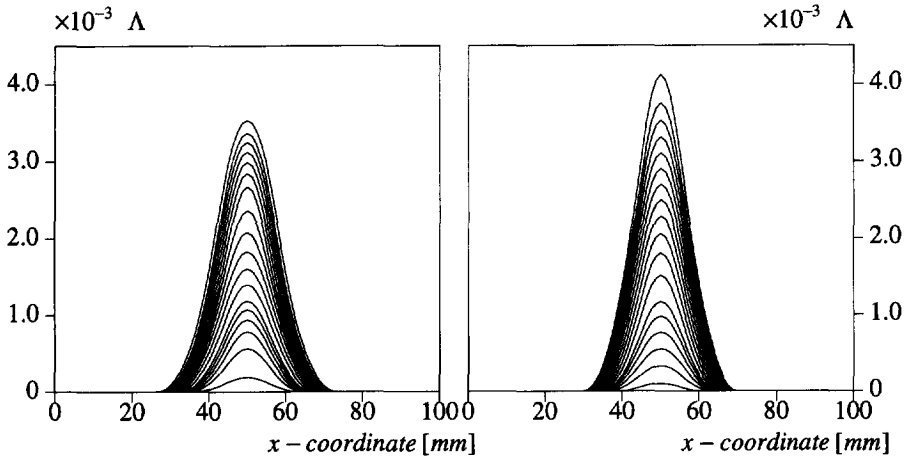


Figure 5.7 Evolution of inelastic strains for nonlinear softening and gradient dependence (left - $\kappa_u = 0.003$, right - $\kappa_u = 0.006$).

5.3 Shear banding examples

5.3.1 Rectangular elements

To demonstrate the potential of two-dimensional elements we consider the biaxially compressed specimen analyzed in Section 2.1.3, in which strain localization into a shear band takes place at the onset of softening. The dimensions of the specimen are $B = 60 \text{ mm}$ and $H = 120 \text{ mm}$. The specimen is placed on a smooth rigid plane and its upper edge is constrained to remain horizontal while a vertical deformation equivalent to a compressive force is applied (see Fig. 2.5). The elastic shear modulus $G = 4000 \text{ N/mm}^2$ and Poisson's ratio $\nu = 0.49$ are assumed. The gradient-dependent Huber-Mises yield function is adopted with the initial yield strength $\sigma_y = 100 \text{ N/mm}^2$, the (linear) softening modulus $h = -0.1 G$ and the gradient constant $g = 3600 \text{ N}$, which corresponds to an internal length scale $l = 3 \text{ mm}$ in case of pure shear.

The left part of Fig. 5.8 shows the load-displacement diagrams for three discretizations with 6×12 , 12×24 and 24×48 eight-noded elements *R32EG* (note that the letter *E* in the element name marks the plane strain version). In the right part of Fig. 5.8 a comparison of load-displacement diagrams for different rectangular elements and the medium mesh (12×24) is given.

It is noted that a homogeneous solution is found in the elastic regime. For an ideal system, homogeneous deformations are also calculated in the unstable regime. The gradient enhancement then has no influence on the solution. To follow an equilibrium path associated with a localized deformation mode we can either detect the bifurcation point and perturb the incremental solution with a scaled eigenvector belonging to the chosen

deformation pattern or include one or more slightly weaker spots in the model (de Borst 1989). In the latter approach, followed here, the bifurcation problem is transferred into a limit problem and the imperfections initiate a localized deformation pattern. In the present calculations an imperfect zone with a 10% reduction of σ_y is introduced in the bottom left-hand corner of the specimen.

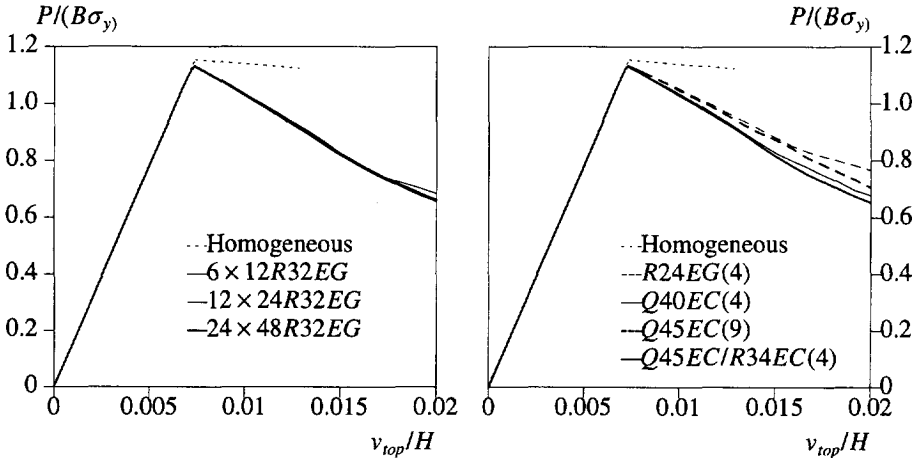


Figure 5.8 Load-displacement diagrams for three discretizations using element $R32EG$ with 2×2 integration (on the left) and comparison of different elements with integration scheme given in brackets (on the right).

For C^1 -elements extra boundary conditions for λ ($\Lambda_n = 0$ and $\Lambda_{xy} = 0$) are introduced on the whole circumference of the specimen. For the most reliable element $R32EG$ fast convergence is observed in the whole analysis, also when the yield strength in the most strained elements goes to zero. The response is practically insensitive to mesh refinement (left part of Fig. 5.8). Element $R34EG$ shows an even faster convergence and results for the coarse mesh are better, but the solution is spoiled by spurious hourglass deformation modes.

A similar performance is found for element $Q45EC$ (right part of Fig. 5.8). For this element, however, the available boundary conditions for Φ_x and Φ_y are not sufficient to assure the correct rank of the $\mathbf{K}_{\lambda\lambda}^c$ matrix, negative pivots are found and spurious modes are observed for the plastic multiplier field. They can be prevented by setting the Λ degrees of freedom to zero on the upper edge of the model. The results are then similar to the two previous elements. Similar convergence and results are also exhibited by the 'heterosis' element $Q43EC$, where the spurious modes must be prevented only for the λ field. Stiffer results and poor convergence are found for element $Q45EC$ with 3×3 numerical integration, which supplies a sufficient rank of the matrices in elastic elements and prevents zero-energy modes, but introduces too many internal constraints and destroys the satisfaction of the yield condition, since optimal sampling points are not used.

The four-noded element *R24EG* also gives stiffer results (Fig. 5.8), but shows good convergence in spite of a poor match between the interpolations. Element *Q20EC* with 2×2 integration locks totally and shows no localization. The eight-noded element *Q40EC* with 2×2 integration gives an acceptable load-deformation response, but quite unexpectedly does not converge well. More explanations concerning the behaviour of the elements can be found in Section 4.4.2.

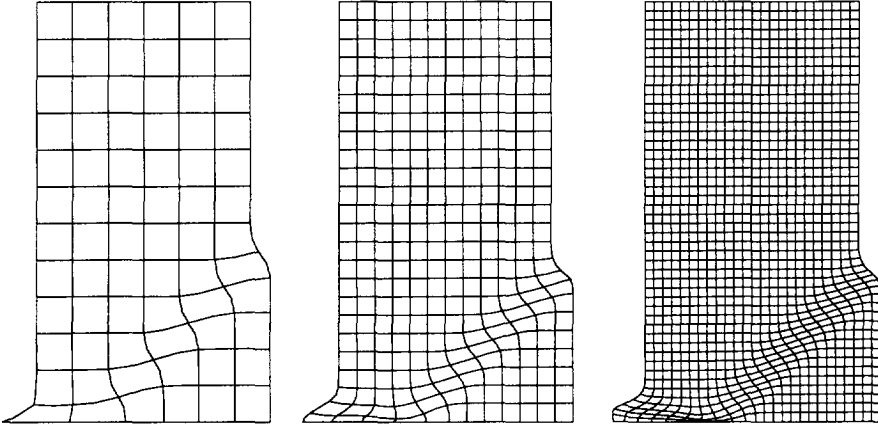


Figure 5.9 Deformation patterns for the three discretizations (element *R32EG*, $v_{top}/H = 0.02$).

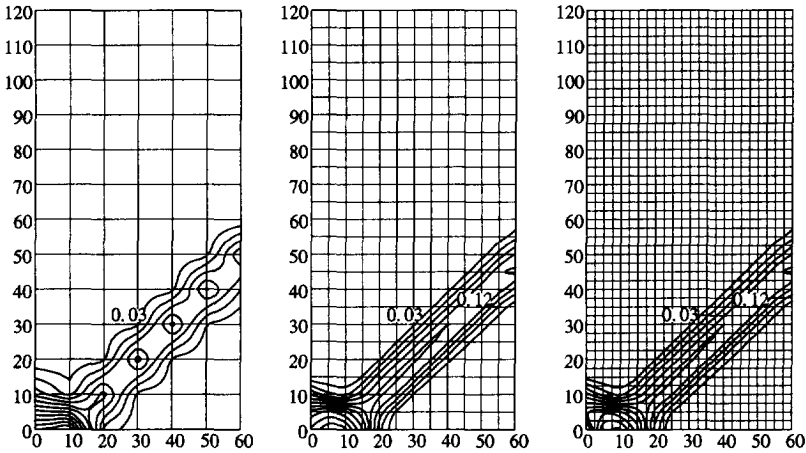


Figure 5.10 Contour plots of the equivalent plastic strain (element *R32EG*, $v_{top}/H = 0.02$).

Fig. 5.9 presents the deformation patterns obtained using element *R32EG*. Notice that the deformations seem large due to the use of a large scaling factor. Fig. 5.10

presents contour lines of equal plastic multiplier values. Both figures show about the same width of the shear band for the three used meshes, especially for the medium and fine meshes. Fig. 5.11 shows the evolution of the equivalent plastic strain field along the vertical symmetry axis of the specimen (element *Q45EC* has been used). For the coarse mesh spurious negative values of λ are visible next to the localization band. For the finer meshes λ profiles are similar to each other and smooth as expected.

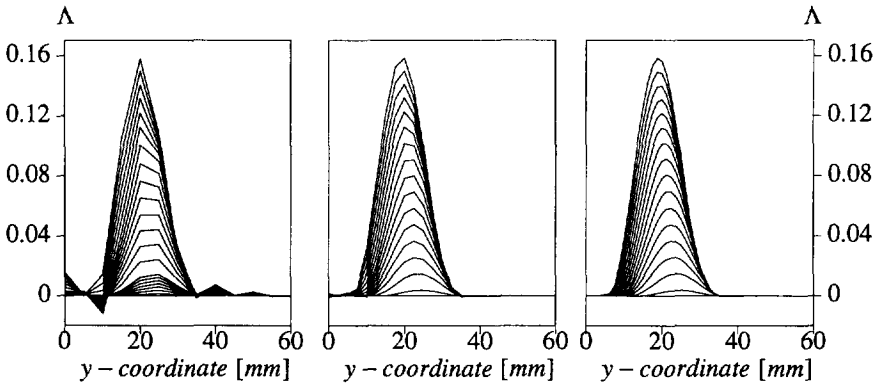


Figure 5.11 Evolution of the equivalent plastic strain along the vertical symmetry axis $x=0$ (from the left: coarse, medium and fine mesh, elements *Q45EC*; only $0 < y < 60$ shown since in the upper part of the specimen $\lambda = 0$).

5.3.2 Triangular elements

The same biaxial compression test has been analyzed using three six-noded triangular elements: the C^1 -element *T30EG*, the non-conforming element *T21EG* and the C^0 penalty-enhanced element *T30EC*. Attention has been focused on the comparison of their sensitivity to mesh alignment. Fig. 5.12 shows the load-displacement diagrams obtained for the discretization $12 \times 24 \times 4$ (crossed diagonal) and $12 \times 24 \times 2$ (with directional bias, i.e. with the elements aligned perpendicularly to the expected direction of a shear band).

For element *T21EG* 3 integration points and boundary conditions $\Lambda_n = 0$ are used (the solution without the boundary conditions is similar, but exhibits a few negative pivots). For element *T30EG* 6 integration points and boundary conditions as for the previous element are employed (if additionally $\Lambda_{xy} = 0$ on the specimen edges, results are similar). For element *T30EC* 3 integration points and boundary conditions for Φ_n (normal to the boundary) are used.

Despite the fact that none of the analyzed triangular elements ensures fast and full convergence, because the used integration stations are not Barlow points (cf. Section 4.4.3), for crossed-diagonal meshes all of them give a similar inclination of the post-peak equilibrium path and prediction of the shear band width and position (see Fig. 5.13). The results are close to the results of element *R32EG*.

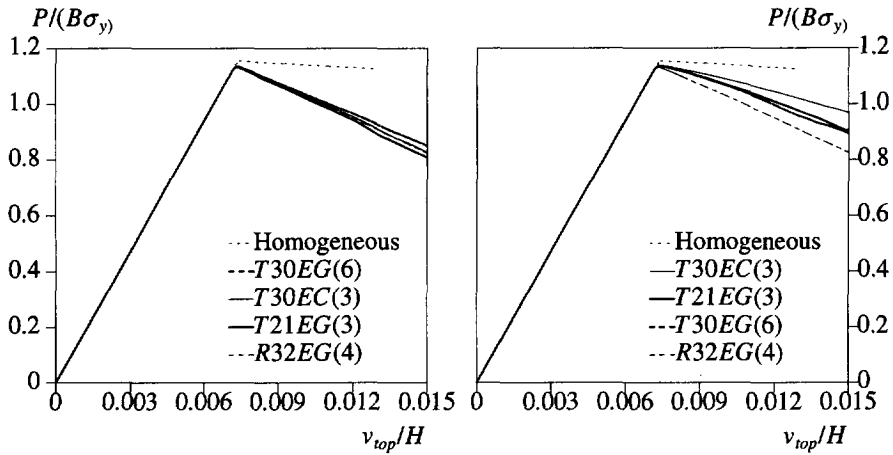


Figure 5.12 Comparison of the behaviour of C^1 and C^0 continuous triangular elements in crossed diagonal meshes (left) and in biased meshes (right).

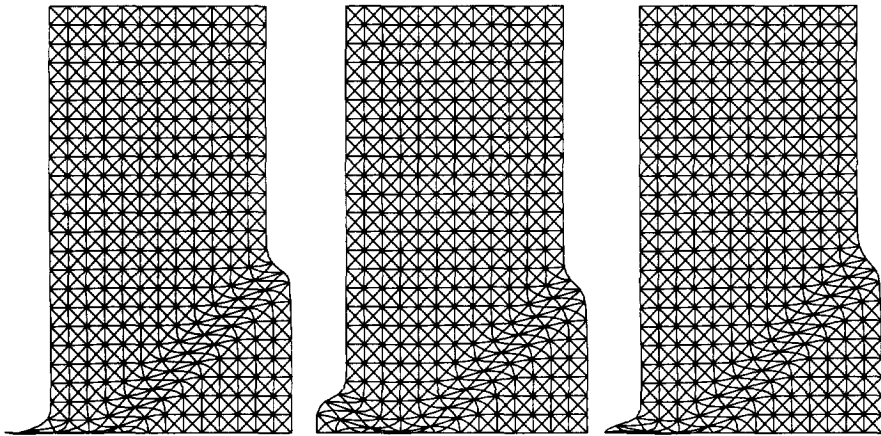


Figure 5.13 Deformation patterns for the crossed diagonal meshes $12 \times 24 \times 4$ ($T21EG$ on the left, $T30EG$ in the middle, $T30EC$ on the right).

Fig. 5.14 presents the deformation patterns obtained for the biased meshes. Though the shear bands now extend from the weaker spot in the bottom left-hand corner of the specimen (compare the results for the classical continuum in Section 2.1.3) the biased mesh makes the response stiffer (cf. Fig. 5.12) especially for the C^0 -element $T30EC$, which also predicts a too broad shear band. For the C^1 -elements the results are acceptable and the slight mesh alignment sensitivity is expected to vanish upon a further mesh refinement.

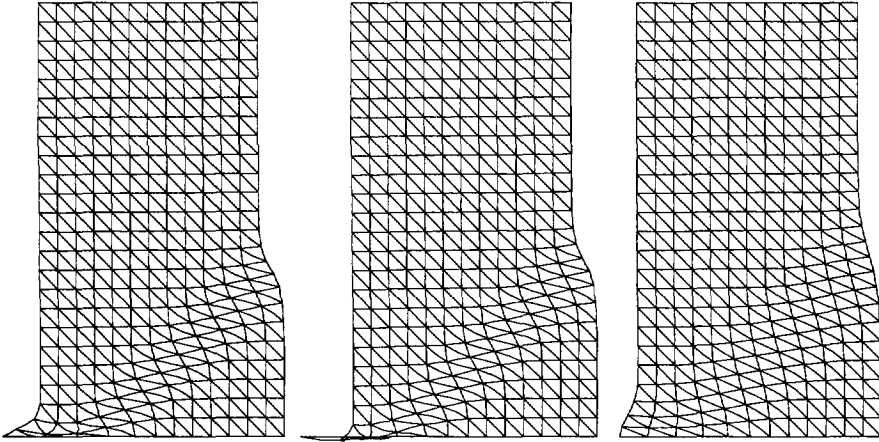


Figure 5.14 Sensitivity to mesh alignment exhibited by the triangular elements (*T21EG* on the left, *T30EG* in the middle, *T30EC* on the right).

5.4 Imperfection sensitivity

The aim of this chapter is to demonstrate the imperfection sensitivity of gradient plasticity predictions. The biaxial compression test and Huber-Mises yield condition are used again. It seems that the influence of imperfections in regularized instability problems depends on the type of loading (static or dynamic) and the used localization limiter (see e.g. Belytschko et al 1992, Wang 1994). We will show that for static problems and gradient plasticity the internal length scale determines the width of the shear band irrespectively of the size of imperfection.

In the previous simulations the size of the imperfect zone, in which a 10% smaller value of the initial yield strength has been assumed, has been kept constant during mesh refinement. Fig. 5.15 shows load-displacement diagrams for the following cases: either only one element at the middle of the specimen is assigned 90% of σ_y (medium and fine mesh), or a weaker zone $25 \times 25 \text{ mm}$ (25 elements) with 95% of σ_y is introduced (medium mesh), or three randomly chosen elements are assigned 95% of σ_y (medium mesh). The diagrams for the medium mesh (12×24 elements) in Fig. 5.15 and the deformation patterns in Fig. 5.16 prove that the results are similar whether the size of the imperfection is larger or smaller than the width of the shear band, determined by the internal length scale. In the absence of a symmetry breaking factor the results for the medium mesh exhibit two shear bands, which is not the most critical solution. For the fine mesh (24×48 elements) and the small imperfection localization in one band through the middle of the specimen is found (Fig. 5.16) after one not fully converged step during the shear band initiation. The load-displacement response is then more brittle, but the width of the band is similar to the medium mesh.

For the specimen with three imperfections different load-displacement diagrams

(Fig. 5.15) are computed depending on the position of the shear band. The diagram for the band running through the middle of the specimen follows the previous results for the fine mesh and the similar band location. For the shear band at the top, accompanied by a highly localized compression zone at the upper edge, the response is the softest.

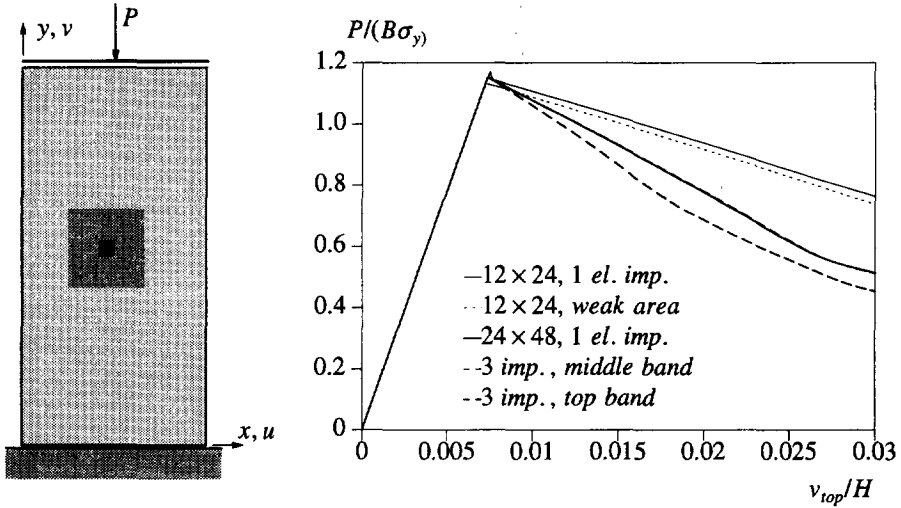


Figure 5.15 Load-displacement diagrams for different imperfection sizes and for the case of three randomly placed imperfections.

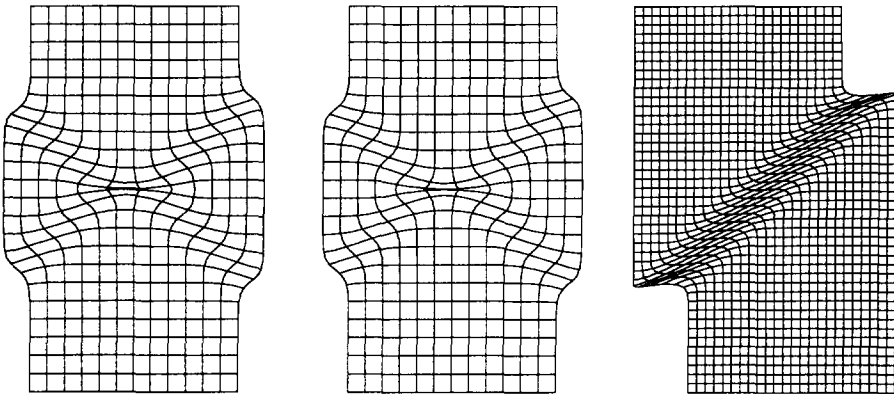


Figure 5.16 Deformation patterns for large weaker area (on the left) and one-element imperfection (middle and right). Element $R32EG$, $v_{top}/H = 0.02$.

Fig. 5.17 shows three contour plots for the case of randomly chosen places of the three imperfections. As can be seen in the left picture three weak spots exist in the specimen. The other two pictures present the distribution of plastic strains obtained for different loading step sizes in the deformation controlled algorithm. It is observed that the shear

band width is the same in both cases.

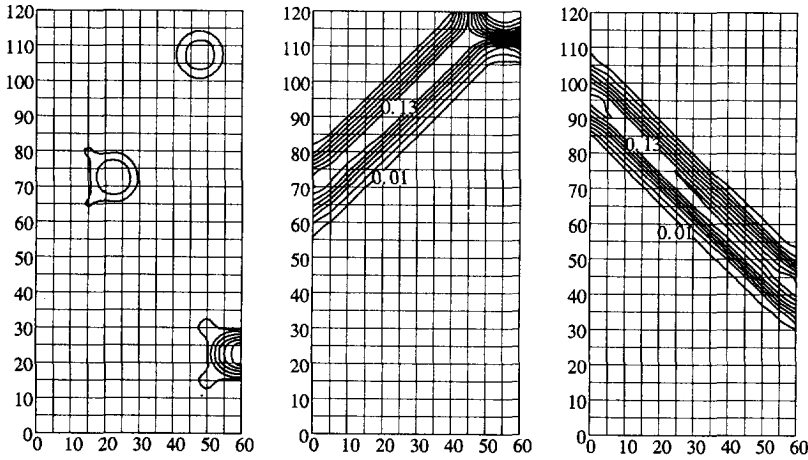


Figure 5.17 Contour plots of the equivalent plastic strain (on the left three small plastic zones caused by imperfections at the peak load, on the right two shear band solutions obtained for different loading step sizes).

We conclude that in the presence of the gradient localization limiter more than one solution is possible (uniqueness of solution is not assured), but all solutions are physically meaningful. The choice of a particular solution depends on the distribution of imperfections, presence of symmetry breaking factors (e.g. boundary conditions) and numerical algorithm (e.g. the step size), but not on the imperfection dimensions.

6. Application to soil instability problems

In this chapter attention is focused on instabilities encountered in geomaterials (cf. de Borst et al 1994₂). The Drucker-Prager gradient plasticity model is used to analyze localized deformations in a biaxially compressed sample and in an embankment under increasing gravity load.

In loose and cemented granular materials like soil, rock and concrete considerable changes of material volume are observed upon loading (Rudnicki and Rice 1975, Vermeer and de Borst 1984). The constitutive equations are strongly pressure-sensitive and the resulting inelastic response is *dilatant* (or contractant). Dependence on the load history plays also an important role. An increase of volume associated with a shear distortion of a material element (shear dilatancy) is a characteristic feature related to the decrease of soil density and strength. The dilatancy angle (which represents a ratio of the plastic volume change and the plastic shear strain) is significantly smaller than the friction angle and the material response is softer as the dilatancy angle decreases. Moreover, experiments show that the normality of the plastic flow direction with respect to the yield surface should not be postulated. The behaviour of geomaterials can be closer reproduced using a non-associated flow rule.

Failure of soil and rock masses under compressive stresses is often accompanied by a sudden transition from a uniform deformation field into a number of localized *shear bands* (de Borst 1986, 1989). They have a small but finite thickness. Within the classical continuum theory, the acoustic tensor singularity condition gives the critical value of the hardening modulus, for which the bifurcation is possible at a given state of stress, and the direction of the strain rate discontinuity plane (Runesson et al 1991). However, a meaningful prediction of the post-bifurcation behaviour is impossible since well-posedness is lost.

The Mohr-Coulomb (cf. Vermeer and de Borst 1984, de Borst 1986) and Drucker-Prager (cf. Rudnicki and Rice 1975) plasticity models include the hydrostatic stress dependence of the yield function and the non-normality of the plastic flow. In the context of the *critical state* models (cf. Gens and Potts 1988) they are able to describe the behaviour of geomaterials in the *supercritical* (softening) regime, but are inadequate in the *subcritical* (hardening) regime, where a cap is necessary to allow for yielding at high confining pressures. However, our aim is not to formulate a complete constitutive model for soil, but rather to examine the gradient plasticity approach to localization in geomaterials. Therefore we will limit our consideration to the non-associated Drucker-Prager model. In accordance with the assumed isotropy, we will adopt constant values of the friction and dilatancy angles and only the cohesion will exhibit softening, attributed to soil overconsolidation.

The loss of material stability may be caused by the cohesion softening or the loss of normality of the plastic flow or a combination of the two effects. It means that localization may be encountered even for a hardening model, if a non-associated flow rule is used (Rudnicki and Rice 1975). A bifurcation into a localized deformation pattern may

also take place prior to the limit load obtained for homogeneous deformations (Vermeer and de Borst 1984). However, the gradient enhancement with $g > 0$, cf. the discussion before eq. (3.24), enlarges the elliptic domain of the governing equations in the post-critical regime and introduces the internal length scale defining the width of the shear bands.

6.1 Drucker-Prager gradient plasticity

Assuming that the hardening/softening behaviour is limited to the cohesion of the material, the Drucker-Prager yield function for gradient-dependent plasticity can be written as follows:

$$F = \sqrt{3J_2} + \alpha p - \beta \bar{c}_g(\kappa, \nabla^2 \kappa), \quad (6.1)$$

where $p = \frac{1}{3}(\sigma_{xx} + \sigma_{yy} + \sigma_{zz})$ is the hydrostatic pressure, α and β are functions of the internal friction angle ϕ :

$$\alpha = \frac{6 \sin \phi}{3 - \sin \phi}, \quad \beta = \frac{6 \cos \phi}{3 - \sin \phi}, \quad (6.2)$$

and \bar{c}_g is a gradient dependent measure of the cohesion. Introducing an auxiliary vector $\Pi = (1/3, 1/3, 0, 1/3)$ and using the matrix \mathbf{P} defined in eq. (5.2) the yield function for the plane strain case takes the form:

$$F = \left(\frac{3}{2} \sigma^T \mathbf{P} \sigma\right)^{1/2} + \alpha \Pi^T \sigma - \beta \bar{c}_g(\kappa, \nabla^2 \kappa). \quad (6.3)$$

The gradient to the yield function equals

$$\mathbf{n} = \frac{\partial F}{\partial \sigma} = \frac{3\mathbf{P}\sigma}{2\left(\frac{3}{2} \sigma^T \mathbf{P} \sigma\right)^{1/2}} + \alpha \Pi. \quad (6.4)$$

For non-associated plasticity we define the plastic potential function and its gradient in a similar way:

$$G = \sqrt{3J_2} + \bar{\alpha} p, \quad (6.5)$$

$$\mathbf{m} = \frac{\partial G}{\partial \sigma} = \frac{3\mathbf{P}\sigma}{2\left(\frac{3}{2} \sigma^T \mathbf{P} \sigma\right)^{1/2}} + \bar{\alpha} \Pi, \quad (6.6)$$

where $\bar{\alpha}$ is a function of the dilatancy angle ψ similar to the definition of α in eq. (6.2). The second derivative of the plastic potential function is equal to the second derivative defined for Huber-Mises plasticity in (5.5), so the algorithmic matrix \mathbf{H} is identical for both criteria. To determine the value of the constant η relating $\dot{\kappa}$ to $\dot{\lambda}$ according to eq. (3.45) we use again the strain-hardening hypothesis. Substitution of the plastic strain rate vector $\dot{\epsilon}^p = \dot{\lambda} \mathbf{m}$ into eq. (5.6), recalling the auxiliary matrix $\mathbf{Q} = \text{diag}[1, 1, 1/2, 1]$ and noting that $\mathbf{PQ} = \mathbf{P}$ and $\mathbf{PQ}\Pi = \mathbf{0}$ give:

$$\dot{\kappa} = \dot{\lambda} \left(1 + \frac{2}{9} \bar{\alpha}^2\right)^{1/2}, \quad (6.7)$$

so that $\eta = \sqrt{1 + 2/9 \bar{\alpha}^2}$. According to the definitions in eqs (3.48) and (3.49) we have:

$$h = \eta\beta \frac{\partial \bar{c}_g}{\partial \kappa}, \quad g = -\eta\beta \frac{\partial \bar{c}_g}{\partial \nabla^2 \kappa}, \quad (6.8)$$

and for linear softening \bar{c}_g can be written as:

$$\bar{c}_g = c_y + \frac{h}{\eta\beta} \kappa - \frac{g}{\eta\beta} \nabla^2 \kappa \quad (6.9)$$

with constant h and g . For nonlinear softening the cohesion changes according to the formula:

$$\bar{c}_g = \bar{c}(\kappa) - \frac{g(\kappa)}{\eta\beta} \nabla^2 \kappa, \quad (6.10)$$

so the softening modulus can be calculated as:

$$h = \eta\beta \bar{c}'(\kappa) - g'(\kappa) \nabla^2 \kappa. \quad (6.11)$$

An important advantage of the Drucker-Prager yield function is its smoothness, since the presence of singular edges on the yield surface poses a difficulty for the gradient plasticity algorithm (for the discussion see Chapter 7.1). In fact, the Drucker-Prager yield surface also possesses a vertex at the cross section with the hydrostatic axis $J_2 = 0$. From eq. (6.1) we can calculate that at the vertex $p = \bar{c}_g \cot\phi$. It is assumed here that the stress points in large triaxial tension, which would fall into the vertex regime $p > \bar{c}_g \cot\phi$, are not admitted.

6.2 Biaxial compression test

6.2.1 Associated flow rule

We will now investigate the standard plane strain biaxial compression test introduced in Section 2.1.3. In Chapter 5 we have used this test in the mesh-sensitivity studies with the Huber-Mises gradient plasticity. Now we allow for some pressure dependence and plastic dilatation by the use of the Drucker-Prager yield function. The adapted material data are as follows: elastic shear modulus $G = 4000 \text{ N/mm}^2$, Poisson's ratio $\nu = 0.49$, initial cohesion $c_y = 50 \text{ N/mm}^2$, linear softening modulus for cohesion $\partial \bar{c} / \partial \kappa = -0.05 G$. Associated plasticity is assumed with the friction and dilatancy angles such, that $\sin \phi = \sin \psi = 0.3$. From eq. (6.7) we have $\eta = \dot{\kappa} / \dot{\lambda} \approx 1.048$. According to eq. (6.8)₁ the value of the hardening modulus is $h \approx -0.111 G$. We assume an internal length $l = 3 \text{ mm}$ and calculate the value of the gradient constant as $g = -l^2 h = 4000 \text{ N}$.

The test configuration has the same dimensions as before: $B = 60 \text{ mm}$ and $H = 120 \text{ mm}$ (Fig. 6.1). We use eight-noded gradient plasticity elements *R32EG* with serendipity interpolation of displacements and hermitian interpolation of plastic strains. The results for three discretizations are compared: 6×12 , 12×24 and 24×48 elements. The support of the specimen is smooth and rigid, the load is applied at the top and all nodes at the top are constrained to have the same vertical displacements. Along all boundaries the derivatives of the plastic multiplier Λ_n and Λ_{xy} are set to zero. To follow the most critical solution with only one shear band, an imperfect zone with 10% smaller

c_y is introduced in the bottom left-hand corner (Fig. 6.1). Calculations are performed under arc-length control.

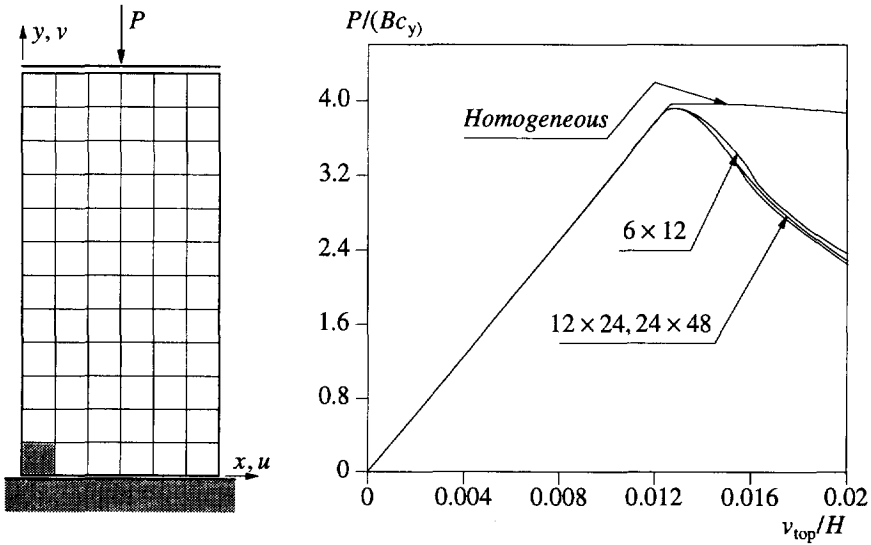


Figure 6.1 Test configuration (with imperfection in the bottom left-hand corner) and load-displacement diagram for the softening Drucker-Prager plasticity ($\sin \phi = \sin \psi = 0.3$).

Fig. 6.1 presents the relative load versus relative displacement diagrams for the case of homogeneous and localized deformation. Fig. 6.2 presents the incremental deformations and Fig. 6.3 contours of equal values of the equivalent plastic strain obtained at the end of calculations.

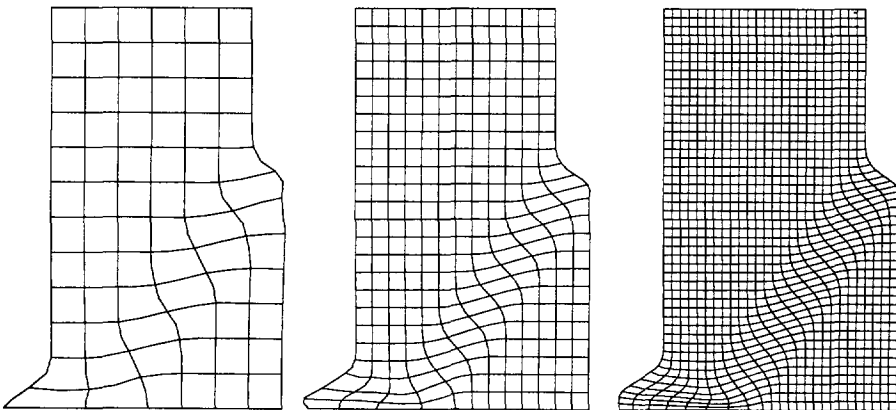


Figure 6.2 Deformation patterns for the three discretizations at $v_{top}/H = 0.02$.

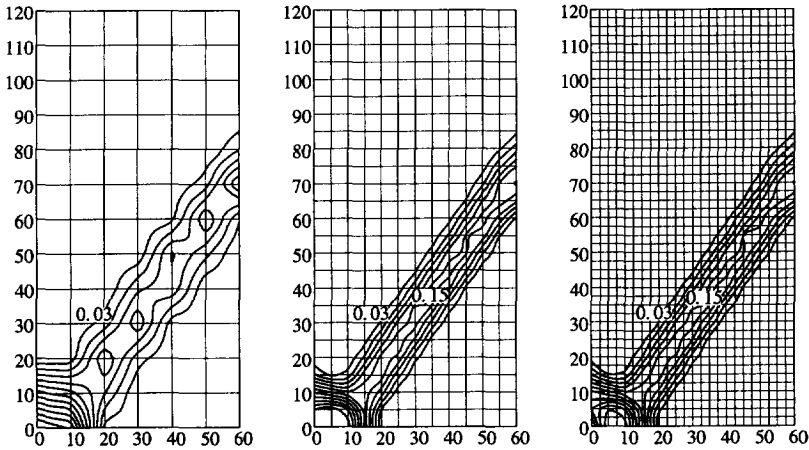


Figure 6.3 Contour plots of the equivalent plastic strain at $v_{\text{top}}/H = 0.02$.

It is observed that the transition from homogeneous to localized deformation takes place at the beginning of the plastic process and that the shear band runs more vertically than for the Huber-Mises plasticity in Chapter 5. The inclination of the band is very close to the critical bifurcation direction calculated analytically: according to Runesson et al (1991), the angle between the vertical axis and the normal to the discontinuity is 56.2° . This is expected since the gradient model is a singular perturbation of the classical continuum (cf. Chapter 3.1). The load-displacement diagrams in Fig. 6.1 exhibit proper convergence to the unique solution and the same convergence is visible in the deformation patterns and contour plots. The convergence is even faster if the nine-noded elements *R34EG* are used (cf. de Borst et al 1993). It is noticed that even though we now analyze a biaxial stress state, the formula $w = 2\pi l$ derived for a one-dimensional case gives a good approximation of the shear band thickness obtained in the numerical simulation.

We next adopt a new set of data and show that a bulging mode can develop in the specimen instead of a shear band. The new material data are: $G = 1000 \text{ N/mm}^2$, $\nu = 0.2$, $c_y = 1 \text{ N/mm}^2$, $\partial \bar{c} / \partial \kappa = -0.025 G$, $\phi = 30^\circ$ ($\sin \phi = 0.5$, $\alpha = 1.2$). We first analyze the case of associated plastic flow, so the dilatancy angle ψ is equal to the friction angle ϕ ($\bar{\alpha} = \alpha$). According to the derivations in the preceding chapter $\eta \approx 1.149$ and the softening modulus $h \approx -0.060 G$. The internal length scale $l = 4 \text{ mm}$ is assumed, so that the gradient constant $g \approx 955 \text{ N}$.

Fig. 6.4 presents load-displacement diagrams for the case of homogeneous deformation, classical continuum model ($l=0$, medium mesh) and gradient plasticity model (all meshes). The significant pressure dependence of the yield function causes the initial stress build-up and hardening behaviour despite the cohesion softening. The whole specimen shows an almost uniform plastic flow (the imperfection causes only a minor disturbance) and a shear band type localization is impossible at the onset of

plastification. This behaviour agrees with the fact that the critical value of the softening modulus calculated analytically for this stress state according to Runesson et al (1991) or Rudnicki and Rice (1975) is much smaller than the value adopted in our calculations.

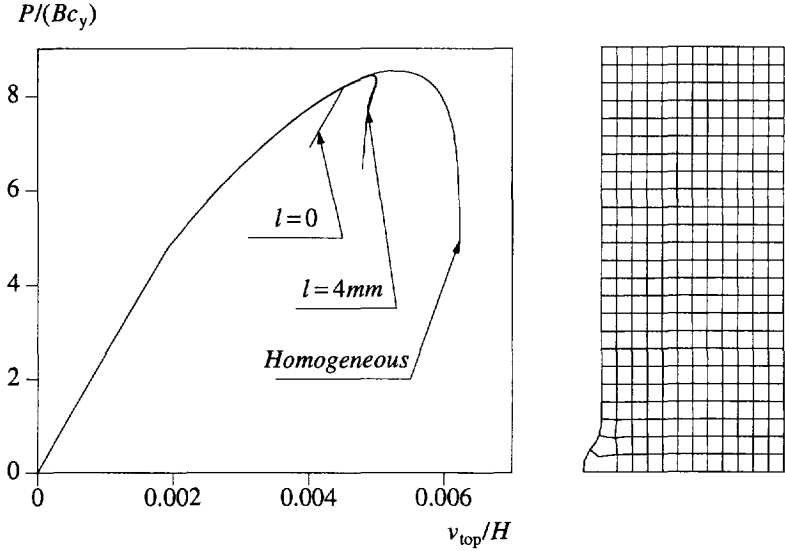


Figure 6.4 Load-displacement diagrams for associated plasticity with the second set of data ($\sin \phi = \sin \psi = 0.5$) and incremental deformations of the gradient-independent model for the medium mesh.

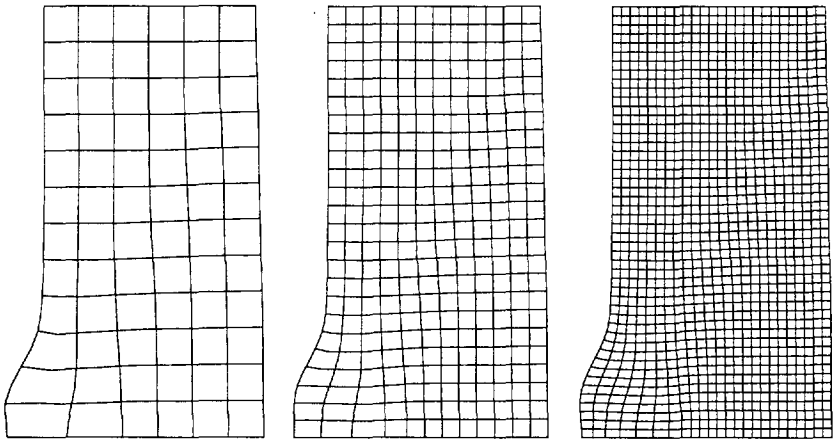


Figure 6.5 Incremental deformations of the gradient-dependent model at $P/(Bc_y) = 7.3$.

At the load level $P/(Bc_y) \approx 8.4$ (and in the absence of gradient dependence even earlier) a bulging localization mode emerges as shown in Figs 6.4-6.5. For the gradient-

independent model ($l=0$) the deformation is trapped in two of the imperfect elements. The deformation patterns obtained for gradient-dependent continuum ($l=4\text{mm}$) show the expected smoothing and distribution of plastic strains outside the imperfect zone. The results for the three meshes are also similar in the post-critical regime.

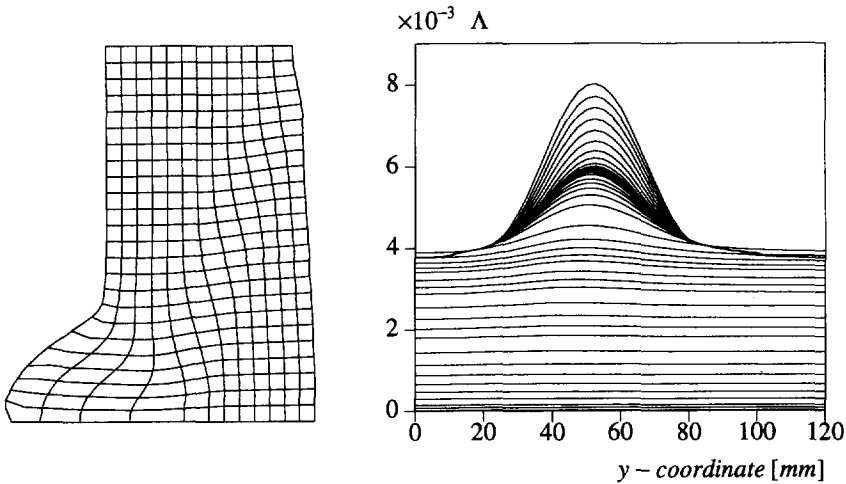


Figure 6.6 Emergence of a shear band in the presence of the bulging localization mode. Incremental displacements of the medium mesh at $P/(Bc_y)=6.4$ (left) and the evolution of the plastic strain distribution along the vertical symmetry axis (right).

During the plastic deformation process the relations between the stress components have changed and the critical value of the softening modulus has increased. At the onset of inhomogeneous deformation the analytical formula (Runesson et al 1991) applied to the numerically determined stress values gives $h_{cr} \approx -0.13 G$, which is still smaller than the input data (shear band formation is impossible). However, it is observed that in the post-critical regime the bulging mode evolves into a shear band mode (Fig. 6.6).

6.2.2 Non-associated flow rule

For real soils the dilatancy angle is considerably smaller than the friction angle. In the previous associated plasticity case the dilatancy has therefore been overestimated. We will now deal with the other limiting case of volume-preserving plastic flow. The test data are the same as in the second part of the previous chapter with the exception of the dilatancy angle ψ , which is now equal to zero. The value of the softening modulus is $h \approx -0.052 G$ and the gradient constant is $g \approx 831 N$. Calculations are performed under displacement control.

Load-displacement curves for the three discretizations are shown in Fig. 6.7 on the left together with the homogeneous and gradient-independent case. As expected, the material response is much softer than in the previous test due to the decrease of the dilatancy angle. On the right the shear band obtained for the standard continuum case using

the medium mesh is plotted. It shows how the gradient-independent finite elements attempt to predict the formation of a discontinuity plane (the shear band width converges to the smallest value permitted by the discretization). For $l=0$ the other meshes would give completely different solutions in the post-critical regime.

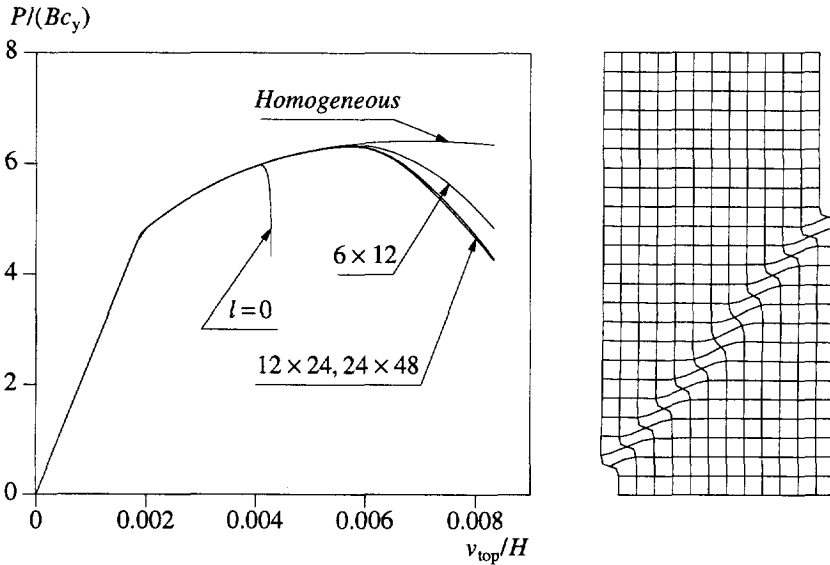


Figure 6.7 Load-displacement diagrams for the non-associated plasticity case and the incremental deformations of the gradient-independent model for the medium mesh.

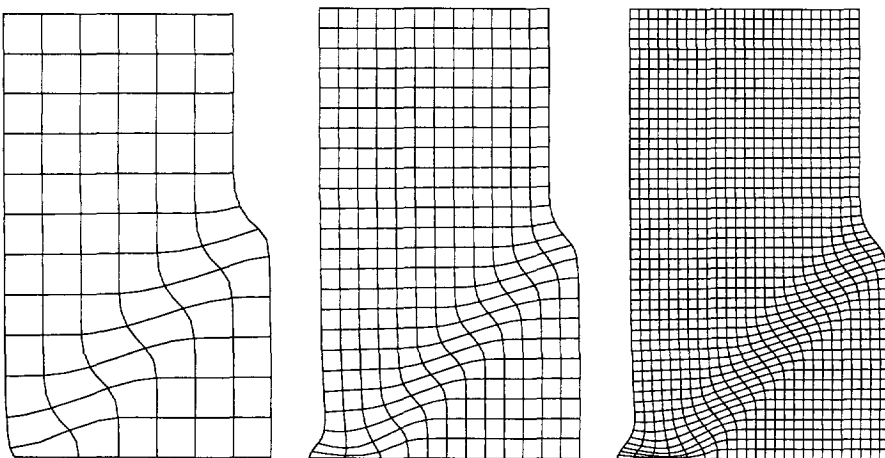


Figure 6.8 Incremental deformations of the gradient-dependent model at $v_{top}/H = 0.0083$.

On the other hand the gradient-dependent model predicts physically acceptable results. Though the response for the coarse mesh is slightly too stiff, it is almost the same for the medium and fine meshes. The shear band width is similar for all meshes (Fig. 6.8) and it is determined by the value of the internal length l .

The non-associated plasticity model results in a less stable behaviour than the associated model. At the onset of plastification the localization is obviously impossible ($h_{cr} \approx -0.427 G$), but at the onset of numerically predicted shear banding the analytical value of the critical hardening modulus is already positive: $h_{cr} \approx 0.03 G$ according to Runesson (1991).

6.3 Slope stability problem

Fig. 6.9 shows two configurations used for the analysis of soil mass stability under an increasing gravity load. On the left we present a slope with an inclination of 45° (cf. Ortiz et al 1987) and on the right a vertical embankment. In both cases the lower edge is fixed and the right edge is supported in the horizontal direction.

The material data are based on Ortiz et al (1987): Young's modulus $E = 2 \cdot 10^8 N/m^2$, Poisson's ratio $\nu = 0.25$, initial cohesion $c_y = 2000 N/m^2$, friction angle $\phi = 20^\circ$, dilatancy angle $\psi = 10^\circ$. The soil density $\rho = 1000 kg/m^3$ is adopted. The linear softening rate for cohesion is $\partial \bar{c} / \partial \kappa = -0.01 G$. Assuming the strain hardening hypothesis from eq. (5.6) we obtain $\eta = \dot{\kappa} / \dot{\lambda} \approx 1.015$ and the softening modulus equals $h \approx -0.060 G$ according to eq. (6.8)₁. Two internal length scales $l = 0.02 m$ and $l = 0.04 m$ are considered (the gradient constants are $g \approx 688 N$ and $g \approx 2752 N$, respectively).

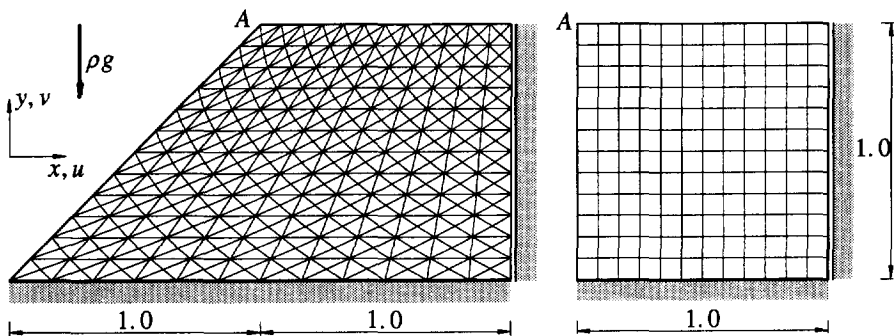


Figure 6.9. Inclined and vertical embankment models (dimensions in m).

For the first configuration we use two crossed-diagonal meshes with $12 \times 12 \times 4$ and $24 \times 24 \times 4$ six-noded triangles $T21EG$ (quadratic interpolation of displacements, non-conforming interpolation of plastic strains, 3 integration points). For the second configuration we use three discretizations with 12×12 , 24×24 and 48×48 eight-noded elements $R32EG$ (serendipity interpolation of displacements, hermitian interpolation of plastic strains, 2×2 integration scheme). Along all the boundaries the normal derivatives of the

plastic multiplier Λ_n (and for element *R32EG* also the mixed derivative Λ_{xy}) are set to zero. The calculations are performed under arc-length or single displacement control. In the latter case the vertical displacement of point A is the controlling parameter (cf. Fig. 6.9).

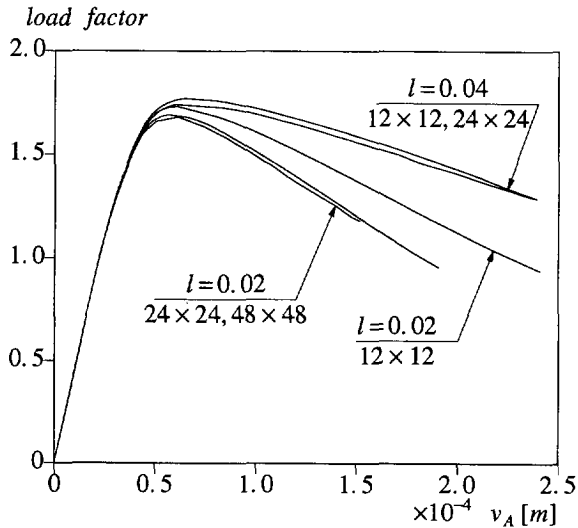


Figure 6.10. Mesh sensitivity of load-displacement diagrams for the vertical embankment and gradient plasticity elements *R32EG*.

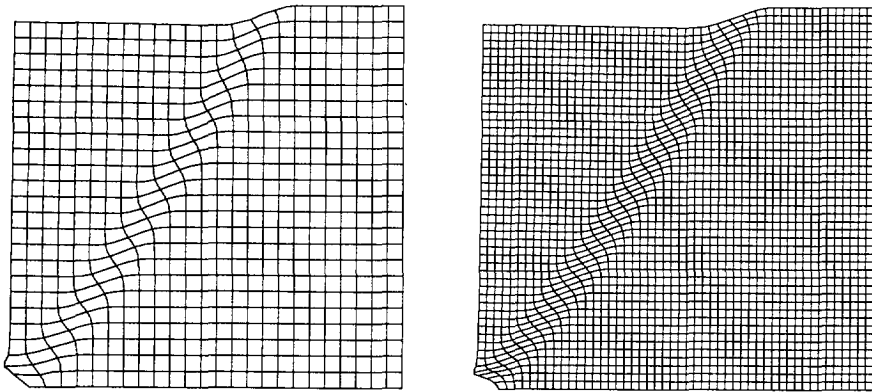


Figure 6.11. Incremental deformation patterns for the medium and fine mesh ($l=0.02m$).

An attempt to use the quadrilateral elements *Q45EC* was not successful. While the use of 2×2 integration resulted in many negative pivots and spurious zero-energy modes for the plastic multiplier field, 3×3 integration caused locking of the solution and no

localization was observed.

We begin the discussion with the vertical embankment. Fig. 6.10 presents the calculated relations between the gravity load factor and the vertical displacement of point A obtained using the Drucker-Prager gradient plasticity model. When the gravity load reaches the level 0.6 the first plastic points occur in the bottom left-hand corner of the embankment. A shear band then gradually extends towards the upper edge and a softening response follows. Fig. 6.11 presents the incremental displacements at the final load level for the smaller internal length $l=0.02m$ ($g=688 N$). It is observed that the medium and fine mesh produce similar results. A too stiff response is found in Fig. 6.10 for the coarse mesh (12×12 elements). The shear band width defined by the assumed internal length is close to the smallest shear band size that can be reproduced by this mesh. Therefore the representation is insufficient, while for the larger internal length $l=0.04m$ ($g=2752 N$) the coarse and medium meshes give already similar results. Fig. 6.12 illustrates the dependence of the shear band width w on the assumed value of the internal length l . As for the biaxial compression test a good correspondence is found with the analytical formula $w=2\pi l$ derived for a one-dimensional case in Section 3.1.1.

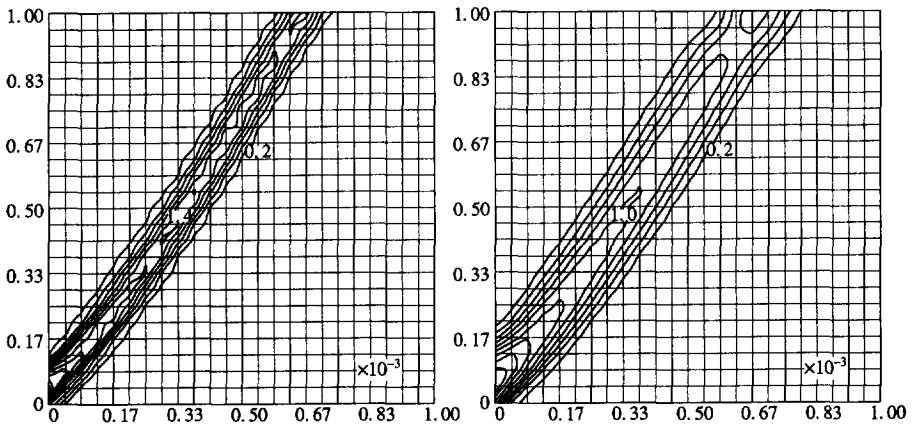


Figure 6.12. Contour plots of equivalent plastic strain for $l=0.02$ (left) and $l=0.04$ (right).

Next, we analyze the stability of the slope in Fig. 6.9. In addition to the linear softening case we consider the ideal plasticity case $\partial \bar{c} / \partial \kappa = 0$. In the gradient plasticity calculations the coefficient $g=2752 N$ is used. Fig. 6.13 presents the load-displacement diagrams. With the increase of the self-weight (at the load factor value 1.8) the compressed soil mass starts to plastify at the bottom of the embankment. The plastic zone then gradually expands upwards and at the peak load a shear band forms, along which a part of the soil mass slides down.

Calculations for the classical softening plasticity case fail soon after the formation of the shear band. The gradient plasticity algorithm gives a more stable behaviour even though we employ the non-conforming triangular elements $T21EG$ (which does not

fulfil the robustness requirements, see Section 4.4.3). The peak load is higher and the response is more ductile when the gradient contribution is included. The results for both analyzed meshes are close, but not the same (Fig. 6.13).

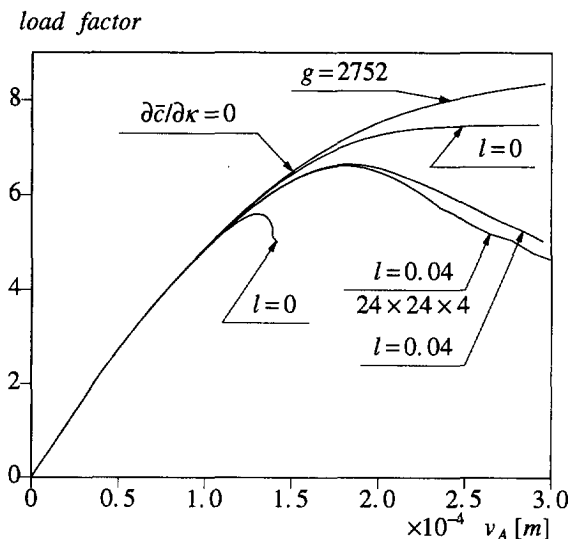


Figure 6.13. Classical versus gradient plasticity solutions for the slope stability problem in terms of gravity load factor and vertical displacement at point A.

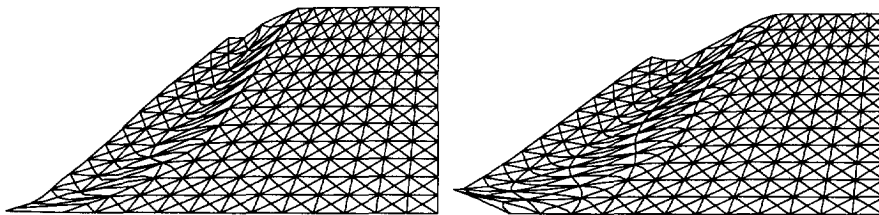


Figure 6.14. Incremental deformation patterns for classical elements ($l=0.0$) and gradient plasticity triangles ($l=0.04$).

Fig. 6.14 presents the final incremental deformations of the $12 \times 12 \times 4$ element mesh for the classical and gradient plasticity cases. Fig. 6.15 shows the deformations of the finest mesh. The expected smoothing effect is observed and the curved shear band has the width of several elements. Fig. 6.16 compares the contour plots of the equivalent plastic strain obtained for the two analyzed discretizations. The strains are slightly more localized for the fine mesh, but the shear band width $w \approx 0.25m$ is well reproduced.

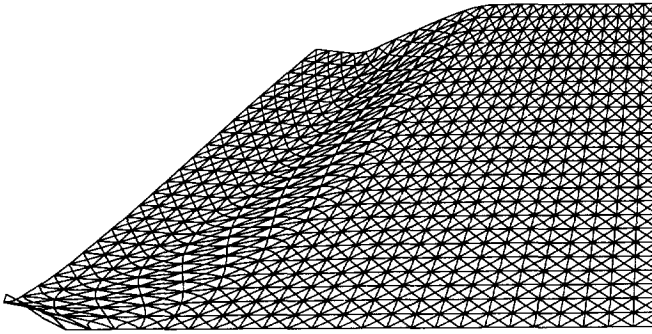


Figure 6.15. Incremental deformation pattern for the finest mesh ($24 \times 24 \times 4$ elements $T21EG$) and $l = 0.04$.

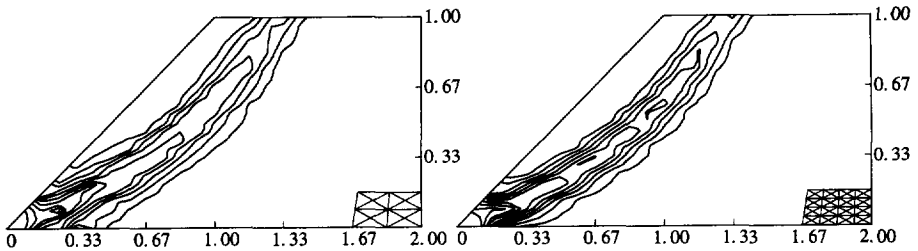


Figure 6.16. Contour plots of equivalent plastic strain for two discretizations ($l = 0.04$).

For the ideal plasticity case the gradient dependence produces an increased load carrying capacity (Fig. 6.13) and a broader shear band is observed (Fig. 6.17). In fact, the relation between the coefficient g , which scales the gradient influence, and the internal length l (hence also the shear band width) is not determined in this case, which corresponds to the gradual increase of the shear band width, observed in the incremental solution.

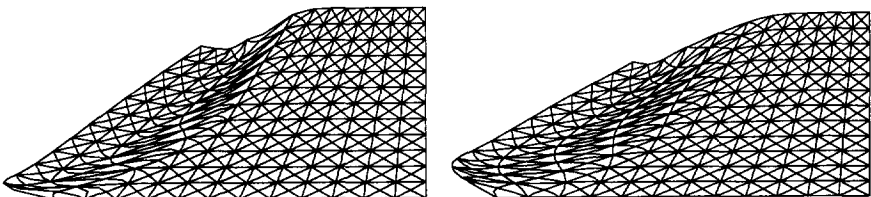


Figure 6.17. Incremental deformations at $v_A = 3 \times 10^{-4} \text{ mm}$ for the ideal plasticity case: $g = 0$ on the left, $g \approx 2752 \text{ N}$ on the right.

7. Application to concrete fracture

As mentioned in the introduction, it is important to assess the ductility of a concrete structure for safety reasons. Some components of the structure may already fail, while no danger of the overall collapse exists. These components exhibit a residual strength that is often neglected in safe, but uneconomic design. Therefore there is a need for more reliable and robust analysis methods that can predict the whole failure process.

The state of the art in computational modelling of concrete has been presented recently during the EURO-C Conference in Innsbruck. For time- and temperature-independent behaviour, an evaluation of the existing cracking and plasticity models (de Borst et al 1994, Willam et al 1994) and continuum damage models (Pijaudier-Cabot et al 1994) has been given. Special emphasis has been put on the cracking processes that govern the failure of concrete and on the formulation of regularization methods for this type of localization.

We have stated in Chapter 2.1 that, in order to explain the fracture of concrete, it is necessary to look at the behaviour at the meso-level (van Mier 1984). We then observe the evolution of microcracks, interaction between mortar and aggregate and formation of macrocracks. There exist computational models of concrete, in which the heterogeneity of the material is included. Two-phase composite models with realistic constitutive relations for the cement matrix and the interfaces between the matrix and the aggregate grains have been formulated and implemented in the finite element method (e.g. Roelfstra 1989, Vonk 1992, Stankowski et al 1992). A lattice model, in which the fracture process zone is discretized by a dense mesh of beam elements having stochastically varying properties, has also been developed (Schlangen 1993). These models have been successfully applied in the numerical verification of concrete fracture experiments, but they require complex mesh generation procedures and/or gradual changes of element topology to follow the complex cracking processes (formation, propagation and bridging).

In this thesis we focus on phenomenological modelling, in which the meso-scale effects are incorporated in a macroscopic constitutive model via the gradient dependence. For simplicity we have accepted the strong assumptions of isotropy and homogenized continuum. We limit our consideration to the behaviour of concrete in plane stress tension and tension-shear.

In the presence of localization the stress-strain relation is only a nominal property and structural effects have to be reflected. In fact, the distribution of heterogeneities in concrete and hence the macroscopic material characteristics have a stochastic character. Their random distribution should be considered in realistic modelling (cf. Carmeliet 1992, Schlangen 1993). However, it has been shown in the context of concrete fracture, that the deterministic size effect - due to the release of the stored elastic energy - is much more important than the probabilistic size effect (due to the randomness of the material strength, cf. Bažant 1992).

In this work the stochastic aspects are neglected. In contradiction to the classical

plasticity models we are capable of reproducing the deterministic size effect since the length parameter (internal length scale) is included in the theory. A direct measurement of the characteristic length for concrete is however not possible and it is interpreted via the width of the fracture zone defined in eq. (2.51), which is related to the maximum aggregate size (Pijaudier-Cabot and Bažant 1988).

Though plasticity is a more natural constitutive description for metals and soils, it is possible to model within its framework most of characteristic features of quasi-brittle (cementitious) materials under monotonic loading conditions (Feenstra 1993). The incapability of reproducing the elastic stiffness degradation cannot be accepted for cyclic loading, for which a damage theory (see e.g. Pijaudier-Cabot et al 1994) or a plastic-fracturing model (see e.g. Maier and Hueckel 1979, Chen and Han 1988) is necessary. It is also noted that the isotropic softening plasticity model is not optimal for concrete cracking (cf. Feenstra 1993), since in reality the emergence of a crack does not reduce the local material stiffness in all directions, but only in the direction perpendicular to the crack. However, since we focus attention on the examination of the gradient regularization and its finite element implementation, we accept those limitations.

7.1 Vertex-enhanced Rankine fracture function

The maximum principal stress criterion, adopted further as a condition of continuum fracture, is formulated here for the plane stress case. The Rankine yield function can be written in the following form:

$$F = \sigma_1 - \bar{\sigma}_g(\kappa, \nabla^2 \kappa), \quad (7.1)$$

where σ_1 is the maximum principal stress

$$\sigma_1 = \frac{1}{2}(\sigma_x + \sigma_y) + \frac{1}{2}\sqrt{(\sigma_x - \sigma_y)^2 + 4\sigma_{xy}^2} \quad (7.2)$$

and $\bar{\sigma}_g$ is the gradient dependent yield strength. Introducing an auxiliary matrix \mathbf{P}

$$\mathbf{P} = \begin{bmatrix} 1/2 & -1/2 & 0 \\ -1/2 & 1/2 & 0 \\ 0 & 0 & 2 \end{bmatrix} \quad (7.3)$$

and an auxiliary vector $\mathbf{\Pi} = (1, 1, 0)$, the yield function can be written as:

$$F = \left(\frac{1}{2} \boldsymbol{\sigma}^T \mathbf{P} \boldsymbol{\sigma}\right)^{1/2} + \frac{1}{2} \mathbf{\Pi}^T \boldsymbol{\sigma} - \bar{\sigma}_g(\kappa, \nabla^2 \kappa). \quad (7.4)$$

The gradient to the yield function equals

$$\mathbf{n} = \frac{1}{2} \left[\frac{\mathbf{P} \boldsymbol{\sigma}}{\left(\frac{1}{2} \boldsymbol{\sigma}^T \mathbf{P} \boldsymbol{\sigma}\right)^{1/2}} + \mathbf{\Pi} \right] = \frac{1}{2\psi_R} \begin{bmatrix} \sigma_x - \sigma_y \\ \sigma_y - \sigma_x \\ 4\sigma_{xy} \end{bmatrix} + \begin{bmatrix} 1/2 \\ 1/2 \\ 0 \end{bmatrix}, \quad (7.5)$$

with

$$\psi_R = \sqrt{(\sigma_x - \sigma_y)^2 + 4\sigma_{xy}^2}. \quad (7.6)$$

The second derivative of the yield function is obtained as:

$$\frac{\partial^2 F}{\partial \sigma^2} = \frac{1}{\sqrt{2}} \frac{\sigma^T \mathbf{P} \sigma \mathbf{P} - \mathbf{P} \sigma \sigma^T \mathbf{P}}{(\sigma^T \mathbf{P} \sigma)^{3/2}} \quad (7.7)$$

For this yield criterion the following definition of the equivalent plastic strain rate is proposed:

$$\dot{\kappa} = |\dot{\varepsilon}_1^p|, \quad (7.8)$$

where $\dot{\varepsilon}_1^p$ is the maximum principal plastic strain rate:

$$\dot{\varepsilon}_1^p = \frac{1}{2} (\dot{\varepsilon}_x^p + \dot{\varepsilon}_y^p) + \frac{1}{2} [(\dot{\varepsilon}_x^p - \dot{\varepsilon}_y^p)^2 + (\dot{\gamma}_{xy}^p)^2]^{1/2}. \quad (7.9)$$

Using an auxiliary matrix \mathbf{R} similar to \mathbf{P} but with the coefficient $R_{33} = 1/2$, we can write:

$$\dot{\varepsilon}_1^p = \left(\frac{1}{2} \dot{\varepsilon}^{pT} \mathbf{R} \dot{\varepsilon}^p \right)^{1/2} + \frac{1}{2} \Pi^T \dot{\varepsilon}^p. \quad (7.10)$$

Substitution of the associated flow rule $\dot{\varepsilon}^p = \dot{\lambda} \mathbf{n}$ into eq. (7.10) gives:

$$\dot{\varepsilon}_1^p = \dot{\lambda}, \quad (7.11)$$

since $\mathbf{P} \mathbf{R} \mathbf{P} = \mathbf{P}$, $\mathbf{P} \mathbf{R} \Pi = \mathbf{0}$, $\Pi^T \mathbf{R} = \mathbf{0}$ and $\Pi^T \mathbf{P} = \mathbf{0}$. We assume that the Rankine yield criterion is activated only when σ_1 is positive. Consequently $\dot{\varepsilon}_1^p$ is positive and $\dot{\kappa} = \dot{\lambda}$ ($\eta = 1$).

A similar form of the yield criterion can be assumed for plane strain situations provided we assure that $\sigma_3 = \sigma_z < \bar{\sigma}_g$ (or σ_y), which means that cracking is admitted only in planes parallel to the z -axis.

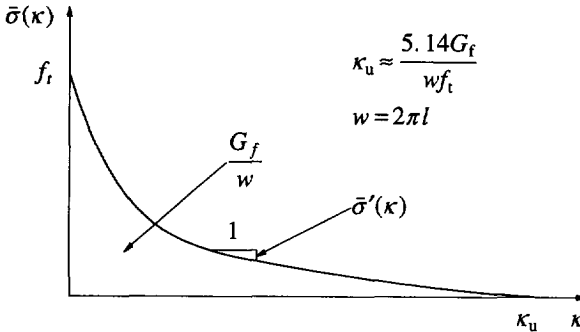


Figure 7.1 Nonlinear softening rule for concrete Mode-I fracture (cf. Hordijk 1991).

The general form of the yield strength $\bar{\sigma}_g$ has been given in eq. (4.69). The following softening function, based on experiments of Cornelissen, Hordijk and Reinhardt (Hordijk 1991), will be used in the applications to concrete fracture problems:

$$\bar{\sigma}(\kappa) = f_t \left\{ \left[1 + \left(c_1 \frac{\kappa}{\kappa_u} \right)^3 \right] \exp\left(-c_2 \frac{\kappa}{\kappa_u}\right) - \frac{\kappa}{\kappa_u} (1 + c_1^3) \exp(-c_2) \right\}, \quad (7.12)$$

where $c_1 = 3.0$, $c_2 = 6.93$, f_t is the uniaxial tensile strength and κ_u is the ultimate value of equivalent fracture strain. The function, formulated originally in the context of discrete cracking, has been adapted here to the continuum format and its relation to the

fracture energy G_f is presented in Fig. 7.1. The relation between the crack band width w and the internal length scale l is assumed to be similar to the uniaxial analytical solution in Section 3.1.1. Moreover, the gradual failure of crack grain bridges which produce the residual carrying capacity of concrete (van Mier 1991) suggests that the gradient influence should decrease with the increase of the accumulated fracture strain. This leads to the softening law in the form derived in eq. (4.72):

$$\bar{\sigma}_g(\kappa, \nabla^2 \kappa) = \bar{\sigma}(\kappa) + l^2 \bar{\sigma}'(\kappa) \nabla^2 \kappa. \quad (7.13)$$

The Rankine yield surface for plane stress problems, presented in Fig. 7.2 in the $(\sigma_x, \sigma_y, \sigma_{xy})$ space, possesses a vertex $\sigma_v = (\bar{\sigma}, \bar{\sigma}, 0)$.

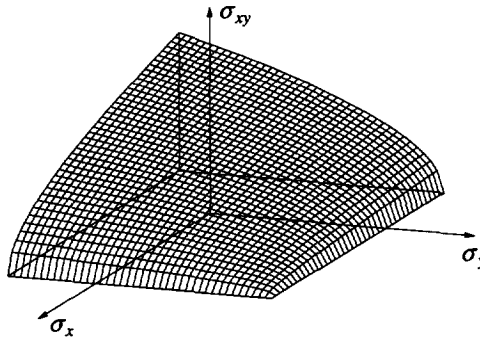


Figure 7.2 Rankine yield surface in the $(\sigma_x, \sigma_y, \sigma_{xy})$ space.

For classical plasticity algorithms the presence of vertices in yield functions involves some extra difficulties (de Borst 1987, Simo et al 1988). Each smooth part of the yield function can first be redefined as a separate function (for instance $F_{(1)}$ and $F_{(2)}$) and then Koiter's generalization can be applied:

$$\Delta \epsilon^p = \Delta \lambda_{(1)} \frac{\partial F_{(1)}}{\partial \sigma} + \Delta \lambda_{(2)} \frac{\partial F_{(2)}}{\partial \sigma}, \quad (7.14)$$

where $\Delta \lambda_{(1)}$ and $\Delta \lambda_{(2)}$ are the respective plastic multipliers. If a stress point in the vertex regime is found, the stress state can be returned to the vertex, which is the correct solution (cf. Fig. 7.3), according to the formula:

$$\sigma_v = \sigma_0 + \mathbf{D}^e \Delta \epsilon - \mathbf{D}^e \Delta \epsilon^p = \sigma_t - \Delta \sigma^p. \quad (7.15)$$

Knowing the vertex position σ_v , it is also possible to reverse the sequence of calculations. First we determine the increment of plastic strains $\Delta \epsilon^p$ as:

$$\Delta \epsilon^p = (\mathbf{D}^e)^{-1} \Delta \sigma^p = (\mathbf{D}^e)^{-1} (\sigma_t - \sigma_v) \quad (7.16)$$

and then we calculate

$$\Delta \epsilon^e = \Delta \epsilon - \Delta \epsilon^p, \quad \Delta \sigma = \sigma_v - \sigma_0 = \mathbf{D}^e \Delta \epsilon^e. \quad (7.17)$$

Alternatively we first calculate the elastic strain increment $\Delta \epsilon^e$ as:

$$\Delta \boldsymbol{\varepsilon}^e = (\mathbf{D}^e)^{-1} \Delta \boldsymbol{\sigma} = (\mathbf{D}^e)^{-1} (\boldsymbol{\sigma}_v - \boldsymbol{\sigma}_0) \quad (7.18)$$

and then the plastic strain increment $\Delta \boldsymbol{\varepsilon}^p$:

$$\Delta \boldsymbol{\varepsilon}^p = \Delta \boldsymbol{\varepsilon} - \Delta \boldsymbol{\varepsilon}^e. \quad (7.19)$$

Iterations at the point level are necessary to obtain an agreement between the stress increments and the position of the vertex, which is a function of the hardening parameter.

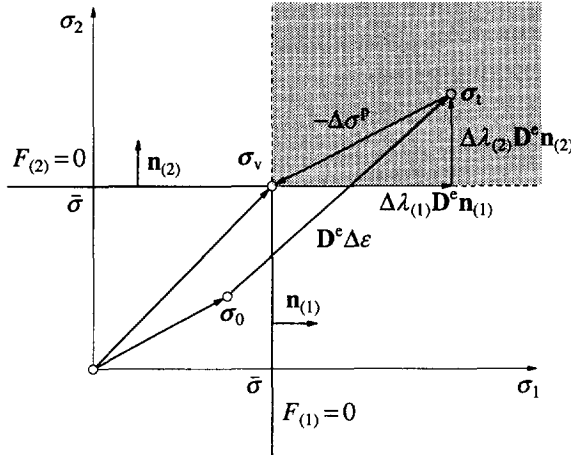


Figure 7.3 Classical return to the vertex in two-dimensional principal stress space.

The situation is different if, as in gradient plasticity algorithm, the plastic multiplier is discretized and the yield condition is fulfilled in a weak sense. A possible, but inefficient solution (following the Koiter's strategy) is to include the discretization of two plastic multipliers $\lambda_{(1)}$ and $\lambda_{(2)}$ in the element formulation and penalize the latter to zero, unless the vertex regime is entered. The second approach, described below, is to apply a smooth approximation of the Rankine yield function. In the next section the original function is smoothed in the neighbourhood of the vertex and in Section 7.1.2 the Drucker-Prager yield function is used for the same purpose.

7.1.1 Vertex smoothing approach

The vertex regime is usually entered from a plastic state, for which $\sigma_2 < \bar{\sigma}$, but in any case there is only one segment of the yield function $F = F_{(1)}$ active and the return mapping is governed by the vector $\mathbf{n} = \mathbf{n}_{(1)}$ (left part of Fig. 7.4). As a result the stress state after the mapping is incorrect, because $\sigma_2 > \bar{\sigma}$.

For vertex smoothing we develop a family of yield functions in the two-dimensional principal stress space (right part of Fig. 7.4), tangential to the Rankine function in the points $(0, \bar{\sigma})$ and $(\bar{\sigma}, 0)$:

$$F_m = (\sigma_1^m + \sigma_2^m)^{1/m} - \bar{\sigma} = 0. \quad (7.20)$$

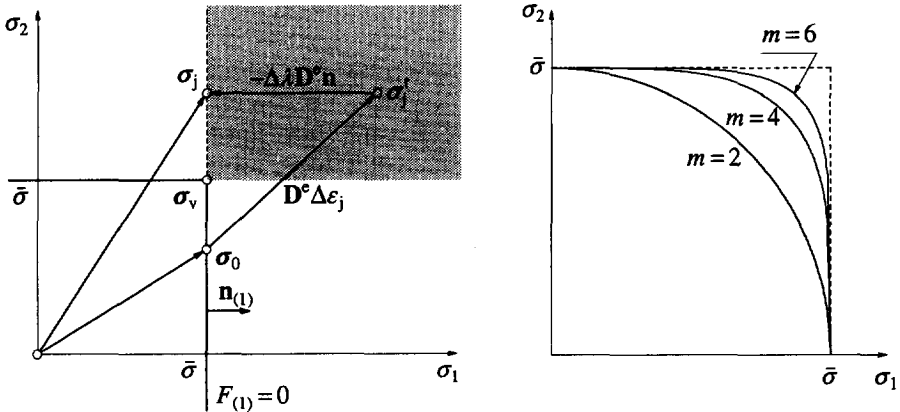


Figure 7.4 Incapability of returning to the vertex in gradient plasticity algorithm (left) and smoothing functions in tension-tension regime (right).

However, these yield surfaces are not compatible with the Rankine yield surface in the $(\sigma_x, \sigma_y, \sigma_{xy})$ space (cf. Fig. 7.2). For example the simple $F_s = F_2$ function, which is a circle in the principal stress space:

$$F_s = (\sigma_1^2 + \sigma_2^2)^{1/2} - \bar{\sigma} = (\sigma_x^2 + \sigma_y^2 + 2\sigma_{xy}^2)^{1/2} - \bar{\sigma} = 0 \tag{7.21}$$

is shown in the left part of Fig. 7.5. In an attempt to enforce compatibility at the point $(0, 0, \sigma_{xy})$ the function F_s could be modified:

$$F_{ss} = (\sigma_x^2 + \sigma_y^2 + \sigma_{xy}^2)^{1/2} - \bar{\sigma} = 0 . \tag{7.22}$$

However, incompatibility then still exists along the lines $\sigma_x = 0$ and $\sigma_y = 0$ (right part of Fig. 7.5). Therefore, assuming that the enhanced Rankine criterion will be active for stress states dominated by tension and not by shear, the yield function F_s from eq. (7.21) is adopted henceforth (this option will be called RS). It can be written in a convenient form:

$$F_s = (\boldsymbol{\sigma}^T \mathbf{P} \boldsymbol{\sigma})^{1/2} - \bar{\sigma} , \tag{7.23}$$

with the auxiliary matrix for plane stress conditions $\mathbf{P} = \text{diag} [1, 1, 2]$. The first and second derivative with respect to stresses can be calculated as for the regular Rankine and a modified strain-hardening hypothesis:

$$\dot{\kappa} = [(\dot{\epsilon}_1^p)^2 + (\dot{\epsilon}_2^p)^2]^{1/2} \tag{7.24}$$

assures the equivalence the plastic strain measure and the plastic multiplier $\dot{\kappa} = \dot{\lambda}$.

It is noted that for the regular Rankine regime, linear softening and standard plasticity algorithm a one-step return mapping to the yield surface is obtained. An immediate return to the smoothing surface F_s is also observed for the zero Poisson effect. The mapping is then orthogonal to the circle in the principal stress space. It is also noted that the problem of distinguishing between the regular and vertex regime is not trivial in the gradient plasticity algorithm. The test of the vertex regime is performed after the

regular mapping, since a trial stress point in the vertex regime may be mapped onto a point in the regular regime. A regime change may also occur during stress redistribution, especially when $\nu \neq 0$ and when for progressive softening the circular function in the tension-tension regime has shrunk almost to the origin. The change of the active yield function may result in a disturbance of convergence, since the plastic multiplier value is determined on the global level, which is correct for one regime and incorrect for the other regime. Therefore the use of $\nu = 0$ is advantageous for the robustness of large-scale computations, if this assumption introduces a marginal error in the model.

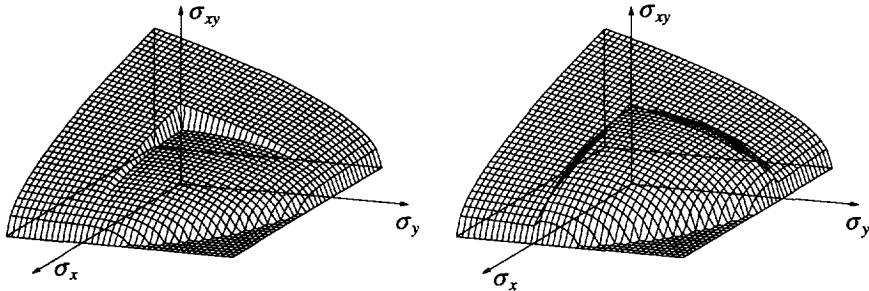


Figure 7.5 Rankine yield surface smoothed in the tension-tension regime by $F_s = 0$ (left) and by $F_{ss} = 0$ (right).

7.1.2 Drucker-Prager type approximation

The Drucker-Prager yield function for plane stress may be written in terms of the principal stresses as follows:

$$F = [(\sigma_1)^2 - \sigma_1 \sigma_2 + (\sigma_2)^2]^{1/2} + \frac{1}{3} \alpha (\sigma_1 + \sigma_2) - k = 0, \quad (7.25)$$

where

$$\alpha = \frac{6 \sin \phi}{3 - \sin \phi}, \quad k = \frac{6 \bar{c} \cos \phi}{3 - \sin \phi}, \quad (7.26)$$

ϕ is the friction angle and \bar{c} is the softening cohesion. For $\alpha \geq 1.5$ the function $F = 0$ is a hyperbola which can be used to approximate the Rankine yield function.

We have investigated two approximations (left part of Fig. 7.6) fulfilling the conditions that $\sigma_2 = f_t$ for $\sigma_1 = 0$ and $\sigma_1 = f_t$ for $\sigma_2 = 0$, where $f_t > 0$ is the uniaxial tensile strength. This condition leads to:

$$k = f_t + \frac{1}{3} \alpha f_t. \quad (7.27)$$

For the first approximation (called DT) we require that the plastic flow direction coincides with the normal to the Rankine yield function for the case of uniaxial tension. The condition that $\partial F / \partial \sigma_2 = 0$ for $\sigma_1 = 0$ leads to $\alpha = 1.5$ and from eqs (7.27) and (7.26) $k = 1.5 f_t$. As can be seen from Fig. 7.6 this approximation is applicable to concrete only for the stress states close to uniaxial tension (including biaxial tension). This

approximating yield function is plotted in the same figure on the right in the $(\sigma_x, \sigma_y, \sigma_{xy})$ space.

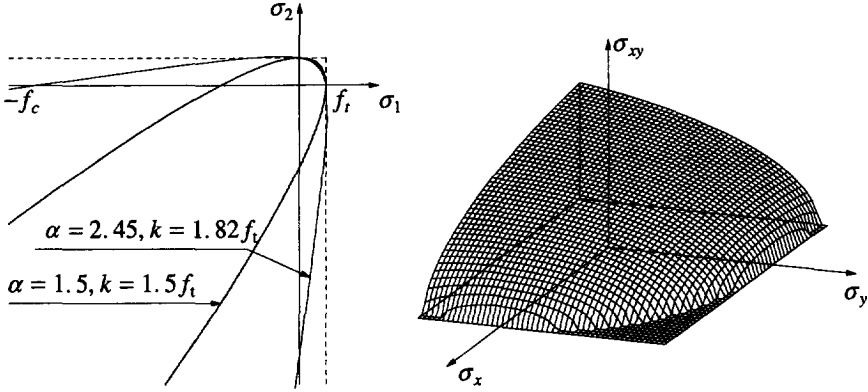


Figure 7.6 Drucker-Prager approximations of the Rankine yield function.

For the second approximation in Fig. 7.6 on the left (called DC) we require that $\sigma_2=0$ for $\sigma_1=-f_c$ and $\sigma_1=0$ for $\sigma_2=-f_c$, where $f_c > 0$ is the uniaxial compressive strength. This gives:

$$\alpha = \frac{3(f_c - f_t)}{f_c + f_t}. \quad (7.28)$$

If for instance $f_c \approx 10f_t$ is assumed for concrete, $\alpha \approx 2.45$ and $k \approx 1.82f_t$ is obtained.

In order to apply the above described Drucker-Prager approximations to the Mode-I fracture problems and compare the results with experiments, a suitable definition of the inelastic strain measure has to be used instead of the strain hardening rule in eq. (5.6). Here the maximum principal plastic strain hypothesis from eq. (7.8) is used just as for Rankine plasticity. Substitution of the plastic strain vector for Drucker-Prager plasticity (cf. Chapter 6.1):

$$\dot{\epsilon}^p = \dot{\lambda} \left(\frac{3\mathbf{P}\boldsymbol{\sigma}}{2\psi_M} + \alpha \mathbf{\Pi} \right), \quad (7.29)$$

with

$$\mathbf{P} = \begin{bmatrix} 2/3 & -1/3 & 0 \\ -1/3 & 2/3 & 0 \\ 0 & 0 & 2 \end{bmatrix}, \quad \mathbf{\Pi} = \begin{bmatrix} 1/3 \\ 1/3 \\ 0 \end{bmatrix} \quad (7.30)$$

and

$$\psi_M = \sqrt{(\sigma_x^2 + \sigma_y^2 - \sigma_x \sigma_y + 3\sigma_{xy}^2)}, \quad (7.31)$$

into eq. (7.9) leads to

$$\dot{\kappa} = |\dot{\epsilon}_1^p| = \dot{\lambda} \left| \frac{3}{4} \frac{\psi_R}{\psi_M} + \frac{1}{4} \frac{(\sigma_x + \sigma_y)}{\psi_M} + \frac{1}{3} \alpha \right|, \quad (7.32)$$

where ψ_R is defined in eq. (7.6). To avoid complications in the formulation encountered when $\eta = \dot{\kappa}/\dot{\lambda}$ is not constant a simplified hardening rule is assumed. This rule coincides with eq. (7.32) for uniaxial tension and reads:

$$\dot{\kappa} = (1 + \frac{1}{3} \alpha) \dot{\lambda} . \tag{7.33}$$

7.2 Four point bending

The geometry in Fig. 7.7 and the material data for the concrete beam are based on the experimental values (Hordijk 1991): Young’s modulus $E = 40000 \text{ N/mm}^2$, tensile strength $f_t = 3.30 \text{ N/mm}^2$, fracture energy $G_f = 0.120 \text{ N/mm}$. Previously a plane strain configuration with linear softening was analyzed (de Borst et al 1992), now we consider the actual plane stress case with nonlinear softening. Both the vertex enhancements of the Rankine fracture criterion are tested, because some stress points in the vertex regime are observed after the peak load. The numerical results are compared with the experimental data.

A value for the internal length $l = 3 \text{ mm}$ is assumed in most of the calculations, so that according to eq. (3.18) the expected width of the localization zone is $w = 2\pi l \approx 18.8 \text{ mm}$. The nonlinear softening relation $\bar{\sigma}(\kappa)$ according to eq. (7.12) is used and the ultimate equivalent fracture strain is: $\kappa_u = 5.14 G_f / (w f_t) \approx 9.92 \times 10^{-3}$. The gradient influence variable $g(\kappa) = -l^2 \bar{\sigma}'(\kappa)$ is then found, see eq. (7.13).

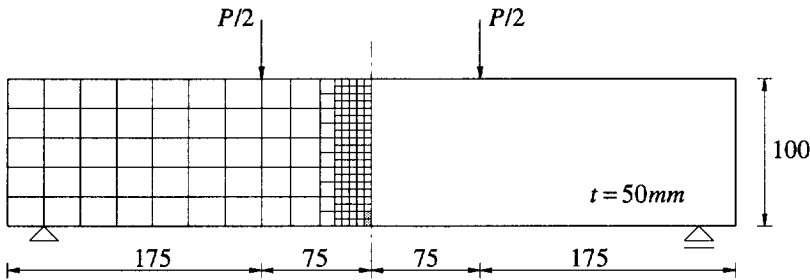


Figure 7.7 Four-point bending test on a plain concrete beam (dimensions in mm).

One half of the beam is discretized using nine-noded elements and the coarse mesh is shown in Fig. 7.7. The fine mesh is similar to the coarse mesh except for the central zone of fracture localization ($25 \times 100 \text{ mm}$), where a uniform refinement is made. In this zone gradient plasticity elements $R34MG$ with a 2×2 integration rule are used, while the other elements are standard and have a 3×3 integration rule. C^0 -elements $Q45MC$ have also been used instead of $R34MG$ with similar results (Pamin and de Borst 1994). To ensure compatibility of the displacement field linear dependence relations are introduced at locations where mesh densification takes place. Deformation control is used: the vertical displacement of the load application point is enforced.

The beam examined first has a $5 \times 10 \text{ mm}$ notch in the midspan. Since for a ‘real’ notch, i.e. with some elements removed from the model, stress concentrations are

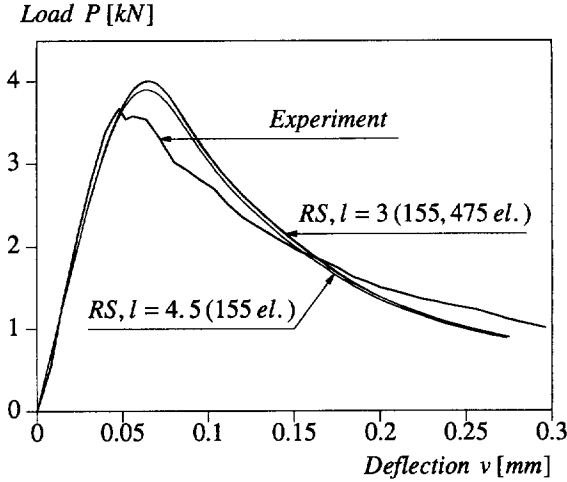


Figure 7.11 Load-displacement diagrams for the smoothed Rankine (RS) model.

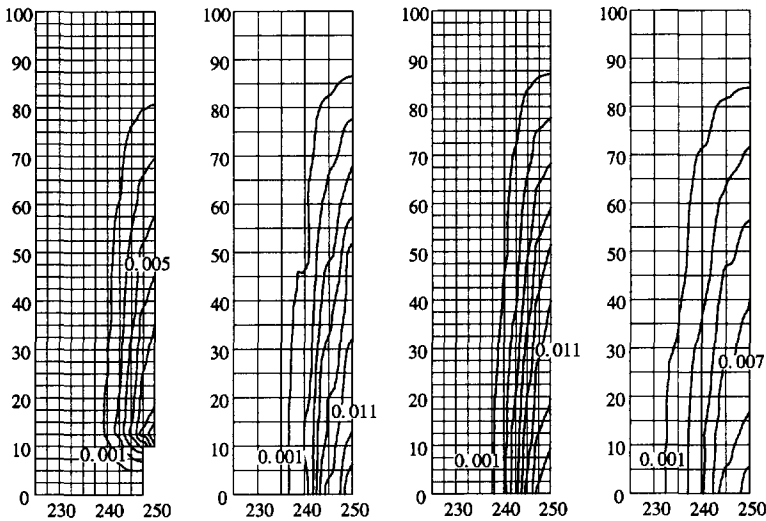


Figure 7.12 Contour plots of equivalent fracture strain for the smoothed Rankine (RS) model. From left to right: 'real' notch, coarse and fine mesh (all $l = 3\text{mm}$), coarse mesh $l = 4.5\text{mm}$.

Very similar load-displacement curves are obtained for both the internal length scales assumed (Fig. 7.11). The reason is that in both cases the fracture energy is equal and governs the softening process. The observation is important if one considers the problem of experimental determination of the internal length scale as a material parameter. It seems that to obtain mesh-objective results we can assume any reasonable (non-zero) value of l . It influences the deformation pattern and the distribution of fracture strains,

but it does not influence the load-displacement relation since the released energy does not change.

In all the cases the expected width of the localization zone is well reproduced (Fig. 7.12). The expansion of the band over this width as observed at the bottom of the beam is caused by the midspan elements, in which softening has been exhausted.

The following figures present the results obtained using the Drucker-Prager type approximation of the Rankine yield function. Fig. 7.13 shows the incremental deformations in the centre of the beam for the two options (cf. Section 7.1.2) and Fig. 7.14 presents the load-displacement diagrams. For option DT the following material data have been used: $c_y = 2.25 \text{ N/mm}^2$, $\sin \phi = 0.60$, $\eta = 1.5$; for option DC: $f_c = 59.5 \text{ N/mm}^2$, $\alpha = 2.68$, $c_y = 5.71$, $\sin \phi = 0.926$, $\eta = 1.89$.

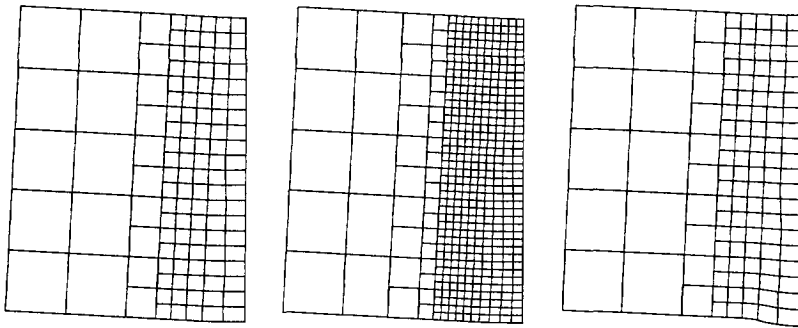


Figure 7.13 Incremental deformations of the elements in the centre of the beam (the right plot for the DC option, the others for the DT option).

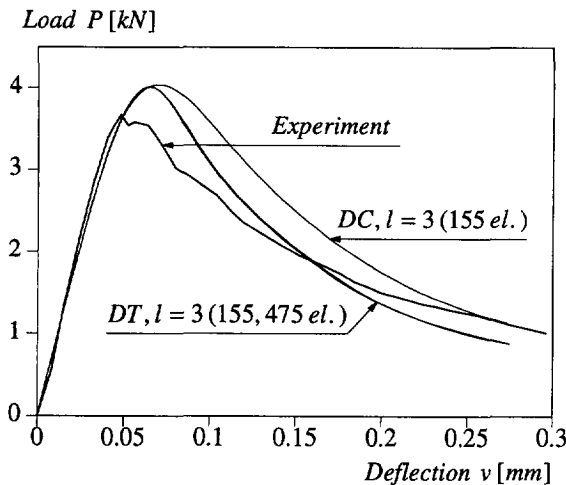


Figure 7.14 Load-displacement diagrams for the Drucker-Prager model.

The option with the fracture 'flow' direction for uniaxial tension equal to that of

Rankine plasticity (DT) gives results very close to the smoothed Rankine model (RS). The Drucker-Prager approximation based on the values of both f_t and f_c (DC) gives a too ductile response. As can be seen on the right deformation pattern in Fig. 7.13, the direction of the fracture 'flow' is not horizontal in this case, causing an incorrect stiffness of the model in Fig. 7.14.

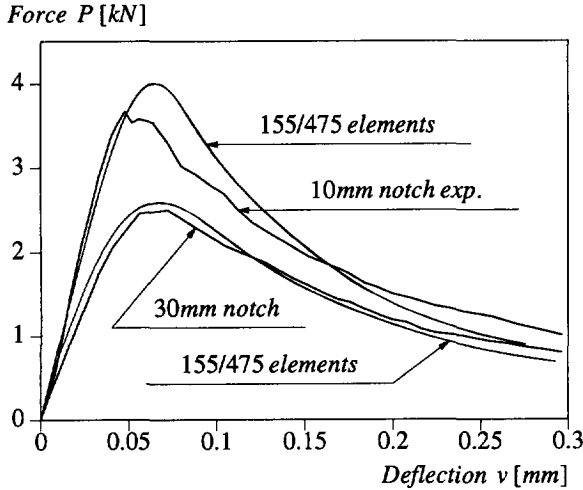


Figure 7.15 Experimental and computed load-displacement diagrams for two notch lengths (nonlinear softening smoothed Rankine model).

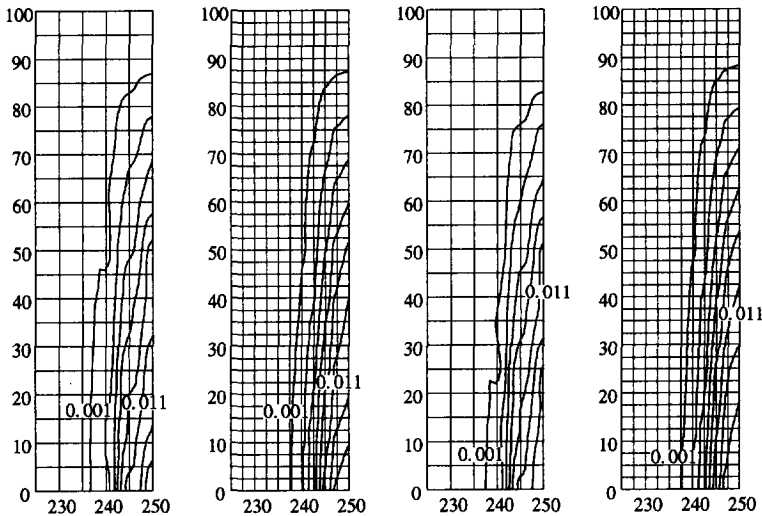


Figure 7.16 Mesh sensitivity of the equivalent fracture strain plots for the final states of nonlinear softening with $l=3\text{mm}$: the Drucker-Prager model (DT) with 10mm notch and $v=0.2$ on the left, the smoothed Rankine model (RS) with 30mm notch and $v=0.0$ on the right.

Finally a similar beam with a larger notch $5 \times 30\text{mm}$ is examined using the smoothed Rankine model and the load-displacement diagrams are compared in Fig. 7.15. This time a 90% smaller thickness in the notch area is used instead of the 'real' notch. Fig. 7.15 shows that for this beam the numerical predictions are even closer to the experimental curves. The correct invariance with respect to mesh refinement for the Drucker-Prager model and for the larger notch are presented in Fig. 7.16.

In the analysis of the three subsequent problems we will use only the smoothed Rankine yield function (option RS) and the most reliable eight-noded C^1 -continuous gradient plasticity elements *R32MG*. Despite the stress locking in the notch area, which causes convergence problems especially in the peak load regime of the analysis, we will include 'real' notches in the numerical models.

7.3 Direct tension test

The direct tension test has been performed on notched plain concrete specimens under deformation control (Hordijk 1991) and has been analyzed before with the smeared cracking model (Rots and de Borst 1989). From this paper we have adopted the test configuration (Fig. 7.17 on the left) and the material data for lightweight concrete: $L = 250\text{mm}$, $B = 60\text{mm}$, thickness $t = 50\text{mm}$, Young's modulus $E = 18000\text{ N/mm}^2$, tensile strength $f_t = 3.4\text{ N/mm}^2$ and fracture energy $G_f = 0.0593\text{ N/mm}$.

The internal length scale $l = 2\text{mm}$ and the ultimate equivalent fracture strain $\kappa_u \approx 7.14 \cdot 10^{-3}$ (corresponding to the above value of the fracture energy) are assumed. The Poisson ratio ν is taken equal to zero. The specimen is fixed at the bottom and tied to a rigid plate at the top. A rotational spring, modelling the stiffness of the testing rig, is included to counteract the rotation of the upper plate. The average deformations are measured over a base $L_m = 35\text{mm}$ according to the original position of five extensometers. Indirect displacement control (de Borst 1986) using the vertical displacements of the nodes at the gauge positions is applied to control the loading.

Fig. 7.17 presents the deformations of the specimen for two cases: firstly, the rotation of the upper edge is prevented by a rotational spring with a stiffness $k_r = 10^9\text{ Nmml/rad}$ and, secondly, free rotation is assumed ($k_r = 0$). Fig. 7.18 shows the load-displacement diagrams for these two cases. On the left a relation between the nominal stress $\sigma_N = P/(tB_0)$ and the average displacement over the measuring length L_m is plotted, on the right the same nominal stress is plotted versus the vertical displacement of the upper edge (elongation of the bar). A snap-back response is observed in the latter diagram, which is due to the elastic unloading outside the fracture zone. This demonstrates the necessity of a careful choice of degrees of freedom for the loading control in the experiment and the advantage of using the indirect displacement control in numerical simulations of localization phenomena.

For both cases the specimen exhibits flexing to one side starting at the peak load. In the absence of the rotational constraint the whole further deformation is nonsymmetric. When the rotational stiffness is included in the model, the nonsymmetric stage of fracture development is followed by a symmetric failure mode (Fig. 7.19).

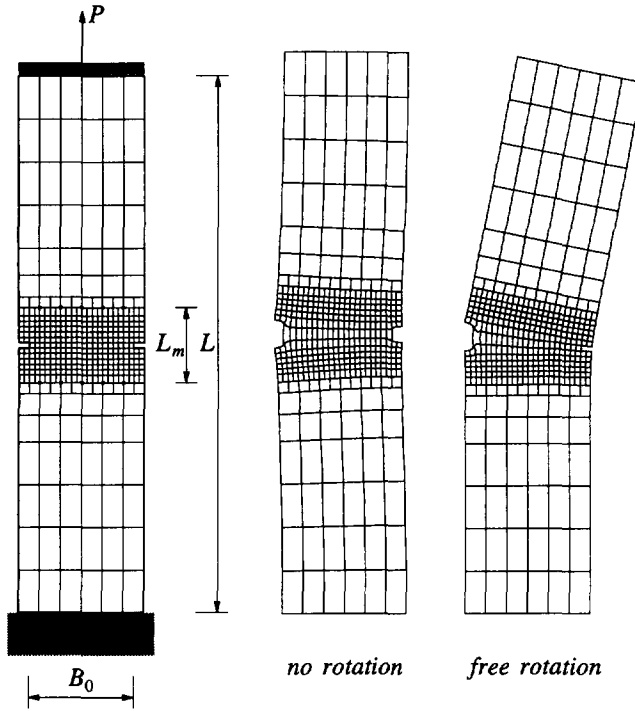


Figure 7.17 Configuration of the direct tension test and simulated deformation patterns for the specimen with rotational spring at the top and with free rotation.

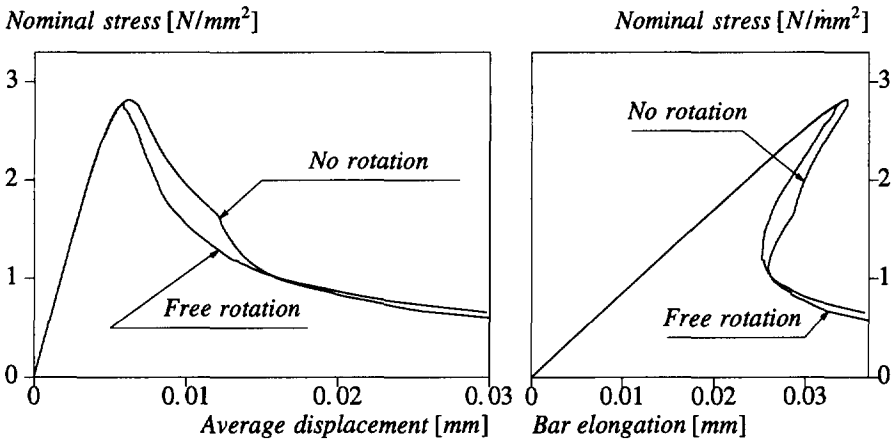


Figure 7.18 Load-displacement curves obtained using the gradient-dependent model.

The return to the symmetric mode corresponds to the bump on the load-displacement curves. The temporary nonsymmetric development of fracture is consistent with experimental results (Hordijk 1991) and analytical arguments (Bažant and Cedolin 1993).

The response of the model with non-zero rotational stiffness is similar to the results obtained for the smeared cracking model with exponential softening (Rots and de Borst 1989), where localization of fracture occurred in just one row of elements in the absence of a localization limiter. In the context of comparison with the classical cracking models it is also mentioned, that the occurrence of spurious mechanisms activated in finite element calculations by the loss of material stability (cf. de Borst and Rots 1989) is very much reduced by the gradient regularization.

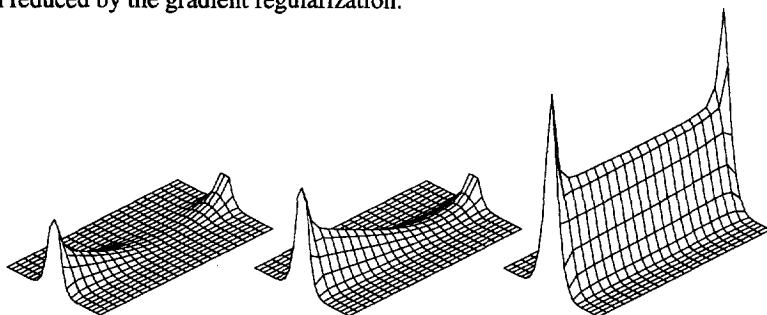


Figure 7.19 Evolution of the fracture strain field (nonsymmetric deformation).

We will further analyze the actual case with the rotational stiffness of the testing machine included. In Fig. 7.20 load-displacement diagrams for the temporarily nonsymmetric evolution of fracture are compared with another simulation, in which symmetry has been enforced during the whole fracture process. Only a slight mesh-sensitivity is visible for both cases (it is noted that the mesh has been refined in the centre area of the specimen only in the axial direction).

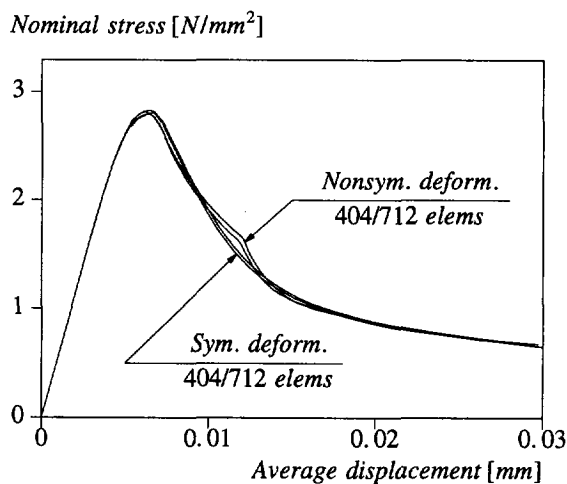


Figure 7.20 Mesh sensitivity of gradient plasticity results.

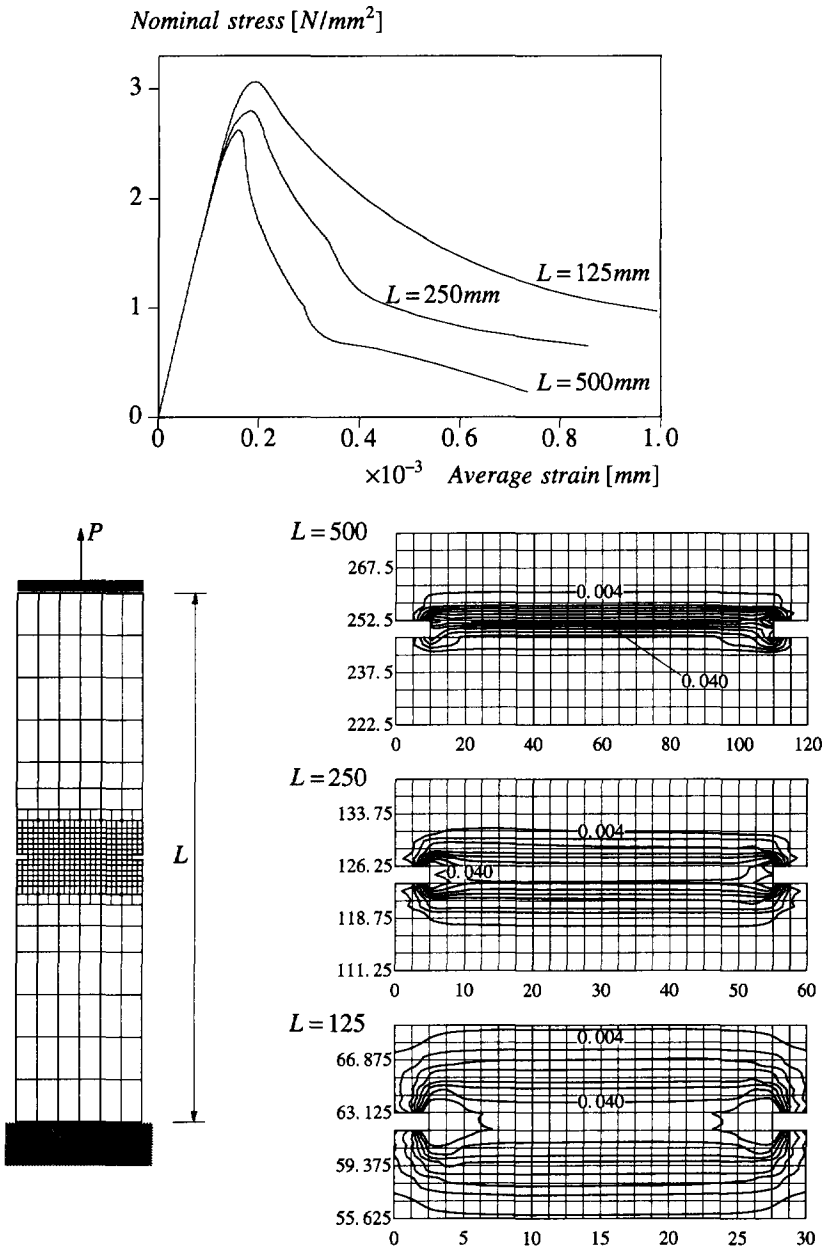


Figure 7.21 Size effect simulations: stress-strain diagrams and contour plots of equivalent fracture strain for three sizes of the specimen at $0.25\sigma_{Nmax}$.

The load-displacement diagram in Fig. 7.21 shows relations between the nominal stress and the average strain, defined as the average displacement divided by the measuring length L_m , obtained numerically for three specimens scaled uniformly. A size effect in

both the peak stress (load carrying capacity) and strain softening response can be observed. This numerical prediction of the size effect is possible since the internal length scale $l=2\text{mm}$ sets the width of the fracture band ($w\approx 12.6\text{mm}$), which is equal for the three specimen sizes as demonstrated in Fig. 7.21 on the contour plots of the equivalent fracture strain.

7.4 Single-edge-notched beam

The single-edge-notched beam in Fig. 7.22 has been investigated by Schlangen (1993) experimentally and numerically using a lattice model. The beam has a 5 mm wide and 20 mm deep notch on the symmetry axis at the top. It is subjected to an anti-symmetric loading and shows a cracking failure dominated by Mode-I action (cf. Carpinteri et al 1993).

The material data for concrete, based on experimental values (cf. Schlangen and van Mier 1991, Schlangen 1993) are as follows: Young's modulus $E=35000\text{ N/mm}^2$, tensile strength $f_t=3.00\text{ N/mm}^2$, fracture energy $G_f=0.10\text{ N/mm}$. To preserve the robustness of the Rankine gradient plasticity algorithm with vertex smoothing the Poisson ratio equal to zero is taken, which, for the plane stress configuration, involves a negligible deviation of results with respect to the real case with $\nu=0.2$.

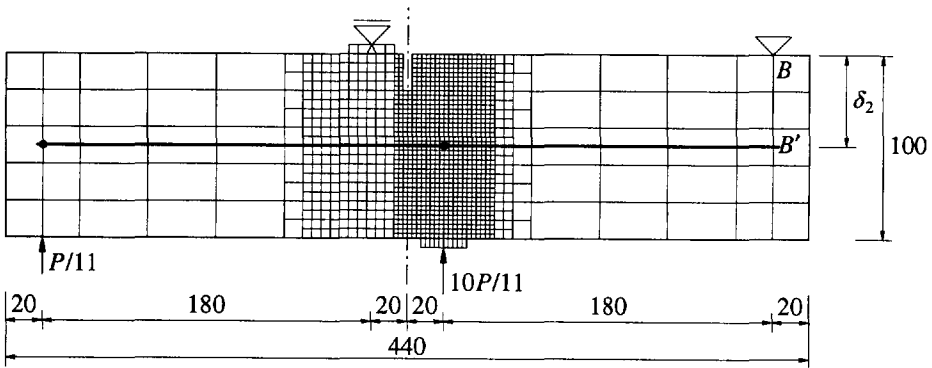


Figure 7.22 Single-edge-notched beam with discretization (dimensions in mm).

In the experiments a monotonically increasing deformation parameter δ_2 has been measured between the right support B and point B' on a reference bar glued to the beam above the points of load application. The beam is now analyzed numerically under indirect arc length control using the same controlling parameter δ_2 .

Since fracture takes place in the middle of the beam, the element mesh (Fig. 7.22) is composed of the following parts:

- the middle zone ($115\times 100\text{mm}$) with a 'real' notch, discretized using eight-noded gradient plasticity elements $R32MG$; the additional boundary conditions for the plastic multiplier λ are imposed on the boundaries of this zone; along the remeshing lines the degrees of freedom for λ in the nodes of the finer mesh are tied linearly to

the neighbouring nodes, which is an approximation,

- two coarse mesh zones of standard eight-noded elements on both sides of the beam,
- the loading plates discretized with standard quadrilateral and triangular elements having ten times higher stiffness $E = 350000 \text{ N/mm}^2$.

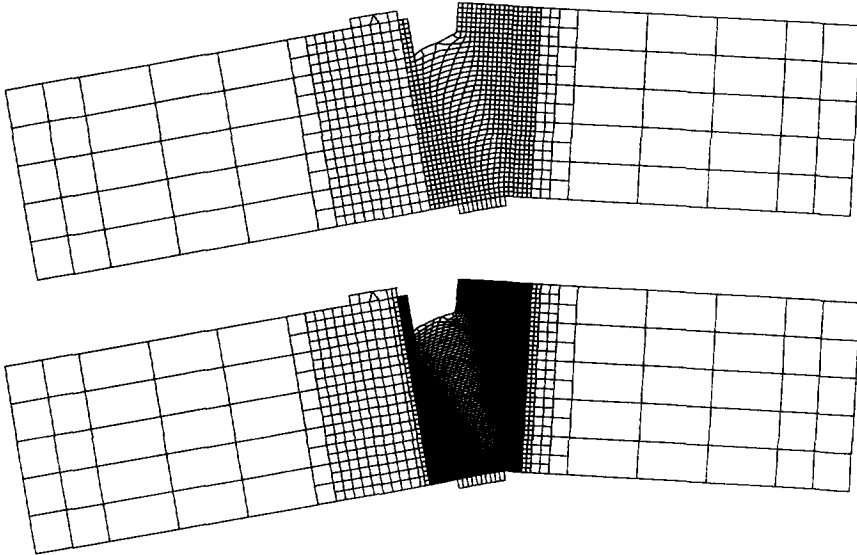


Figure 7.23 Total deformations of the numerical model with the medium and fine discretization at the final load level.

As in the previous tests the nonlinear softening rule and the decreasing gradient influence according to eqs (7.12-7.13) are used. In the first simulation an internal length scale $l = 3 \text{ mm}$ ($\kappa_u = 9.09 \cdot 10^{-3}$) is assumed, then $l = 2 \text{ mm}$ ($\kappa_u = 0.0136$) is taken. In the third simulation the fracture energy is doubled to observe its influence on the peak load and ductility of the response ($l = 3 \text{ mm}$ is assumed). To study the mesh-sensitivity and to check whether the curved crack obtained in experiments can be reproduced, the mesh in the central area ($50 \times 100 \text{ mm}$) is refined uniformly in the fourth simulation, while $l = 2 \text{ mm}$. In Fig. 7.23 a comparison of deformation patterns for the two discretizations is presented. Mode-I crack opening is observed.

Figures 7.24-7.25 show load-displacement diagrams for the experiment (Schlangen 1993) and the four cases. In the first figure the relation between the load and the parameter δ_2 is shown and in the second figure the relation between the load and the crack-mouth sliding displacement (CMSD) is presented. The global behaviour of the beam is reproduced satisfactorily with the Rankine gradient plasticity model and the simulation results are close to the experiment. For $G_f = 0.1 \text{ N/mm}$ three curves are shown: for the two meshes with $l = 2 \text{ mm}$ and for the coarser mesh with $l = 3 \text{ mm}$. The load-deformation diagram is governed by the value of the fracture energy and it is almost not affected by

either mesh refinement or the change of the internal length scale.

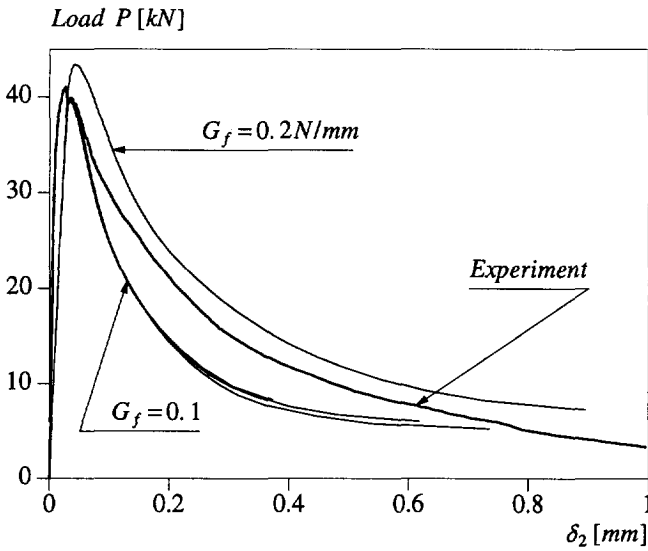


Figure 7.24 Computed and experimentally obtained load- δ_2 diagrams.

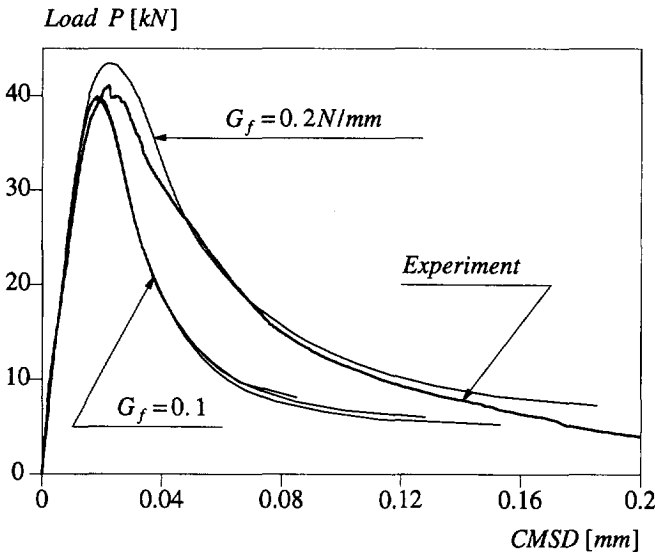


Figure 7.25 Computed and experimentally obtained load-CMSD diagrams.

Figs 7.26-7.27 present the expected regularization effect: the fracture is distributed over a band having a width determined by the internal length scale. The equal value contours for the equivalent fracture strain are similar for the two used meshes. At the same time the experimental propagation of the primary crack along a curved line is not reproduced.

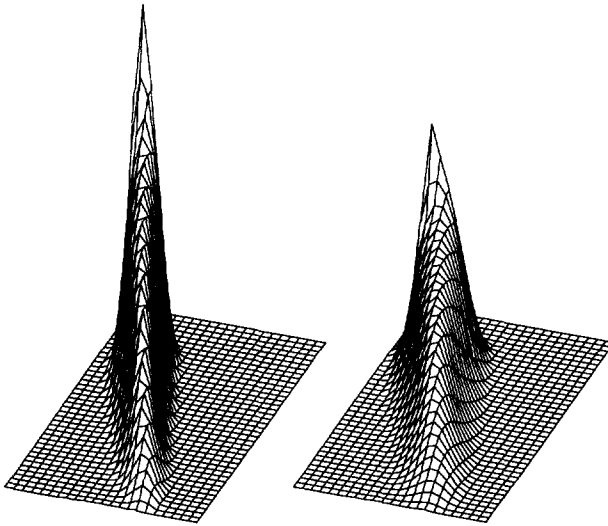


Figure 7.26 Equivalent fracture strain field for $l = 2\text{mm}$ (left) and $l = 3\text{mm}$ (right).

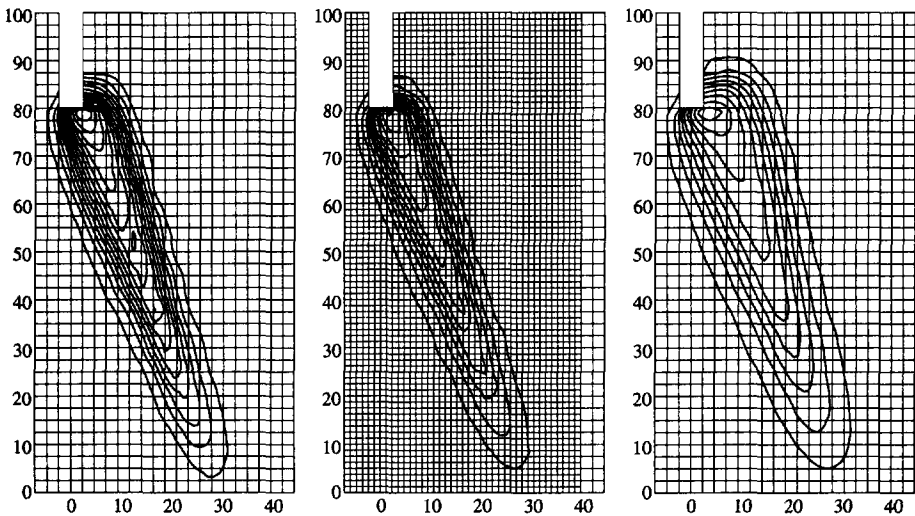


Figure 7.27 Contour plots of equivalent fracture strain at the final load level for $l = 2\text{mm}$ (left and middle) and $l = 3\text{mm}$ (right).

7.5 Double-edge-notched specimen

Fig. 7.28 shows the configuration of a mixed-mode concrete fracture test, analyzed experimentally by Nooru-Mohamed (1992). The double-edge-notched specimen was placed in a special loading frame that allowed for the analysis of various loading paths

of combined shear and tension under force or deformation control.

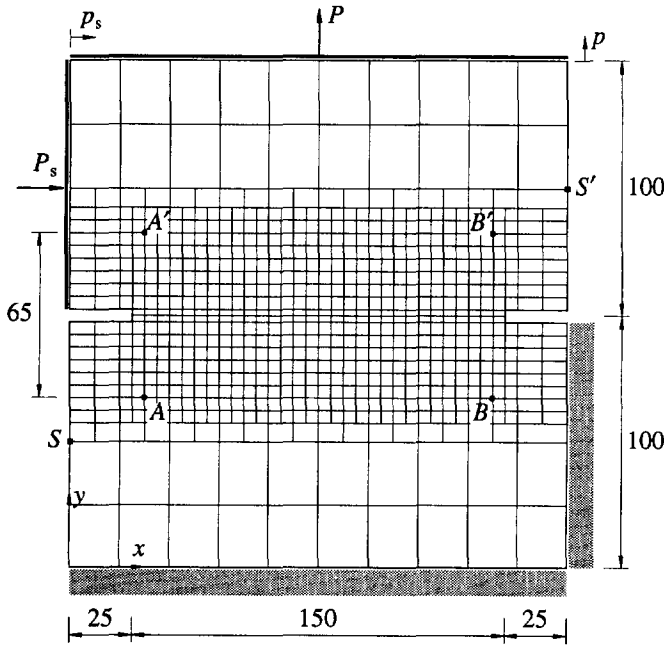


Figure 7.28 Double-edge-notched concrete specimen with discretization (dimensions in mm).

Three specimen sizes ($L \times L$) were used in the experiments: 200×200 , 100×100 , 50×50 mm. The sizes of symmetrical notches were 25×5 , 12.5×5 and 6.25×5 mm, respectively, and the specimen thickness was for all cases $t = 50$ mm. The specimen was supported at the bottom and along the right-hand side below the notch. The shear force P_s was applied through the frame above the notch along the left-hand side of the specimen and the tensile force P was applied at the top. The frames were glued to the specimen. The relative shear deformation between the upper and lower half of the specimen δ_s was measured at the points S and S' on both sides and the relative normal deformation in the fracture zone δ was measured between the points A and A' as well as B and B' and averaged. Owing to the servo-controlled system the loading could also be controlled by the deformations δ_s and δ .

We have analyzed two of the loading paths considered by Nooru-Mohamed (1992) using the Rankine gradient dependent plasticity with the smoothed vertex. In the first series of simulations the largest specimen is used. The shear force is applied under force control and then kept constant while the normal loading is imposed under deformation control of δ (path 4 from the experiment). In the second series all three sizes are analyzed to verify the size effect. To obtain a monotonic increase of loading, the shear and tension are applied simultaneously under the control of the horizontal and vertical

displacements p_s and p with the condition $p = p_s$. It is noted that this deformation control is only a numerically convenient approximation of the real case, since in the experiment (path 6) δ_s and δ were used to control the loading.

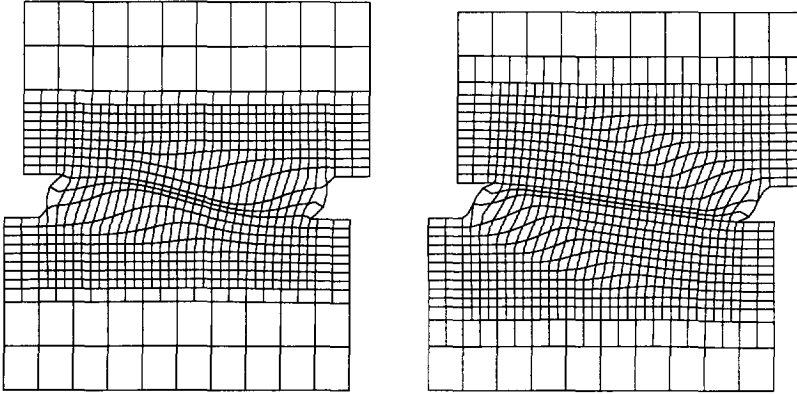


Figure 7.29 Incremental deformations of the largest specimen at the final tensile load level (path 4, $P_s = 10kN$ on the left, $P_{s\max}$ on the right).

The material data used in numerical simulations are as follows: Young's modulus $E = 30000 N/mm^2$, Poisson's ratio $\nu = 0.0$, tensile strength $f_t = 0.8 f_{spl} \approx 3.00 N/mm^2$, fracture energy $G_f = 0.10 N/mm$. The same nonlinear softening rule as in the previous chapters is employed. Unless stated otherwise, the internal length scale $l = 2mm$ ($\kappa_u = 0.0136$) is assumed.

In Fig. 7.28 we have presented the geometry of the specimen $200 \times 200mm$ and the finite element mesh used in the calculations. The central zone of refined mesh ($50 \leq y \leq 150$) is composed of eight-noded gradient plasticity elements *R32MG* and the coarse mesh zones at the top and at the bottom are discretized with standard serendipity elements. Additional boundary conditions for the plastic multiplier field are enforced on the boundaries of the fine mesh and the respective displacements are tied on the remeshing lines to preserve the displacement continuity.

Fig. 7.29 presents the final deformation patterns of the largest specimen for two levels of the lateral confining load (path 4). Figs 7.30 and 7.31 show the experimentally determined and numerically simulated relations between the tensile load P and the normal displacement δ and between δ and the shear displacement δ_s .

The calculated maximum shear load $P_{s\max} = 29.7kN$ is larger than the experimental value (about $27.5kN$) and the ultimate carrying capacity under subsequent tension is even stronger overestimated, which is attributed to the stress locking in the notch area and overestimation of the cracking stress in the presence of the lateral compression. On the other hand, the Rankine gradient plasticity model reproduces correctly the character of the experimental curves and is close to experiments for progressive softening.

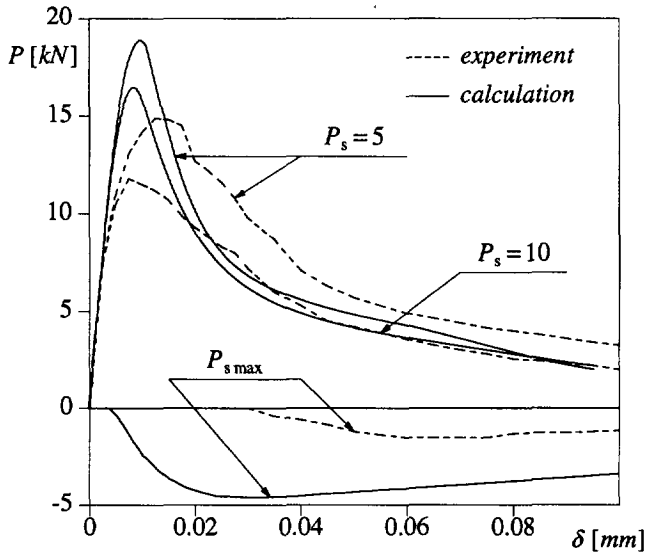


Figure 7.30 Computed and experimental tensile force versus average normal displacement diagrams (path 4).

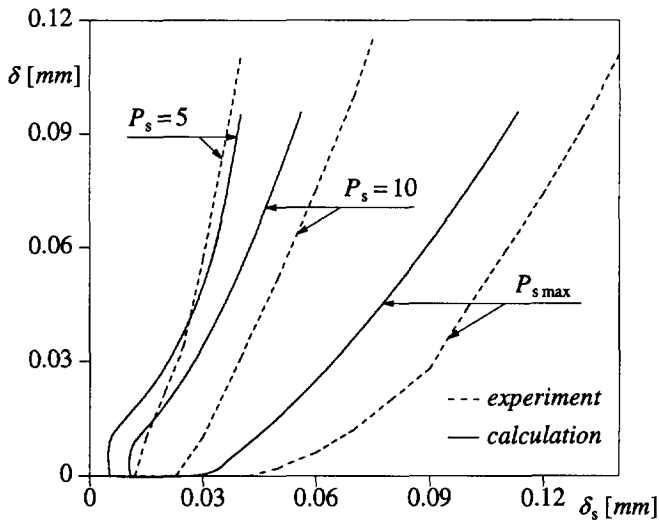


Figure 7.31 Computed and experimental relations between the average normal and shear displacement (path 4).

The simulated fracture process zones are compared in Fig. 7.32 with the average experimental crack positions, i.e. an average of the experimental crack locations at the front and back of the specimen are plotted. The agreement is reasonable and no bias of the mesh lines is found as was the case in the smeared cracking simulations (Nooru-

Mohamed 1992). It is noted that for the case with $P_{s\max}$ the central zone of gradient plasticity elements had to be extended over the area $40 \leq y \leq 160$ in order to admit the inclined 'crack' propagation. For the case $P_s = 5kN$ two fracture zones developing from the notches finally join, for the other cases the width of the compressive strut is estimated correctly. The width of the fracture zones corresponds well to the assumed value $w = 2\pi l \approx 12.6mm$. However, as for the SEN beam in the previous chapter, the curved character of the cracks cannot be simulated.

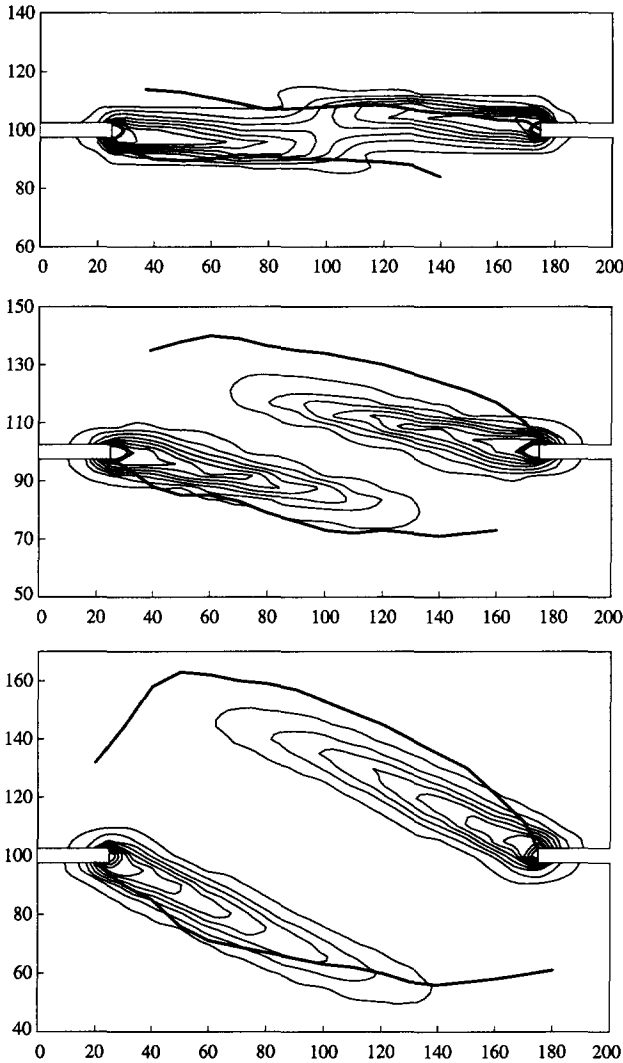


Figure 7.32 Contour plots of equivalent fracture strain at the final tensile load level for the three lateral confining load levels (from the top $P_s = 5, 10, P_{s\max}$).

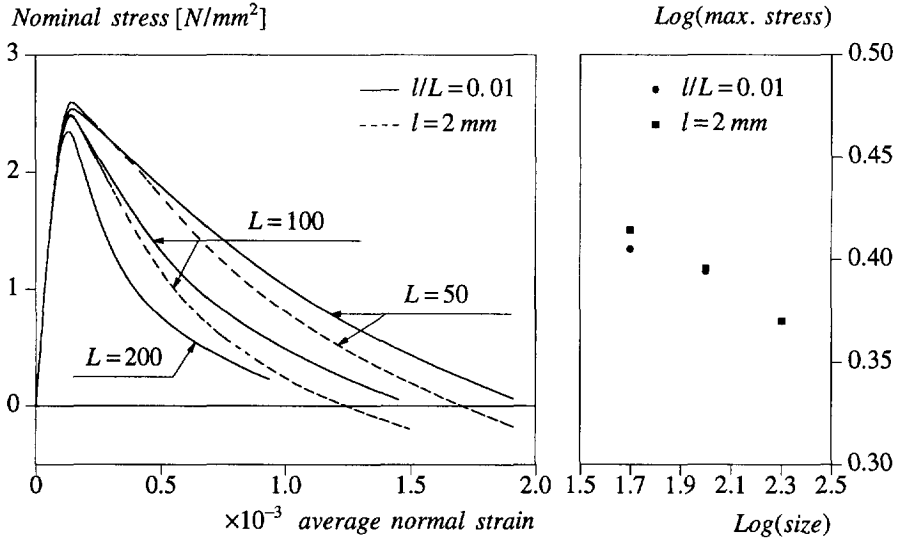


Figure 7.33 Nominal tensile stress versus average tensile strain diagram and the size effect on the peak-stress (path 6).

In the second series of calculations we have applied simultaneously equal shear and tensile deformation (path 6). Fig. 7.33 shows the calculated diagrams for the relation between the nominal stress ($P/(tL_0)$, where L_0 is the load carrying length equal to 150, 75 and 37.5mm for the three respective specimen sizes, and the average normal strain (δ/L). For the smaller specimens two possibilities are considered: a changing internal length $l=1/0.5\text{mm}$ (so that $l/L=0.01$) and a constant internal length $l=2\text{mm}$. For all cases the fracture energy G_f is the same.

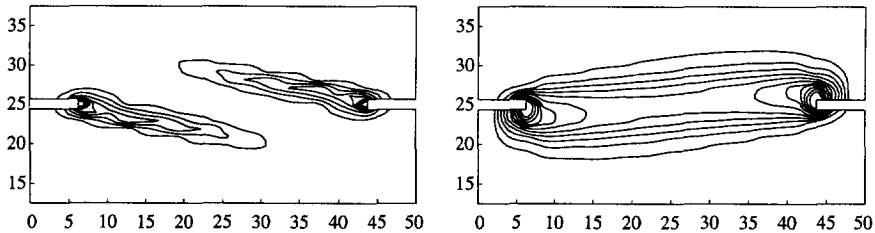


Figure 7.34 Contour plots of equivalent fracture strain for the smallest specimen and different internal length values: $l=0.5\text{mm}$ (left) and $l=2\text{mm}$ (right).

As can be seen in Fig. 7.34 the choice of the internal length can influence the predicted fracture mode. If the internal length scale is decreased together with the specimen size, two cracks are predicted for all three specimens. If the internal length is kept constant, we find just one fracture zone for the medium and small specimen. It is noted that in the experiments both crack patterns, distributed and with dominant cracks, were

observed in the series of medium and small specimens. From Fig. 7.33 we observe, that the choice of the internal length influences the softening behaviour. A classical size effect is found both in the peak-stress value and the post-peak regime although in the experiment a reversed size effect was found for path-6 tests. It is mentioned that since an internal length scale is incorporated in the numerical model, the predicted size effect law need not be a power law and our results correspond to the predictions of nonlinear elastic fracture mechanics (Bažant 1992).

In sum, the gradient-dependent Rankine plasticity model seems to be less accurate for the mixed-mode fracture problem than for the plain Mode-I cases analyzed previously. However, the localization limiting properties of gradient plasticity make the results physically reasonable and much closer to experiments than the results of the smeared-cracking model (Nooru-Mohamed 1992).

8. Conclusions

In this thesis the potential of gradient-dependent plasticity (Mühlhaus and Aifantis 1991, de Borst and Mühlhaus 1992) as a localization limiter in shear (Mode-II), tension (Mode-I) and mixed mode problems has been assessed. The employed continuum theory, summarized in Chapter 3, includes a regularizing dependence of the yield function on higher-order spatial derivatives of a plastic strain measure and therefore the boundary value problem for a softening continuum remains well-posed in the post-peak regime.

The fundamental feature of the used algorithm is a weak (and not pointwise) satisfaction of the yield condition, which is coupled with a weak equilibrium condition. Various aspects of finite element implementation of the gradient plasticity have been studied in Chapter 4. The dependence of the yield function on the Laplacian of the plastic strain measure induces the necessity of C^1 -continuous interpolation of the plastic strain field in the incremental formulation. A new C^0 -approach has been developed, in which the continuity requirement is relaxed by treating the first derivatives of the plastic multiplier as additional unknowns and connecting them to the plastic multiplier field using a penalty constraint. Several C^1 - and C^0 -continuous, rectangular and triangular elements have been examined.

Most of the implemented elements introduce properly the localization limiting properties of the gradient-dependent continuum: the results of finite element simulations are almost insensitive to mesh refinement or alignment, since the width of the shear bands (fracture process zones) is determined by the internal length scale incorporated in the theory. However, it turns out that for robustness the elements should fulfil some additional conditions:

- The balance of interpolations for displacements \mathbf{u} and plastic multiplier λ . The best agreement is found between quadratic shape functions for \mathbf{u} and cubic hermitian polynomials for λ or quadratic shape functions for λ and its derivatives.
- The existence of a suitable integration quadrature. A sufficient number of integration points is necessary to prevent zero-energy modes for \mathbf{u} and λ fields without introducing too many constraints and the sampling positions should be optimal for accuracy.
- The availability of additional boundary conditions for the λ field, necessary in combination with a symmetric tangent operator and helpful in removing spurious modes for the plastic multiplier field.

A failure to satisfy these conditions manifests itself by stress oscillations and/or incorrect return mappings, deterioration of the convergence rate and reliability of the solution. Since the employed set of integral equations for equilibrium and plastic yielding is coupled, an error in the satisfaction of one equation may affect adversely the other equation.

In Chapter 5 the behaviour of various gradient plasticity elements has been compared using a shear banding test. The above discretization requirements favour the use of rectangular/quadrilateral elements with reduced integration. In fact, among the

analyzed two-dimensional elements only the eight-noded serendipity/hermitian element *R32_G* fulfils all the requirements, but nine-noded elements *R34_G* and *Q45_C/Q43_C* also give proper results, if a sufficient number of additional boundary constraints are introduced in the model. None of the implemented triangular elements fulfils the above robustness conditions. Among them, the six-noded quadratic/non-conforming element *T21_G* with 3 integration points performs the best.

The regularization is essentially active if the shear/fracture band is larger than the element size, which means that the meshes used must be fine enough. Upon further mesh refinement convergence to a meaningful solution is then guaranteed. Since the considered problems involve high strain gradients, fine meshes or adaptive meshing techniques should be used.

The size of an imperfect zone that initiates localization does not seem to be important for this localization limiter: it is the internal length scale included in the theory that defines the size of the localization zone. It has also been shown that the regularization does not assure the uniqueness of solution. Boundary conditions, imperfection position and sometimes also discretization influence the localization mode.

The problems solved in Chapters 6 and 7 proved that the gradient plasticity models may be successfully applied in the numerical verification of experiments as well as the simulation of instability phenomena in frictional materials. The approach is equally effective for the description of localized failure under Mode-I, Mode-II and mixed-mode conditions.

The geotechnical problems analyzed in Chapter 6 have shown that the Drucker-Prager softening gradient plasticity is capable of predicting various instability modes in soil specimens or soil masses. The main field of application, i.e. concrete cracking, has been analyzed in Chapter 7. It has been shown that the Rankine softening gradient plasticity reproduces closely the experimentally observed structural response and size effect. The load-deformation diagrams for these problems are governed by the value of fracture energy G_f and are not affected by the assumed value of the internal length, unless its change results in a different localization mode.

The fracture problems require a vertex-enhancement of the Rankine criterion for the proper modelling of Mode-I and mixed mode fracture of concrete. Though no fully robust solution has been found within the frame of the present algorithm, acceptable results have been obtained when the vertex is smoothed using a circular yield function in the principal stress tension-tension regime as well as a Drucker-Prager type approximation. It has also turned out that a nonlinear softening rule should be used to reproduce closely experimental results of concrete fracture problems and to preserve the good algorithmic performance for progressive fracture.

While the present solution algorithm for gradient plasticity performs very well for relatively smooth strain/stress fields, the return mapping determined by the nodal plastic multiplier variables is not sufficiently accurate in case of stress concentrations (e.g. at notches) and sudden changes of the plastic flow direction (e.g. when the vertex regime of the Rankine criterion is entered). This problem, which is a consequence of the weak

fulfilment of the yield condition, causes convergence deterioration especially in the peak load regime.

The gradient plasticity elements augmented with the classical mass matrix have been applied to preserve hyperbolicity in the wave propagation problems (Sluys et al 1993, Sluys 1994). Though no such examples have been shown, the gradient plasticity elements with embedded reinforcement bars can also be used in calculations of reinforced concrete structures.

A further investigation of the applicability of the gradient regularization to more advanced elasto-plastic models is necessary, for example to the Cam-clay model (cf. Gens and Potts 1988) for soils, to the Leon model (cf. Willam and Etse 1990) and the plasticity model with composite yield criteria (e.g. Feenstra 1993) for concrete. The main difficulty seems to lie in resolving the vertices in a computationally efficient manner. Moreover, an investigation of gradient-dependent yield surfaces in the strain space and an extension of the formulation to finite deformations is suggested. It is also emphasized that the experimental determination of the internal length scale for various materials is of primary importance. In this way reliable and robust continuum models with the gradient localization limiter could be offered to material analysts and designers of complex mechanical systems.

References

- AIFANTIS E.C. (1984) - On the microstructural origin of certain inelastic models, *J. Eng. Mater. Technol.*, **106**, p. 326-330.
- AIFANTIS E.C. (1987) - The physics of plastic deformation, *Int. J. Plasticity*, **3**, p. 211-247.
- BARLOW J. (1976) - Optimal stress locations in finite element model, *Int. J. Num. Meth. Eng.*, **10**, p. 243-251.
- BAŽANT Z.P. and OH B. (1983) - Crack band theory for fracture of concrete, *RILEM Materials and Structures*, **16**, p. 155-177.
- BAŽANT Z.P., BELYTSCHKO T. and CHANG T.-P. (1984) - Continuum theory for strain softening, *ASCE J. Eng. Mech.*, **110**, p. 1666-1692.
- BAŽANT Z.P. and LIN F.-B. (1988) - Non-local yield limit degradation, *Int. J. Num. Meth. Eng.*, **26**, p. 1805-1823.
- BAŽANT Z.P. and PIAUDIER-CABOT G. (1988) - Nonlocal continuum damage, localization instability and convergence, *ASME J. Appl. Mech.*, **55**, p. 287-293.
- BAŽANT Z.P. and OŽBOLT J. (1990) - Nonlocal microplane model: tensile and compression fractures and triaxial damage, *Proc. Second Int. Conf. Computer Aided Analysis and Design of Concrete Structures*, Eds N. Bićanić et al, Pineridge Press, Swansea, p. 809-828.
- BAŽANT Z.P. (1992) - Scaling laws in mechanics of failure, *ASCE J. Eng. Mech.*, **119**, p. 1828-1845.
- BAŽANT Z.P. and CEDOLIN L. (1993) - Why direct tension test specimens break flexing to one side, *ASCE J. Struct. Eng.*, **119**, p. 1101-1113.
- BAŽANT Z.P. (1994) - Nonlocal damage theory based on micromechanics of crack interactions, *ASCE J. Eng. Mech.*, **120**, p. 593-617.
- BECKER E. and BÜRGER W. (1975) - *Kontinuumsmechanik*, Chapter 7, Teubner Studienbücher, B.G. Teubner, Stuttgart.
- BELYTSCHKO T., ONG J.S.-J., LIU W.K. and KENNEDY J.M. (1984) - Hourglass control in linear and nonlinear problems, *Comp. Meth. Appl. Mech. Eng.*, **43**, p. 251-276.
- BELYTSCHKO T. and LASRY D. (1989) - A study of localization limiters for strain-softening in statics and dynamics, *Comp. & Struct.*, **33**, p. 707-715.
- BELYTSCHKO T., CHIANG H.-Y. and PLASKACZ E. (1992) - 'Two dimensional shear band computations and the effects of imperfection', *Proc. Third Int. Conf. Computational Plasticity: Fundamentals and Applications*, Eds D.R.J. Owen et al, Pineridge Press, Swansea, p. 509-519.
- BENALLAL A., BILLARDON R. and GEYMONAT G. (1991) - 'Localization phenomena at the boundaries and interfaces of solids', *Proc. Third Int. Conf. Constitutive Laws for Engineering Materials: Theory and Applications*, Ed. C.S. Desai, p. 387-390, Tucson, Arizona.
- DE BORST R. (1986) - *Non-linear analysis of frictional materials*, Dissertation, Delft University of Technology, Delft.

- DE BORST R. (1987) - Integration of plasticity equations for singular yield functions, *Comp. & Struct.*, **26**, p. 823-829.
- DE BORST R. (1989) - Numerical methods for bifurcation analysis in geomechanics, *Ing.-Arch.*, **59**, p. 160-174.
- DE BORST R. and ROTS J.G. (1989) - Occurrence of spurious mechanisms in computations of strain-softening solids, *Eng. Comput.*, **6**, p. 272-280.
- DE BORST R. and FEENSTRA P.H. (1990) - Studies in anisotropic plasticity with reference to the Hill criterion, *Int. J. Num. Meth. Eng.*, **29**, p. 315-336.
- DE BORST R. (1991) - The zero-normal-stress condition in plane-stress and shell elastoplasticity, *Comm. Appl. Num. Meth.*, **7**, p. 29-33.
- DE BORST R. (1991) - Simulation of strain localisation: A reappraisal of the Cosserat continuum, *Eng. Comput.*, **8**, p. 317-332.
- DE BORST R. and MÜHLHAUS H.-B. (1991) - 'Continuum models for discontinuous media', *Fracture Processes in Concrete, Rock and Ceramics*, Eds J.G.M. van Mier et al, E & FN Spon/Chapman & Hall, London, p. 601-618.
- DE BORST R. and MÜHLHAUS H.-B. (1992) - Gradient-dependent plasticity: Formulation and algorithmic aspects, *Int. J. Num. Meth. Eng.*, **35**, p. 521-539.
- DE BORST R., MÜHLHAUS H.-B. and PAMIN J. (1992) - 'A gradient continuum model for Mode-I fracture in concrete and rock' *Fracture Mechanics of Concrete Structures*, Ed. Z.P. Bažant, Elsevier Applied Science, London and New York, p. 251-259.
- DE BORST R. (1993) - A generalisation of J_2 -flow theory for polar continua, *Comp. Meth. Appl. Mech. Eng.*, **103**, p. 347-362.
- DE BORST R., SLUYS L.J., MÜHLHAUS H.-B. and PAMIN J. (1993) - Fundamental issues in finite element analyses of localization of deformation, *Eng. Comput.*, **10**, p. 99-121.
- DE BORST R., FEENSTRA P.H., PAMIN J. and SLUYS L.J. (1994) - 'Some current issues in computational mechanics of concrete structures', *Proc. EURO-C 1994 Int. Conf. Computer Modelling of Concrete Structures*, Eds H. Mang et al, Pineridge Press, Swansea, p. 283-302.
- DE BORST R. and GROEN A. (1994) - Some observations on element performance in isochoric and dilatant plastic flow, *Int. J. Num. Meth. Eng.*, submitted for publication.
- DE BORST R., PAMIN J., SCHELLEKENS J.C.J. and SLUYS L.J. (1994) - 'Instability in materials - Computational aspects', *Proc. Eighth Conf. Int. Assoc. Computer Methods and Advances in Geomaterials*, Eds H.J. Siriwardane and M.M. Zaman, A. A. Balkema, Rotterdam, p. 91-102.
- CARMELIET J. (1992) - *Duurzaamheid van weefselgewapende pleisters voor buitenisolatie*, Dissertation, Catholic University of Leuven, Leuven.
- CARMELIET J. and DE BORST R. (1994) - 'Nonlocal damage and random fields', *Proc. EURO-C 1994 Int. Conf. Computer Modelling of Concrete Structures*, Eds H. Mang et al, Pineridge Press, Swansea, p. 73-82.
- CARPINTERI A., VALENTE S., FERRARA G. and MELCHIORRI G. (1993) - Is Mode-II fracture energy a real material property? *Comp. & Struct.*, **48**, p.397-413.

- CHEN W.F. and HAN D.J. (1988) - *Plasticity for Structural Engineers*, Chapter 7, Springer-Verlag, New York.
- COLEMAN B.D. and HODGDON M.L. (1985) - On shear bands in ductile materials, *Arch. Ration. Mech. Anal.*, **90**, p. 219-247.
- CRISFIELD M.A. (1991) - *Non-linear Finite Element Analysis of Solids and Structures*, Volume 1, Chapter 6, J. Wiley & Sons, Chichester.
- DASGUPTA S. and SENGUPTA D. (1990) - A higher-order triangular plate bending element revisited, *Int. J. Num. Meth. Eng.*, **30**, p. 419-430.
- DVORKIN E.N., CUTTIÑO A.M. and GIOIA G. (1990) - Finite elements with displacement interpolated embedded localization lines insensitive to mesh size and distortions, *Int. J. Num. Meth. Eng.*, **30**, p. 541-564.
- ERINGEN A.C. (1968) - Theory of micropolar elasticity, *Fracture, an Advanced Treatise*, Ed. H. Leibowitz, Academic Press, New York, p. 621-729.
- ERINGEN A.C. and EDELEN D.G.B. (1972) - On nonlocal elasticity, *Int. J. Engng Sci.*, **10**, p. 233-248.
- FEENSTRA P.H. (1993) - *Computational aspects of biaxial stress in plain and reinforced concrete*, Dissertation, Delft University of Technology, Delft.
- FISH J. and BELYTSCHKO T. (1988) - Elements with embedded localization zones for large deformation problems, *Comp. & Struct.*, **30**, p. 247-256.
- GENS A. and POTTS D.M. (1988) - Critical state models in computational geomechanics, *Eng. Comput.*, **5**, p. 178-197.
- HILL R. (1958) - A general theory of uniqueness and stability in elastic-plastic solids, *J. Mech. Phys. Solids*, **6**, p. 236-249.
- HILLERBORG A., MODEER M. and PETERSSON P.E. (1976) - Analysis of crack formation and crack growth in concrete by means of fracture mechanics and finite elements, *Cement and Concrete Research*, **6**, p. 773-782.
- HORDIJK D.A. (1991) - *Local approach to fatigue of concrete*, Dissertation, Delft University of Technology, Delft.
- HUERTA A. and PIJAUDIER-CABOT G. (1994) - Discretization influence on regularization by two localization limiters, *ASCE J. Eng. Mech.*, **120**, p. 1198-1218.
- HUGHES T.J.R. (1980) - Generalization of selective integration procedures to anisotropic and non-linear media, *Int. J. Num. Meth. Eng.*, **15**, p. 1413-1418.
- HUGHES T.J.R. (1987) - *The Finite Element Method. Linear Static and Dynamic Analysis*, Chapter 4, Prentice-Hall, New Jersey.
- JETTEUR PH. and CESCOTTO S. (1991) - A mixed finite element for the analysis of large inelastic strains, *Int. J. Num. Meth. Eng.*, **31**, p. 229-239.
- LARSSON R. & RUNESSON K. (1992) - 'Plastic localisation captured by discontinuous displacement approximation', *Proc. Third Int. Conf. Computational Plasticity: Fundamentals and Applications*, Eds D.R.J. Owen et al, Pineridge Press, Swansea, p. 605-616.
- LIU W.K., ONG J.S.-J. and URAS R.A. (1985) - Finite element stabilization matrices - a unification approach, *Comp. Meth. Appl. Mech. Eng.*, **53**, p. 13-46.

- LOTFI H.R. and SHING P.B. (1994) - 'Analysis of concrete fracture with an embedded crack approach', *Proc. EURO-C 1994 Int. Conf. Computer Modelling of Concrete Structures*, Eds H. Mang et al, Pineridge Press, Swansea, p. 343-352.
- LOURENÇO P.B., ROTS J.G. and BLAAUWENDRAAD J. (1994) - 'Implementation of an interface cap model for the analysis of masonry structures', *Proc. EURO-C 1994 Int. Conf. Computer Modelling of Concrete Structures*, Eds H. Mang et al, Pineridge Press, Swansea, p. 123-134.
- MAIER G. and HUECKEL T. (1979) - Nonassociated and coupled flow rules of elastoplasticity for rock-like materials, *Int. J. Rock Mech. Min. Sci. & Geomech. Abstr.*, **16**, p. 77-92.
- MAZARS J. and PIAUDIER-CABOT G. (1989) - Continuum damage theory - application to concrete, *ASCE J. Eng. Mech.*, **115**, p. 345-365.
- VAN MIER J.G.M. (1984) - *Strain-softening of concrete under multiaxial loading conditions*, Dissertation, Delft University of Technology, Delft
- VAN MIER J.G.M. (1991) - Mode-I fracture of concrete: discontinuous crack growth and crack interface grain bridging, *Cement and Concrete Research*, **21**, p. 1-15.
- MINDLIN R.D. (1962) - Influence of couple-stresses on stress concentrations, *Exp. Mech.*, **3**, p. 1-7.
- MÜHLHAUS H.-B. and VARDOULAKIS I. (1987) - The thickness of shear bands in granular materials, *Geotechnique*, **37**, p. 271-283.
- MÜHLHAUS H.-B. and AIFANTIS E.C. (1991) - A variational principle for gradient plasticity, *Int. J. Solids Structures*, **28**, p. 845-857.
- MÜHLHAUS H.-B., DE BORST R. and AIFANTIS E.C. (1991) - 'Constitutive models and numerical analyses for inelastic materials with microstructure', *Proc. Seventh Conf. Int. Assoc. Comp. Methods and Advances in Geomechanics*, Eds G. Beer et al, A. A. Balkema, Rotterdam, p. 377-385.
- NAGTEGAAL J.C., PARKS D.M. and RICE J.R. (1974) - On numerically accurate finite element solutions in the fully plastic range, *Comp. Meth. Appl. Mech. Eng.*, **4**, p. 153-177.
- NEEDLEMAN A. (1988) - Material rate dependence and mesh sensitivity in localization problems, *Comp. Meth. Appl. Mech. Eng.*, **67**, p. 69-86.
- NEILSEN M.K. and SCHREYER H.L. (1993) - Bifurcations in elastic-plastic materials, *Int. J. Solids Structures*, **30**, p. 521-544.
- NOORU-MOHAMED M.B. (1992) - *Mixed-mode fracture of concrete: an experimental approach*, Dissertation, Delft University of Technology, Delft.
- OLIVER J. and SIMO J.C. (1994) - 'Modelling strong discontinuities by means of strain softening constitutive equations', *Proc. EURO-C 1994 Int. Conf. Computer Modelling of Concrete Structures*, Eds H. Mang et al, Pineridge Press, Swansea, p. 363-372.
- OLOFSSON T., KLISIŃSKI M. and NEDAR P. (1994) - 'Inner softening bands: a new approach to localization in finite elements', *Proc. EURO-C 1994 Int. Conf. Computer Modelling of Concrete Structures*, Eds H. Mang et al, Pineridge Press, Swansea, p.

- 373-382.
- ORTIZ M. and SIMO J.C. (1986) - An analysis of a new class of integration algorithms for elastoplastic constitutive relations, *Int. J. Num. Meth. Eng.*, **23**, p. 353-366.
- ORTIZ M., LEROY Y. and NEEDLEMAN A. (1987) - A finite element method for localized failure analysis, *Comp. Meth. Appl. Mech. Eng.*, **61**, p. 189-214.
- ORTIZ M. and MORRIS G.R. (1988) - C^0 finite element discretization of Kirchhoff's equations of thin plate bending, *Int. J. Num. Meth. Eng.*, **26**, p. 1551-1566.
- ORTIZ M. and QUIGLEY J.J. (1990) - Adaptive mesh refinement in strain localization problems, *Comp. Meth. Appl. Mech. Eng.*, **90**, p.781-804.
- OZBOLT J., PETRANGELI M. and ELIGEHAUSEN R. (1994) - 'Nonlocal fracture analysis - identification of material model parameters', *Proc. EURO-C 1994 Int. Conf. Computer Modelling of Concrete Structures*, Eds H. Mang et al, Pineridge Press, Swansea, p. 383-392.
- PAMIN J. and DE BORST R. (1992) - 'A rectangular element for gradient plasticity', *Proc. Third Int. Conf. Computational Plasticity: Fundamentals and Applications*, Eds D.R.J. Owen et al, Pineridge Press, Swansea, p. 2009-2020.
- PAMIN J. and DE BORST R. (1994) - 'Gradient plasticity and finite elements in the simulation of concrete fracture', *Proc. EURO-C 1994 Int. Conf. Computer Modelling of Concrete Structures*, Eds H. Mang et al, Pineridge Press, Swansea, p. 393-402.
- PIETRUSZCZAK St. and MRÓZ Z. (1981) - Finite element analysis of deformation of strain-softening materials, *Int. J. Num. Meth. Eng.*, **17**, p. 327-334.
- PIJAUDIER-CABOT G. and BAŽANT Z.P. (1987) - Nonlocal damage theory, *ASCE J. Eng. Mech.*, **113**, p. 1512-1533.
- PIJAUDIER-CABOT G. and BENALLAL A. (1993) - Strain localization and bifurcation in a nonlocal continuum, *Int. J. Solids Structures*, **13**, p. 1761-1775.
- PIJAUDIER-CABOT G., LA BORDERIE CH. and FICHANT S. (1994) - 'Damage mechanics for concrete modelling: Applications and comparisons with plasticity and fracture mechanics', *Proc. EURO-C 1994 Int. Conf. Computer Modelling of Concrete Structures*, Eds H. Mang et al, Pineridge Press, Swansea, p. 17-36.
- READ H.E. and HEGEMIER G.A. (1984) - Strain softening of rock, soil and concrete - A review article, *Mech. Mater.*, **3**, p. 271-294.
- ROELFSTRA P.E. (1989) - 'Simulation of localization processes with numerical concrete', *Cracking and Damage: Strain Localization and Size Effect*, Eds J. Mazars and Z.P. Bažant, Elsevier Applied Science, London and New York, p. 79-90.
- ROTS J.G. (1988) - *Computational modeling of concrete fracture*, Dissertation, Delft University of Technology, Delft.
- ROTS J.G. and DE BORST R. (1989) - Analysis of concrete fracture in "direct" tension, *Int. J. Solids Structures*, **25**, p. 1381-1394.
- RUDNICKI J.W. and RICE J.R. (1975) - Conditions for the localization of deformation in pressure-sensitive dilatant materials, *J. Mech. Phys. Solids*, **23**, p. 371-394.
- RUNESSON K. and MRÓZ Z. (1989) - A note on nonassociated plastic flow rules, *Int. J. Plasticity*, **5**, p. 639-658.

- RUNESSON K., OTTOSEN N.S. and PERIĆ D. (1989) - Discontinuous bifurcations of elastic-plastic solutions at plane stress and plane strain, *Int. J. Plasticity*, **7**, p. 99-121.
- SANDLER I.S. (1984) - 'Strain softening for static and dynamic problems', *Proc. Symp. Constitutive Equations: Micro, Macro and Computational Aspects*, Ed. K. Willam, ASME, New York, p. 217-231.
- SCHELLEKENS J.C.J. (1992) - *Computational strategies for composite structures*, Dissertation, Delft University of Technology, Delft.
- SCHLANGEN E. and VAN MIER J.G.M. (1991) - 'Boundary effects in mixed mode I and II fracture of concrete', *Fracture Processes in Concrete, Rock and Ceramics*, Eds J.G.M. van Mier et al, E & FN Spon/Chapman & Hall, London, p. 705-716.
- SCHLANGEN E. (1993) - *Experimental and numerical analysis of fracture processes in concrete*, Dissertation, Delft University of Technology, Delft.
- SCHREYER H.L. and CHEN Z. (1986) - One-dimensional softening with localization, *ASME J. Appl. Mech.*, **53**, p. 791-979.
- SIMO J.C. and TAYLOR R.L. (1985) - Consistent tangent operators for rate-independent elasto-plasticity, *Comp. Meth. Appl. Mech. Eng.*, **48**, p. 101-118.
- SIMO J.C. and TAYLOR R.L. (1986) - A return mapping algorithm for plane stress elasto-plasticity, *Int. J. Num. Meth. Eng.*, **22**, p. 649-670.
- SIMO J.C., KENNEDY J.G. and GOVINDJEE S. (1988), Non-smooth multisurface plasticity and viscoplasticity. Loading/unloading conditions and numerical algorithms, *Int. J. Num. Meth. Eng.*, **26**, p. 2161-2185.
- SIMO J.C. (1989) - 'Strain softening and dissipation: a unification of approaches', *Cracking and Damage: Strain Localization and Size Effect*, Eds J. Mazars and Z.P. Bažant, Elsevier Applied Science, London and New York, p. 440-461.
- SLUYS L.J. (1992) - *Wave propagation, localization and dispersion in softening solids*, Dissertation, Delft University of Technology, Delft.
- SLUYS L.J., DE BORST R. and MÜHLHAUS H.-B. (1993) - Wave propagation, localization and dispersion in a gradient-dependent medium, *Int. J. Solids Structures*, **30**, p. 1153-1171.
- SLUYS L.J. (1994) - 'Gradient theory: Discretization principles and application', *Proc. EURO-C 1994 Int. Conf. Computer Modelling of Concrete Structures*, Eds H. Mang et al, Pineridge Press, Swansea, p. 403-412.
- STANKOWSKI T., ETSE G., RUNESSON K., STURE S. and WILLAM K. (1992) - 'Composite analysis with discrete and smeared crack concept', *Fracture Mechanics of Concrete Structures*, Ed. Z.P. Bažant, Elsevier Applied Science, London and New York, p. 269-274.
- STEINMANN P. and WILLAM K. (1991) - Performance of enhanced finite element formulations in localized failure computations, *Comp. Meth. Appl. Mech. Eng.*, **90**, p. 845-867.
- STEINMANN P. and WILLAM K. (1991) - Localization within the framework of micropolar elasto-plasticity, *Advances in continuum mechanics*, Ed. V. Mannl et al, Springer

- Verlag, Berlin, p. 296-313.
- VARDOULAKIS I. and AIFANTIS E.C. (1991) - A gradient flow theory of plasticity for granular materials, *Acta Mechanica*, **87**, p. 197-217.
- VERMEER P.A. and DE BORST R. (1984) - Non-associated plasticity for soils, concrete and rock, *Heron*, **29**, No.3.
- VONK R.A. (1992) - *Softening of concrete loaded in compression*, Dissertation, Eindhoven University of Technology, Eindhoven.
- WANG W. (1994) - *Instability phenomena in softening materials, II. The role of imperfections in viscoplastic solutions*, TU-Delft Report no. 25-2-94-2-01, Delft.
- WILLAM K.J. (1984) - 'Experimental and computational aspects of concrete fracture', *Proc. Int. Conf. Computer Aided Analysis and Design of Concrete Structures*, Eds F. Damjanić et al, Pineridge Press, Swansea, p. 33-70.
- WILLAM K.J. and ETSE G. (1990) - 'Failure assessment of the extended Leon model for plain concrete', *Proc. Second Int. Conf. Computer Aided Analysis and Design of Concrete Structures*, Eds N. Bićanić et al, Pineridge Press, Swansea, p. 851-870.
- WILLAM K.J. and DIETSCHKE A. (1990) - 'Fundamental aspects of strain-softening descriptions', *Fracture Mechanics of Concrete Structures*, Ed. Z.P. Bažant, Elsevier Applied Science, London and New York, p. 227-230.
- WILLAM K.J., MÜNZ T., ETSE G. and MENÉTREY PH. (1994) - 'Failure conditions and localization in concrete', *Proc. EURO-C 1994 Int. Conf. Computer Modelling of Concrete Structures*, Eds H. Mang et al, Pineridge Press, Swansea, p. 263-282.
- WONG B.L. and BELYTSCHKO T. (1987) - Assumed strain stabilization procedure for the 9-node Lagrange plane and plate elements, *Eng. Comput.*, **4**, p. 229-239.
- ZBIB H.M. and AIFANTIS E.C. (1988) - On the localization and postlocalization behavior of plastic deformation, I,II,III, *Res Mechanica*, **23**, p. 261-277, 279-292, 293-305.
- ZIENKIEWICZ O.C. and NAKAZAWA S. (1982) - The penalty function and its applications to the numerical solution of boundary value problems, *Am. Soc. Mech. Eng. AMD*, **51**, p. 157-179.
- ZIENKIEWICZ O.C. and TAYLOR R.L. (1991) - *The Finite Element Method, Fourth edition*, Vol.2, Chapter 1-2, McGraw-Hill, London.

Table 1: Gradient plasticity elements

| Name | Nodes | Int. | Cont. | Comments |
|--------------|-------|-------|-------|-------------------------------------|
| <i>R24MG</i> | 4/4 | 2×2 | C^1 | Hermitian |
| <i>R24EG</i> | 4/4 | 2×2 | C^1 | Hermitian, \bar{B} enhanced |
| <i>R32MG</i> | 8/4 | 2×2 | C^1 | Hermitian |
| <i>R32EG</i> | 8/4 | 2×2 | C^1 | Hermitian |
| <i>R34MG</i> | 9/4 | 2×2 | C^1 | Hermitian, zem for u |
| <i>R34EG</i> | 9/4 | 2×2 | C^1 | Hermitian, zem for u |
| <i>T30MG</i> | 6/3 | 6 | C^1 | Quintic, inc |
| <i>T30EG</i> | 6/3 | 6 | C^1 | Quintic, inc |
| <i>L6G</i> | 2/2 | 2 | C^1 | Hermitian, 1D |
| <i>L7G</i> | 3/2 | 2 | C^1 | Hermitian, 1D |
| <i>Q20MC</i> | 4/4 | 1/2×2 | C^0 | Linear, zem or locking |
| <i>Q20EC</i> | 4/4 | 1/2×2 | C^0 | Linear, zem or locking |
| <i>Q40MC</i> | 8/8 | 2×2 | C^0 | Serendipity, inc, zem for λ |
| <i>Q40EC</i> | 8/8 | 2×2 | C^0 | Serendipity, inc, zem for λ |
| <i>Q45MC</i> | 9/9 | 2×2 | C^0 | Lagrangian, zem |
| <i>Q45EC</i> | 9/9 | 2×2 | C^0 | Lagrangian, zem |
| <i>T30MC</i> | 6/6 | 3 | C^0 | Quadratic, inc |
| <i>T30EC</i> | 6/6 | 3 | C^0 | Quadratic, inc |
| <i>L6C</i> | 2/2 | 1 | C^0 | Linear, 1D |
| <i>L9C</i> | 3/3 | 2 | C^0 | Quadratic, 1D |
| <i>R28EG</i> | 8/4 | 2×2 | C^0 | Cubic, non-conforming, inc |
| <i>Q43EC</i> | 8/9 | 2×2 | C^0 | 'Heterosis' |
| <i>T15MC</i> | 3/3 | 1 | C^0 | Linear, locking |
| <i>T15EC</i> | 3/3 | 1 | C^0 | Linear, locking |
| <i>T21MG</i> | 6/3 | 3 | C^0 | Cubic, non-conforming, inc |
| <i>T21EG</i> | 6/3 | 3 | C^0 | Cubic, non-conforming, inc |
| <i>T24MC</i> | 3/6 | 1 | C^0 | Linear/quadratic, zem |
| <i>T24EC</i> | 3/6 | 1 | C^0 | Linear/quadratic, zem |

Names:

R - rectangle,**T** - triangle,**Q** - quadrilateral,**L** - 1D**M** - membrane (plane stress),**E** - plane strain**G** - algorithm for C^1 elements,**C** - algorithm for C^0 elements with penalty constraint

Symbols:

zem - spurious zero energy modes present**inc** - sampling points not optimal (incorrect mapping $F_{ip} \neq 0$)

GRADIENT-DEPENDENT PLASTICITY IN NUMERICAL SIMULATION OF LOCALIZATION PHENOMENA

Summary

Localization of deformation is associated with a softening behaviour of the analyzed structure or specimen. In the classical (homogenized) continuum framework a negative slope of the stress-strain relation (strain softening) introduces a material instability, which may result in the loss of well-posedness of the partial differential equations governing the boundary value problem. Localization then occurs in a set of measure zero and a pathological discretization sensitivity is observed in numerical simulations. To remedy this difficulty the continuum theory must be enhanced to become nonlocal or dependent on higher-order deformation gradients. Such continua include a characteristic length scale, which defines the width of localization bands (Chapter 2).

In this thesis we consider a gradient plasticity theory, in which the yield function depends on the Laplacian of an invariant plastic strain measure. The gradient term acts as a stabilizer and allows to preserve the well-posedness of the rate boundary value problem in the softening regime. The essential consequence of the gradient-dependence is that, unlike in the classical theory, the plastic consistency condition becomes a partial differential equation. Weak satisfaction of the equilibrium and plastic consistency conditions is assumed to solve the boundary value problem of nonlinear statics with small deformations (Chapter 3).

An incremental-iterative algorithm with a consistent tangent operator is derived. Independent finite element discretization of the displacements and plastic multipliers is used. The presence of the Laplacian sets the requirement of C^1 -continuity of the plastic multiplier field. When the first derivatives of this quantity are interpolated as well, and connected to the plastic multiplier field by a penalty constraint, an alternative C^0 -element formulation is obtained. Several one-dimensional, quadrilateral and triangular elements with mixed interpolation have been implemented. The solution procedure is compared with the classical return mapping algorithm and the implications of the gradient dependence of the yield strength are described (Chapter 4).

The Huber-Mises, Drucker-Prager and Rankine gradient-dependent yield/fracture functions are formulated and applied in several mesh-sensitivity studies. It is numerically verified that the internal length incorporated in the theory sets the size of the localization zone and that the post-peak results do not suffer from the spurious sensitivity to mesh refinement or alignment. The regularization is equally effective for the description of localized failure under shear, tension and mixed-mode conditions.

The performance of the implemented elements is compared using the Huber-Mises gradient plasticity for a one-dimensional tension test and a biaxial compression test. It

is shown that the rectangular element with serendipity interpolation of displacements and hermitian interpolation of plastic strains is the most reliable. The influence of imperfections and the uniqueness of the numerical solution is also investigated (Chapter 5).

Two geotechnical problems are analyzed using the (non)associated Drucker-Prager gradient plasticity theory with cohesion softening. Physically meaningful results are obtained in the post-critical regime. Shear banding and bulging localization modes are predicted in the plane strain biaxial compression test. The stability of a slope and a vertical embankment is also examined (Chapter 6).

The vertex-enhanced Rankine gradient plasticity is applied to Mode-I and mixed-mode concrete fracture problems. Several plane stress configurations (a beam in four-point-bending, a bar in direct tension, a SEN beam and a DEN specimen) are analyzed and the results are compared with experimental findings. The fracture energy and the internal length scale (which determines the crack band width) are the material constants and an exponential softening diagram is used. The results of gradient plasticity simulations show a good agreement with the experiments and the size effect is correctly reproduced (Chapter 7).

In the conclusions some robustness requirements for the developed mixed elements and the observations from the numerical simulations are summarized. Some prospects of the gradient plasticity development are suggested.

GRADIËNT-AFHANKELIJKE PLASTICITEIT IN NUMERIEKE SIMULATIE VAN LOKALISATIE VERSCHIJNSELEN

Samenvatting

Lokalisatie van deformatie wordt geassocieerd met het "softening"-gedrag van de geanalyseerde constructies of proefstukken. In het klassieke (gehomogeniseerde) continuümraamwerk introduceert een negatieve helling in de spanning-rek relatie ("strain softening") een materiaalinstabiliteit die kan leiden tot het verlies van de goedgesteldheid van de partiële differentiaalvergelijkingen die het randvoorwaardeprobleem beschrijven. Lokalisatie treedt dan op in een zone met afmeting nul en een pathologische discretisatie-afhankelijkheid wordt waargenomen in de numerieke simulaties. Om dit probleem op te lossen moet de continuümtheorie verrijkt worden om niet-lokaal of afhankelijk van hogere-orde deformatiegradiënten te worden. Deze continua bevatten een karakteristieke lengteschaal die de breedte van de lokalisatiebanden vastlegt (Hoofdstuk 2).

In dit proefschrift behandelen we een gradiënt-plasticiteitstheorie, waarin de vloeifunctie afhangt van de Laplace operator van een invariante plastische rekgrootheid. De gradiëntenterm fungeert als stabilisator en zorgt voor het behoud van de goedgesteldheid van het randvoorwaardeprobleem in het "softening" traject. De essentiële consequentie van de gradiënt-afhankelijkheid is dat, in tegenstelling tot de klassieke theorie, de plastische consistentie-conditie een partiële differentiaalvergelijking wordt. Om het randvoorwaardeprobleem voor het niet-lineaire statische geval voor kleine deformaties op te lossen wordt aangenomen dat in zwakke zin wordt voldaan aan de evenwichtsvergelijking en de plastische consistentie-conditie (Hoofdstuk 3).

Een incrementeel-iteratief algoritme met een consistente tangent operator is afgeleid. Een onafhankelijke eindige-elementendiscretisatie voor de verplaatsingen en de plastische multiplicatoren is gebruikt. De aanwezigheid van de Laplace operator maakt de C^1 -continuïteit van het plastische multiplicatorveld noodzakelijk. Een alternatief C^0 -element formulering kan worden verkregen wanneer de eerste afgeleiden van deze grootheid ook worden geïnterpoleerd en worden verbonden met het plastische multiplicatorveld via een "penalty constraint". Diverse één-dimensionale, rechthoekige en driehoekige elementen met gemixte interpolatie zijn geïmplementeerd. De oplossingsprocedure is vergeleken met het klassieke "return mapping" algoritme en tevens zijn de problemen van de gradiënt-afhankelijkheid van de vloeisterkte beschreven (Hoofdstuk 4).

De Huber-Mises, Drucker-Prager en Rankine gradiënt-afhankelijke vloeibreekfuncties zijn geformuleerd en toegepast in verschillende studies naar de afhankelijkheid van het eindige-elementennet. Met behulp van numerieke analyses is geverifieerd dat de

interne lengte, die is ingebouwd in de theorie, de afmeting van de lokalisatiezone bepaalt en dat de resultaten in het na-kritische traject niet beïnvloed worden door een valse gevoeligheid met betrekking tot elementennet-verfijning of elementennet-oriëntatie. De regularisatie is zowel effectief voor de beschrijving van het gelokaliseerd bezwijken onder afschuiving, trek en "mixed mode" condities.

De prestatie van de geïmplementeerde elementen is vergeleken voor het geval van Huber-Mises plasticiteit voor één-dimensionale trektest en een bi-axiale druktest. Er is aangetoond dat het rechthoekige element met een "serendipity" interpolatie van de verplaatsingen en een "Hermitian" interpolatie van de plastische rekken het betrouwbaarst is. Tevens is de invloed van imperfecties en de éénvoudigheid van de numerieke oplossing onderzocht (Hoofdstuk 5).

Twee geotechnische problemen zijn geanalyseerd met behulp van de (niet-)geassocieerde Drucker-Prager gradiënt-plasticiteitstheorie met cohesie-"softening". Fysisch betekenisvolle resultaten zijn verkregen in het na-kritische traject. Afschuiving- en "bulging"-lokalisatiepatronen zijn voorspeld in een biaxiale druktest onder een vlakke-vervormingstoestand. Tevens is de stabiliteit van een helling en een verticale kade onderzocht (Hoofdstuk 6).

Het Rankine gradiënt-afhankelijke plasticiteitsmodel met een verbeterde formulering voor de hoekpunten is toegepast voor "mode-I" en "mixed-mode" betonmechanica-problemen. Verschillende vlakke-spanning-configuraties (een balk onder vierpunts-buiging, een ligger onder éénassige trek, SEN-balk en DEN-proefstuk) zijn geanalyseerd en de resultaten zijn vergeleken met de experimentele bevindingen. De scheur-energie en de interne lengteschaal (die de scheurbandbreedte bepaalt) zijn materiaalconstanten en een exponentieel "softening"-diagram is gebruikt. De resultaten van de gradiëntplasticiteit-simulaties tonen een goede overeenstemming met experimenten en de afmetinginvloed wordt korrekt gereproduceerd.

In de conclusies zijn enkele robuustheidseisen voor de ontwikkelde elementen en resultaten van de numerieke simulaties samengevat. Tenslotte worden enkele toekomstige ontwikkelingen van de gradiëntplasticiteitstheorie voorgesteld.

Curriculum vitae

| | |
|-------------------------------|---|
| Name | Jerzy Krzysztof Pamin |
| January 20, 1962 | Born in Krynica, Poland |
| 1981 | Examination of general education in Nowy Sącz, Poland |
| 1981-1986 | Study at the Faculty of Civil Engineering, TU Cracow, since 83 in the field of the Theory of Structures |
| August-September 1985 | IAESTE practical training at Yokogawa Bridge Works Ltd. in Chiba, Japan |
| January 26, 1987 | M.Sc.(Civil Engineering) at TU Cracow on the basis of the diploma work on the 'Application of the FEM in the Analysis of RC Panels' |
| April 1987 - September 1990 | Research assistant at the Laboratory of Computational Methods in Mechanics, Institute of Structural Mechanics, TU Cracow |
| October 1990 - September 1991 | Guest research fellow at the Mechanics and Structures Division, Faculty of Civil Engineering, TU Delft |
| October 1991 - December 1994 | Research assistant at the Mechanics and Structures Division, Faculty of Civil Engineering, TU Delft |